Modeling and Characterization of High TCR, Low Noise Si/$Si_{1-x}Ge_x$ Multi-Quantum Well Detector for Uncooled Microbolometers

by

ATIA SHAFIQUE

Submitted to the Graduate School of Engineering and Natural Sciences
in partial fulfillment of the requirements for the degree of
Doctor of Philosophy

Sabancı University

August, 2018

Modeling and Characterization of High TCR, Low Noise Si/$Si_{1-x}Ge_x$ Multi-Quantum Well Detector for Uncooled Microbolometers

APPROVED BY

Prof. Dr. Yaşar GÜRBÜZ (Thesis Advisor)	....
Assoc. Prof. Dr. Meriç ÖZCAN	....
Prof. Dr. Mehmet YILDIZ	....
Prof. Dr. Fevzi Necati ECEVİT	....
Prof. Dr. Naci İNCİ	....

DATE OF APPROVAL: ....

© Atia shafique 2018

All Rights Reserved

To My Parents
Who always have sacrificed
their needs for my needs...

The more you know, the more you realize how much you don't know...

(David T.Freeman)

Acknowledgements

Over the span of my six years of study and research tenure at Sabanci University, a lot of amazing people have impacted my life, in general and accomplishment of this work, in particular. To reflect all these years I have spent here, I am overwhelmed by a sense of achievement and personal growth that would not have been possible without the support and assistance of numerous people in both professional and personal capacity. To list everyone to whom I owe thanks could fill as many pages as a chapter of this thesis. To those I omit here, I would like to express my honest appreciation for their support throughout my stay here.

Foremost, I would like to express my sincere gratitude to my advisor Prof. Yasar Gurbuz, for giving me the opportunity to join Microelectronics Research Group. I still remember the day when I had first contacted him by an email and got his instant reply about scheduling the Skype interview, which was simultaneously shocking and overwhelming moment for me. I am thankful for his firm support, constant encouragement and above all his patience which has enabled me to come to this far end of my work completion. I would also like to warmly thank my committee members Prof. Mehmet Yildiz, Assoc. Prof. Meric Ozcan, Prof. Fevzi Necati Ecevit, and Prof. Naci Inci for being on my thesis committee. Particularly, Prof. Mehmet Yildiz for his valuable suggestions and fruitful discussions to improve the quality of my work.

This dissertation work is the part of a project financially supported by the Scientific and Technological Research Council of Turkey (Tubitak) under the grant 115E098. Throughout my entire studies, I have been supported by Tubitak scholarship. I am grateful for this scholarship and hoping that the program can keep on supporting many young scientists across the borders in future.

I would also like to acknowledge Dr. Mehmet Kaynak and Dr. Canan B.Kaynak along with many others at IHP Microelectronics, Germany as our project collaborators and for hosting me twice at IHP Microelectronics as a visiting scientist. In particular, I would like to thank Julian Korn, who helped me to get acquainted with Sentaurus TCAD and for his deep involvement and guidance in the device modeling without which I would not be able to develop hands-on skills in the domain of device modeling. I would like to appreciate Dr. Jaroslaw Dabrowski for his immense knowledge and interest in clarifying my queries and confusions. I would like to thank Barbaros Centindogan and Mesut Inac for their friendship and joyful company during my stay at IHP.

My sincere and deepest gratitude to my mentor Dr. Arsalan Jawed, the person who has been always the source of inspiration in every aspect. Prior to join Sabanci University, under his supervision during my job, it was his dedication, sincerity and

very humble attitude which has led me to discover my own strengths, to polish my skills and gave me the confidence to take my professional career to the next level.

Special thanks to my senior labmates Dr. Huseyin Kayahan, Dr. Omer Ceylan and Dr. Melik Yazici for their support and positive attitude. Especially, Omer Ceylan to turn my mood lighter by his humorous and amusing trolls whenever I was extremely stressed at a times during the course of research and for proof-reading this thesis. I would like to thank Shahbaz Abbasi for his discussions and ideas to improve the overall quality of work, particularly, his help during the article writing and publication process. I would like to thank our laboratory specialist Ali Kasal for his help in arrangement and maintenance of the measurement equipment. Overall, I would like to thank all the members of the Microelectronics research group Ilker Kalyoncu, Abdurrahman Burak, Murat Davulcu, Can Caliskan, Alper Guner, Emre Can Durmaz, Esref Turkmen, Hamza Kandis, Elif Gul Ozkan for creating the friendly lab work environment, moreover, it helped me to develop and improve my Turkish language skills.

During these long six years of my study, I have been blessed with countless number of good and sincere friends who have been standing by my side. With whom, not only that I have cherished the joyful moments and fun travels but also provided me the shoulder to cry on during the dark and gloomy days, and never let me feel a foreigner on a far land away from my home. I would like to thank my very special friends Esma Fatima Bilgin, Mariamu Kassim, Jaime Fernando Delgado, Asma Abdullah Almurtadha, Parveen Qureshi, Dilek Cakirolgu for making my graduate studies and university life joyful. Special thanks to the my friends Aneela Tanveer, Seyma Kalyoncu, and lolai Ikromzoda for their constant encouragement and support during the most difficult last one year and their home-cooked meals and the chitchats.

Last but not least, I would like to thank my parents for their unconditional love, efforts and support throughout in shaping up my life. Despite of being very humble background, my father Muhammad Shafique always trusted and encouraged me to opt the professional career in the field of electronic engineering. I would definitely not be the woman I am today without the dedication and sleepless nights of my mother Tasneem Shafique and strong support of my sisters Ambreen Shafique, Sadia Shafique, Lubna Shafique and my brother Usman Shafique.

Above all else, all the glory and praise to Allah. He has been my strength when I was weak, my endurance when I was tired and my hope when I was lost.

Modeling and Characterization of High TCR, Low Noise $Si/Si_{1-x}Ge_x$ Multi-Quantum Well for Uncooled Microbolometers

Atia Shafique
EE, Ph.D. Thesis, August 2018
Thesis Advisor: Prof. Dr. Yaşar Gürbüz

Keywords: Long-wave infrared, uncooled microbolometer, predictive modeling, TCAD, high Ge content based Si/SiGe Multi-Quantum well detector, high TCR detector, low noise detector.

Abstract

Uncooled infrared focal plane arrays (IR FPAs) have seen unprecedented growth over the last decade and ubiquitously extending its application beyond the military realm into various diverse areas such as: surveillance, security and law enforcement, thermography (predictive maintenance, building inspection), industrial process control, automotive safety and medical imaging. The uncooled microbolometers are mainly used for imaging in long wave infrared spectral range (LWIR).

In the recent years, the efforts made for the technical evolution of the microbolometer involves: pixel size reduction, new materials and designs to enhance the detection and integration capability. Currently, Vanadium oxide VO_x together with a-Si based FPAs have the major share in the uncooled imaging market. Nevertheless, they offer limited performance in terms of the thermal sensitivity. Here we present, an epitaxially grown $Si/Si_{1-x}Ge_x$ multi-quantum-well (MQW) detector as a potential candidate to improve the thermal sensitivity due to its inherent fringe benefit of ease of the bandgap tailoring by increasing the Ge content up to 50 %. It offers low flicker noise attributed to its single crystalline properties.

The predictive technology computer-aided design (TCAD) tool has been used to obtain a priori estimate to design and develop $Si/Si_{1-x}Ge_x$ MQW detector. A comprehensive predictive device model is developed to investigate the electrical characteristics of $Si/Si_{1-x}Ge_x$ MQW, device design challenges and design trade-offs. The integrated self-consistent numerical modeling framework incorporates the number of interdependent design variables such as Ge content, active device areas, the doping profiles, the thickness and the periodicity of quantum wells. The model is employed to optimize Ge content and the doping profile for the desired Figure-of merits specified in terms of the temperature coefficient of resistance (TCR) and dc resistance (R). The modeling results are validated with the experimental data and found consistent over a wide range of Ge content varied from 30 % up to 50 %. The model predicts TCR can be raised up to 5.4 $\%K^{-1}$ by incorporating 50 % Ge content in MQW (experimentally verified) where the measured flicker noise constant $k_{1/f}$ of the detector is 5.8 $\times 10^{-13}$.

Soğutmasız Bolometreler için Yüksek TCR Değerine Sahip (sıcaklığa bağlı direnç değişim katsayısı), Düşük Gürültülü Si/Si$_{1-x}$Ge$_x$ Çoklu Kuantum Kuyuların Modellenmesi ve Karakterizasyonu

Atia Shafique
EE, doktora Tezi, 2018
Tez Danışmanı: Prof. Dr. Yaşar GÜRBÜZ

Anahtar Kelimeler: Uzun-dalga kızılötesi, soğutmasız bolometre, öngörücü model, TCAD, Si/SiGe çoklu-kuantum kuyusu, yüksek Ge içeren SiGe bolometre, yüksek TCR (sıcaklığa bağlı direnç değişim katsayısı), düşük gürültülü bolometre

Özet

Uzun dalga kızılötesi frekans bandına duyarlı soğutmasız kızılötesi görüntüleme sistemleri pazarı son yıllarda büyük bir büyüme göstermiştir ve kullanım alanları askeri uygulamalardan farklı alanlara kaymaya başlamıştır: gözetleme, güvenlik, termal görüntüleme (öngörülebilir onarım, bina muayenesi), endüstriyel üretim kontrolü, otomotiv güvenliği ve medikal görüntüleme. Son yıllarda bolometrelerin iyileştirilmesi için yapılan çalışmalar şu noktalarda yoğunlaşmıştır: piksel boyutunun küçültülmesi, yeni malzemeler ve tasarım teknikleriyle algılama ve entegrasyon kabiliyetlerinin geliştirilmesi. Halihazırda bolometre pazarında en çok kullanılan malzemeler Vanadyum Oksit (VO$_x$) ve amorf silikon (a-Si) malzemeleridir. Fakat bu malzemeler termal hassaslık bakımından yeterli performans sunamamaktadır. Bu tezde epitaksiyel olarak büyütülmüş Si/Si$_{1-x}$Ge$_x$ çoklu-kuantum kuyulu malzeme yapısı bolometrelerin termal algılama hassaslığının geliştirilmesi için öneril-miştir. Bu yapıda Ge içeriğini % 50'ye kadar artırarak yarıiletken bant aralığını değiştirmek ve tekli kristal yapısı dolayısıyla düşük kırpışma gürültüsü elde etmek mümkün olmaktadır.

Si/Si$_{1-x}$Ge$_x$ çoklu-kuantum kuyu bolometreyi modellemek, tasarlamak ve geliştirmek için TCAD yarıiletken yazılımı kullanılmıştır. Si/Si$_{1-x}$Ge$_x$ çoklu kuantum kuyu bolometrenin elektriksel karakteristiklerinin çıkarılması, tasarım zorluklarının belirlenmesi ve tasarımda birbirlerini etkileyen parametrelerin optimizasyonunun yapılabilmesi için kapsamlı bir model çıkarılmıştır. Geliştirilen model birbiriyle ilişkili Ge içeriği, aktif aygıt alanı, katkılama profilleri, katmanların kalınlıkları, kuantum kuyularının periyodisitesi gibi parametreleri içermektedir. Geliştirilen model kullanılarak istenilen TCR (sıcaklığa bağlı direnç değişim katsayısı) ve dc direnç değerlerine ulaşabilmek için Ge içeriğinin miktarı ve katkılama profilleri(katman kalınlıkları, katkılama oranı, vs) belirlenebilmektedir. Geliştirilen model % 30 ile % 50 aralığında değişen Ge içeriğine göre elde edilen TCR ve direnç değerleri ile deneysel olarak doğrulanmıştır. Geliştirilen model % 50 Ge içerik ile % 5.4K^{-1} TCR değerine ulaşabileceğini göstermiştir.

Contents

Acknowledgements v

Abstract vii

List of Figures xii

List of Tables xvi

List of Abbreviations xvii

1 Chapter 1
Introduction 1
- 1.1 Infrared Imaging . . . 1
- 1.2 Basic Components of an IR Imager . . . 3
- 1.3 IR Detector Technologies . . . 4
- 1.4 Figure-of-Merits (FoM) . . . 5
- 1.5 Outlook on Microbolometers . . . 7
- 1.6 Motivation and Objectives . . . 9
- 1.7 Thesis Outline . . . 11

2 Chapter 2
An Overview of Resistive-Microbolometer 13
- 2.1 Infrared Detection Mechanisms . . . 13
  - 2.1.1 Photon Detection . . . 13
  - 2.1.2 Thermal Detection . . . 13
- 2.2 Materials and System Developments . . . 15
- 2.3 Basic Principal and Detection Mechanism . . . 17
  - 2.3.1 Temperature-Dependent Resistance . . . 18
  - 2.3.2 Temperature Coefficient of Resistance . . . 19
  - 2.3.3 Thermal Conductance . . . 19
- 2.4 Electrical-Thermal Behavior . . . 21
  - 2.4.1 Dynamic Behavior . . . 22
  - 2.4.2 Static Behavior . . . 25
  - 2.4.3 Microbolometer Temperature Resolution . . . 26
  - 2.4.4 Signal Readout . . . 27
  - 2.4.5 DC Responsivity . . . 28
- 2.5 Noise Sources . . . 29
  - 2.5.1 Johnson Noise . . . 29
  - 2.5.2 Flicker Noise . . . 30
  - 2.5.3 Temperature Fluctuation Noise . . . 31
  - 2.5.4 Background Fluctuation Noise . . . 32
  - 2.5.5 Total System Noise . . . 33
- 2.6 Detector Figure of Merits . . . 33
  - 2.6.1 Noise-Equivalent Power . . . 33
  - 2.6.2 Specific Detectivity . . . 33
  - 2.6.3 Noise Equivalent Temperature Difference . . . 34

2.6.4 State-of-the-Art Microbolometers . . . 34
2.7 Design Constraints and Trades-off . . . 36
2.7.1 Pixel Pitch . . . 36
2.7.2 Thermal Conductance and Capacitance . . . 37
2.7.3 Thermal Absorption Efficiency . . . 37
2.7.4 Noise and Integration Time . . . 37
2.7.5 High TCR and Low 1/f Noise Material . . . 38

**3 Chapter 3
Detector Design and Modeling 39**
3.1 Material and Electronic Properties of SiGe Alloy . . . 39
3.1.1 Crystal Structure . . . 39
3.1.2 Band Structure . . . 42
3.2 Detector Design . . . 43
3.2.1 Effect of Carbon-delta Layers . . . 45
3.2.2 Effect of Boron Autodoping . . . 46
3.2.3 Current Transport . . . 47
3.3 Physical Transport Parameters . . . 48
3.3.1 Electron and Hole Effective Masses . . . 48
3.3.2 Effective Density of States (DOS) . . . 50
3.3.3 Intrinsic Carrier Density . . . 51
3.3.4 Bandgap and Bandgap Narrowing (BGN) . . . 52
3.3.5 Electron and Hole Mobility . . . 53
3.3.6 Carrier Generation-Recombination Models . . . 55
3.4 Carrier Transport Modeling . . . 56
3.5 Numerical Simulation Framework and Methodology . . . 61
3.5.1 2-D Device Structure . . . 61
3.5.2 Generating Mesh and Doping Profile . . . 62
3.5.3 Boundary Conditions . . . 63
3.5.4 The Self-Consistent Solution Implementation . . . 65

**4 Chapter 4
Predictive Model Simulation and Validation 69**
4.1 Device Fabrication . . . 69
4.2 Device Characterization . . . 72
4.2.1 HR-XRD Measurement . . . 72
4.2.2 TEM and EDXS Analysis . . . 73
4.2.3 SIMS Analysis . . . 73
4.2.4 DC Transfer Characteristics Measurement . . . 74
4.3 Predictive Simulation and Validation . . . 76
4.3.1 Steady-State Carrier Transport . . . 76
4.3.2 Modeling Ge Content (x) in MQW . . . 77
4.3.3 Quantum well (QW) Periodicity . . . 88
4.3.4 Background Doping . . . 89
4.3.5 Boron Doping in MQW . . . 90
4.3.6 Quantum Well Thickness . . . 91
4.4 Noise Measurement . . . 92
4.4.1 Effect of Ge Content . . . 92
4.4.2 Effect of Bias Voltage . . . 93

4.4.3 Effect of Active Area 93
4.5 Performance Comparison 94

5 Chapter 5
Conclusions and Future Directions **97**

References **101**

List of Figures

1.1 IR spectrum segmentation used for IR imaging technologies [7]. . . . 1
1.2 The peak curves for blackbody radiation based on Plank's theory [7]. 2
1.3 Basic components of an IR imaging system, the camera core is taken from [8]. . . . 3
1.4 The difference between cooled and uncooled IR camera from technology perspective [9] [10] [11]. . . . 4
1.5 Schematic depiction of a unit pixel in a) photon detector using indium bumps and flip-chip technology for hybridization to the interface ROIC [12], b) thermal detector monolithically integrated and suspended over the ROIC [13]. . . . 5
1.6 Global uncooled thermal camera (units) in commercial vs military applications [22]. . . . 8
1.7 Microbolometers and non microbolometers thermal camera (units) in commercial applications [22]. . . . 9
2.1 a) Schematic representation of fundamental optical excitation process in i) intrinsic, ii) extrinsic, iii) free carrier absorption in photon detector (adapted from [20], b) thermal detection mechanism. . . . 14
2.2 Comparison of relative spectral response of a photon detector and thermal detector. (adapted from [20]) . . . 14
2.3 A brief history of the infrared detectors and systems development [27]. 15
2.4 Schematic representation of a suspended microbolometer structure over ROIC substrate. . . . 18
2.5 Thermal loss mechanisms through the microbolometer via conduction and radiation loss. . . . 20
2.6 Thermal model of a microbolometer 21
2.7 The equivalent circuit for a electrical-thermal model of a microbolometer, If $G_{leg} >> G_{rad}$, then G_{rad} can be ignored and $G_{th} \approx G_{leg}$ (adapted from [49]). . . . 23
2.8 The electrical circuit representation of a microbolometer. . . . 24
2.9 Simplified schematic of a unit pixel readout circuit for a microbolometer. . . . 28
2.10 The observed noise as the sum of two major noise components $1/f$ and the Johnson noise a) as function of frequency b) as function of temperature. . . . 31
2.11 a) The contribution of the major noise sources to the total detector noise, b) The observed noise as the sum of all major noise components. 33
2.12 A typical design flow and procedure to optimize the performance specification of a microbolometer. . . . 36
3.1 Unit cell of diamond lattice (adapted from [60]). . . . 40
3.2 Schematic representation of both compressively strained and relaxed SiGe on a Si Substrate (adapted from [64]). . . . 41
3.3 The critical thickness versus Ge content (x) for pseudomorphic $Si_{1-x}Ge_x$ layers grown on bulk (100) Si [64]. . . . 41
3.4 Energy band structure with degenerated conduction and valence bands (a) Si and (b)Ge [67]. . . . 42

3.5 A schematic representation of the conduction and valence energy bands splitting of a compressively strained SiGe (b) in contrast to bulk Si (a). 43
3.6 a) Si/Si$_{1-x}$Ge$_x$ stacked structure with Si buffers and p-doped Si layers b) The schematic representation of energy band alignment showing Type-I quantum well formation in SiGe layer. 44
3.7 a) Cross sectional view of MQW structure b) Energy band diagram of device with three i-Si$_{1-x}$Ge$_x$ MQW under applied bias. 45
3.8 a) Cross sectional view of MQW structure b) Energy band diagram of device with three i-Si$_{1-x}$Ge$_x$ MQW under applied bias 47
3.9 Valence energy band with larger and smaller curvatures shapes, illustrates the density-of-states difference among two bands in a fixed energy interval. 51
3.10 Hole mobility in Si/SiGe MQW at 300 K: a) Relaxed SiGe layers, b) Strained SiGe layers using mobility model from (3.13), c) strained SiGe layers using Philips mobility model. 54
3.11 The regions-wise segregation of the device treated explicitly to model the carrier transport through the device 57
3.12 The 2D structure in SDE with three Si$_{1-x}$Ge$_x$ MQW with an active area of 17 μm × 17 μm 62
3.13 Discretization of simulation domain illustrating the rectangular meshing of the structure with the desired density and refinement near the Si/SiGe heterointerface. 63
3.14 Abrupt doping profile versus smoothed edge profile obtained by defining the decay length parameter. 63
3.15 Initial boron doping profile placement in the 2D structure illustrating the heavily doped top and bottom Si regions for the ohmic contacts, nearly intrinsic Si buffer regions and Si/Si $_{1-x}$Ge$_x$ MQW stack. 64
3.16 The flow chart of the self-consistent numerical framework and methodology implemented for the device simulation. 66
4.1 The schematic representation of fabricated device illustrating Ni silicide and double metal process for the contact pads. 70
4.2 Cross sectional TEM images of Si/Si$_{0.5}$Ge$_{0.5}$ stack (a,b) show sample without post annealing. (c,d) show samples after post annealing at 575℃. (e,f) show Si cap growth at 575℃ [104]. 71
4.3 a) HR-XRD (004) measured (black line) and simulated (red line) rocking curve of (004) plane of the Si/Si$_{0.5}$Ge$_{0.5}$ MQW structure b) Simulated Ge depth profile for the Si/Si$_{0.5}$Ge$_{0.5}$ stack comprising three quantum wells [103]. 72
4.4 Cross-sectional TEM image: (a) three stack Si/Si$_{0.5}$Ge$_{0.5}$ MQW showing the uniform layer thickness, (b) the pseudomorphic growth of the fully-strained Si/Si$_{0.5}$Ge$_{0.5}$ with the smooth and even interface surfaces, (c) EDXS image showing the compositional analysis of Si/Si$_{0.5}$Ge$_{0.5}$ MQW [103]. 73
4.5 Measured SIMS profile of the test structure with triple Si$_{0.5}$Ge$_{0.5}$ shows the boron doping concentration in the various device regions. . 74
4.6 The test field with various test structures used for dc probing to extract I-V characteristics. 75

4.7 The on-wafer dc characteristics measurement setup. 75
4.8 On-wafer dc measurement of eighteen test devices from two different wafers shows the measurement uniformity and the data consistency. . 76
4.9 The dominant physical phenomena effecting carrier's dynamics and transport modeling at T=298 K in the $Si_{0.6}Ge_{0.4}$ MQW device leading to progressive prediction accuracy. 77
4.10 Energy band diagram indicating the increase in ΔE_V for higher x in $Si_{1-x}Ge_x$. The extracted barrier heights are $\Delta E_V \sim 0.25$ eV, 0.35 eV, 0.45 eV and $\Delta E_C \sim 41$ meV, 49 meV, 51 meV for $x = 0.3$, 0.4 and 0.5 respectively. 78
4.11 Model optimization methodology for given Ge content and the candidate doping profiles 79
4.12 Various boron profiles incorporated in the $Si_{0.5}Ge_{0.5}$ MQW model. Profiles A and C show the abrupt transition whereas B and D are defined by specifying the decay lengths of 70 nm in the top Si buffer. . 80
4.13 Employing profile D, model reproduces the asymmetry in I-V characteristics of $Si_{0.5}Ge_{0.5}$ which is quite in-line with the measured I-V. . 80
4.14 The optimized candidate profiles used for fitting the model and measured I-V for $x=$ 0.3, 0.4 and 0.5. 81
4.15 The transfer characteristics of the model validated with the experiment data for $x = 0.3, 0.4, 0.5$ in 17 µm × 17µm Si/$Si_{1-x}Ge_x$ MQW at 298 K using the best optimum profiles (Figure 4.14) and estimated ΔE_V (Figure 4.10). 81
4.16 I-V fitting of the model and measured data extended over the entire temperature range of 278 K-323 K: a) $Si_{0.7}Ge_{0.3}$ MQW with $\Delta E_V \approx$ 252 meV and the doping profile A. b) $Si_{0.6}Ge_{0.4}$ MQW with $\Delta E_V \approx$ 357 meV and the doping profile B. c) $Si_{0.5}Ge_{0.5}$ MQW with $\Delta E_V \approx$ 459 meV and the doping profile C. 82
4.17 Variation of R over the temperature range for the nominal bias of 0.3 V, predicted by the model and validated with the experimental data in the $Si_{1-x}Ge_x$ MQW, a) for $x=$ 0.4 b) for $x=$ 0.5 for the various device active areas. Extracted E_a and TCR at 298 K for 0.3 V. 83
4.18 Extracted E_a for various Ge content and active areas at fixed bias of 0.3 V. The extracted values of E_a are in-line with the estimated band offset ΔE_V. 84
4.19 TCR increases with the Ge content x in MQW but remains same regardless of the active area for the given x in the Si/$Si_{1-x}Ge_x$ MQW. 84
4.20 Measurement of the electrical characteristics of the device with and without C-delta layers in Si/$Si_{0.6}Ge_{0.4}$ and Si/$Si_{0.5}Ge_{0.5}$ MQW. The presence of C-delta layers shows no significant difference in the measured electrical characteristics. 85
4.21 The model reproduces the asymmetric deviation in I-V characteristics of Si/$Si_{0.6}Ge_{0.4}$ MQW (without C-delta layers) matched to the measured data using the non-uniform doping profile given in the inset plot. 86
4.22 The carbon content does not cause explicit change in TCR. The roll-off in TCR over the bias range is attributed to the nonlinearity in R in consequence to the non-uniform doping. 87

4.23 Self-bias heating effect illustrated by ∂R in (a) $Si_{0.6}Ge_{0.4}$ MQW and (b) $Si_{0.5}Ge_{0.5}$ MQW. The larger R in $Si_{0.5}Ge_{0.5}$ MQW allows extended linear region of operation as compared to $Si_{0.6}Ge_{0.4}$ MQW. 87
4.24 Schematic representation of a) Single quantum well stack b) Double quantum well stack c) Triple quantum well stack. 88
4.25 a) I-V response for different number of well stacks containing 50 % Ge content at T=298 K. b) The model predicts the TCR roll-off which is in good agreement with the measurement attributed to the asymmetric nonuniform background doping. 89
4.26 TCR drops in the device with the $Si_{0.6}Ge_{0.4}$ MQW at a fixed bias of 0.3 V due to the elevated background doping level. 89
4.27 Quasi-fermi level shifts as a result of boron doping in MQW. 90
4.28 a) Boron doping in the $Si_{0.5}Ge_{0.5}$ MQW causes R to reduce from 8 MΩ to 93 KΩ for Vbias= 0.3 V at T=298 K b) TCR drops induced as a consequence of the heavily doped MQW $\approx 1{\times}10^{19}\,\mathrm{cm}^{-3}$. 90
4.29 In a wider well HH0 occupies the lowest ground state energy as compared to a narrow well, where the HH0 shifts to the higher energy level. 91
4.30 a) HH0 occupies the lowest energy as the well thickness increases, b)E_a and TCR increases due to increased effective barrier height for the fixed 40 % Ge content in the MQW for a wider well. 91
4.31 Schematic representation of the noise measurement setup. 93
4.32 Measured noise PSD for various Ge content at nominal bias of 0.5 V. 94
4.33 Measured noise PSD at various bias points: a) $Si_{0.7}Ge_{0.3}$ MQW where characteristic $1/f$ is seen below 50 Hz. b) $Si_{0.6}Ge_{0.4}$ MQW where characteristic $1/f$ is seen below 30 Hz. c) $Si_{0.5}Ge_{0.5}$ MQW where characteristic $1/f$ is seen below few Hz. 95
4.34 The measured noise PSD of $Si_{0.6}Ge_{0.4}$ MQW at fixed bias of 0.5 V. . 96

List of Tables

1 System specifications of some of the commercially available cooled IR systems from major manufacturers 6
2 Commercial uncooled infrared microbolometer arrays [20], [21] 7
3 Summarizing status, limitation and advantages of existing state-of-the-art system for LWIR detectors [47] 16
4 Comparison of principal types of uncooled IR systems [31]. 17
5 Performance specification of VO_x microbolometer from Raytheon [28] 35
6 Performance specification of a-Si microbolometer from ULIS [29] . . 35
7 Electron effective masses in bulk Si [78] and strained $Si_{1-x}Ge_x$ on (100) Si substrate [76, 79] at 300 K. 49
8 The extracted longitudinal m_z and transverse m_{xy} effective masses of holes in strained $Si_{1-x}Ge_x$ on (100) Si substrate as function of Ge content [77]. 50
9 Device structure Specifications 70
10 Comparative analysis with the other semiconductor based detectors. . 96
11 Performance summary of the $Si/Si_{1-x}Ge_x$ MQW in this work for different Ge contents and active areas. 96

List of Abbreviations

AC	Alternating Current
a-Si	Amorphous Silicon
BGN	Bandgap Narrowing
BiTe	Bismuth Telluride
BiSbTe	Bismuth Anitmonide Telluride
BST	Barium Strontium Titanate
BW	Band Width
C-delta	Carbon Delta
2-D	Two Dimensional
DC	Direct Current
DG	Density Gradient
DOS	Density-of-States
EDXS	Energy Dispersive X-ray Spectroscopy
FOM	Figure-of-Merit
FPA	Focal Plane Array
Ge	Germanium
HBT	Heterojunction Bipolar Transistor
HH	Heavy Hole
HR-XRD	High-Resolution X-ray Diffraction
i-MQW	Intrinsic Multi-Quantum Well
InAs	Indium Arsenide
InSb	Indium Antimonide
IR	Infrared
LH	Light Hole
LN_2	Liquid Nitrogen
LWIR	Long Wavelength Infrared
MCT	Mercury Cadmium Telluride
MOSFET	Metal-Oxide-Semiconductor Field-Effect Transistor
MQW	Multi-Quantum Well
MWIR	Mid-Wavelength Infrared
nBn	Ntype-Barrier-Ntype
NEP	Noise Equivalent Power
NETD	Noise Equivalent Temperature Difference
PIN	Ptype-Intrinsic-Ntype
PMN	Lead Magnesium Niobate
pm-SiGe	Polymorphous Silicon Germanium
PSD	Power Spectral Density
PZT	Lead Zirconium Titanate
QWIP	Quantum Well Infrared Photodetector
R	Resistance
RIE	Reactive Ion Etching
RMS	Root Mean Square
ROIC	Readout Integrated Circuit
RPCVD	Reduced Pressure Chemical Vapor Deposition
RMS	Root Mean Square
SDE	Sentaurus Device Editor

SF	Stacking Fault
SiGe	Silicon-Germanium
SNR	Signal-to-Noise Ratio
SO	Spin-Orbit Split-off
SOI	Silicon on Insulator
SRH	Shockley-Read-Hall
SWAP	Size Weight and Power
SWB	Sentaurus Work Bench
SWIR	Short Wavelength Infrared
TCAD	Technology Computer-Aided Design
TCR	Temperature Coefficient of Resistance
TEM	Transmission Electron Microscopy
ToF-SIMS	Time-of-Flight Secondary Ion Mass Spectroscopy
T2SLs	Type-II Supperlattices
VCCS	Voltage Controlled Current Source
VO_x	Vanadium Oxide
ZnS	Zinc Sulphide
ZnSe	Zinc Selenide

1 Chapter 1

Introduction

1.1 Infrared Imaging

The word "infrared" (IR) refers to a broad portion of the electromagnetic spectrum that spans a wavelength range from 1 μm to beyond 30 μm. The segmented IR regions used in thermal imaging are short wave infrared (SWIR, 0.9 μm-2.5 μm), mid-wave infrared (MWIR, 3 μm-5 μm) and long wave infrared (LWIR, 8 μm-14 μm), as presented in Figure 1.1. IR thermal imaging often referred as 'thermography' has undergone a remarkable evolution over the last few decades. The thermal imaging is ubiquitously extending its application beyond the military realm into the diverse areas such as thermography (predictive maintenance, building inspection [1]), medical imaging [2], industrial process control [3], automotive safety [4] and consumer electronics [5, 6].

Unlike the visible light camera, the IR camera does not require any visible light source for imaging rather it converts the IR radiation (heat) into the visible images, hence aids to "see the unseen" in complete darkness. The SWIR band is useful for imaging scenes that reflect light i.e. sunlight, moonlight, starlight and night glow, same as in the case of visible light imaging. The MWIR and LWIR wavebands are

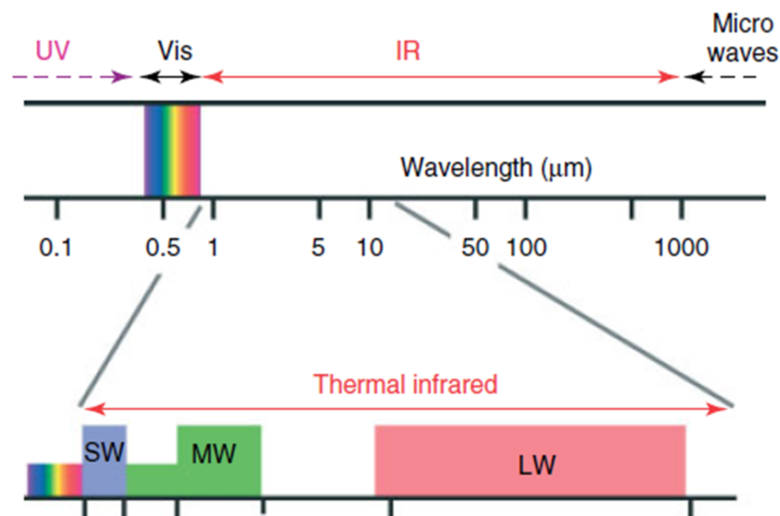

Figure 1.1: IR spectrum segmentation used for IR imaging technologies [7].

important for the imaging of objects that emit thermal radiation. LWIR and MWIR imaging system operate in entirely passive mode, require no external visible light source as the image sensor detects the thermal energy emitted by the object. The temperature and the emissivity of an object mainly determine how bright an object appears to the thermal imager, therefore, eliminates the need of a visible light source for vision. The hotter the body temperature is, the more brighter it appears to the thermal image sensor. Likewise, the emissivity of an object is a physical property which determines how efficiently heat is being radiated. For instance, cloth appears darker in a thermal imager as compared to skin, since cloth has less emissivity compared to skin when both are exactly at the same temperature. The hotter object emits energy which lie at shorter wavelengths (λ). The spectral exitance ($M_\lambda(T, \lambda)$) of a blackbody at various temperatures was first introduced by Plank's theory shown in Figure 1.2. The peak of the emitted energy from a blackbody source at 300 K at $\lambda = 9.7\,\mu m$ whereas a source at 1000 K the peak emitted energy occurs at $\lambda = 2.9\,\mu m$. Thus, the LWIR image sensors are suitable for imaging at room temperature (people, building), while MWIR are good for imaging objects at much higher temperature (hot engines, exhaust gases).

The choice of wavelength band for IR imaging is explicitly determined by the atmospheric conditions. For instance, haze and smoke cause less scattering in LWIR and MWIR band, whereas fog and clouds cause more scattering due to comparable particle size and the IR wavelength.

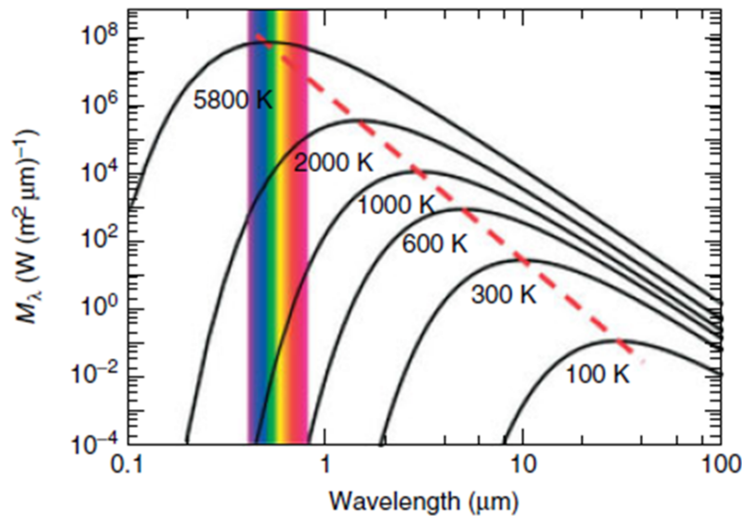

Figure 1.2: The peak curves for blackbody radiation based on Plank's theory [7].

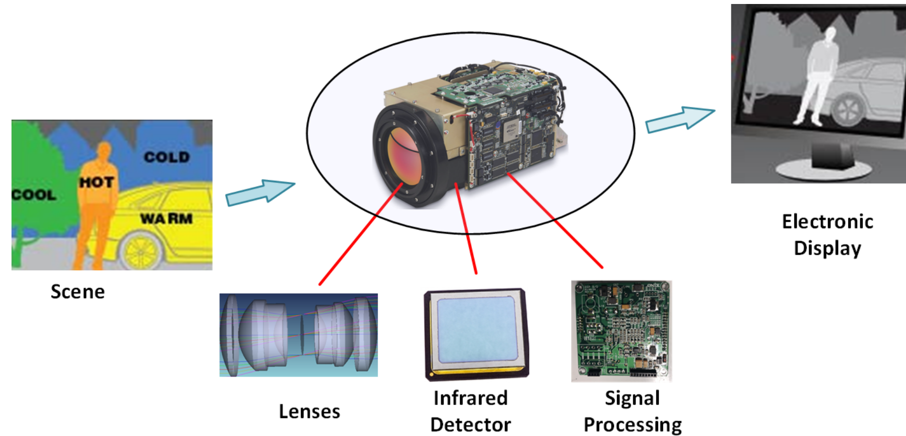

Figure 1.3: Basic components of an IR imaging system, the camera core is taken from [8].

1.2 Basic Components of an IR Imager

Typically, the IR camera mainly comprises of the components illustrated in Figure 1.3. The IR energy is emitted from an object proportional to its temperature.

(i) Lens System: Lenses are used to focus the IR radiation from the scene onto the detector elements. Silicon (Si), germanium (Ge) and zinc selenide (ZnSe) are the common material types used for these lenses. The focal length of lenses are designed based on the intended use of thermal camera.

(ii) Basic Detection System: The detector absorbs the IR energy and converts the detected radiation into the electrical signal. Readout integrated circuit (ROIC) improvises the electrical output from the detector and provides digital or analog output.

(iii) Signal Processing Unit: The output from detection unit is transformed to produce the thermal image by the peripheral electronics. Moreover, the thermal image is also further processed by the signal processing unit to enhance the image quality e.g. by non-uniformity corrections and adaptive contrast enhancement.

(iv) Electronic Display: Image generated by the signal processing element can be viewed on external display or direct view display on the IR camera. The display can be colored or monochromatic. Generally, color displays are color-coded to depict the temperature difference through the field of view of the imager.

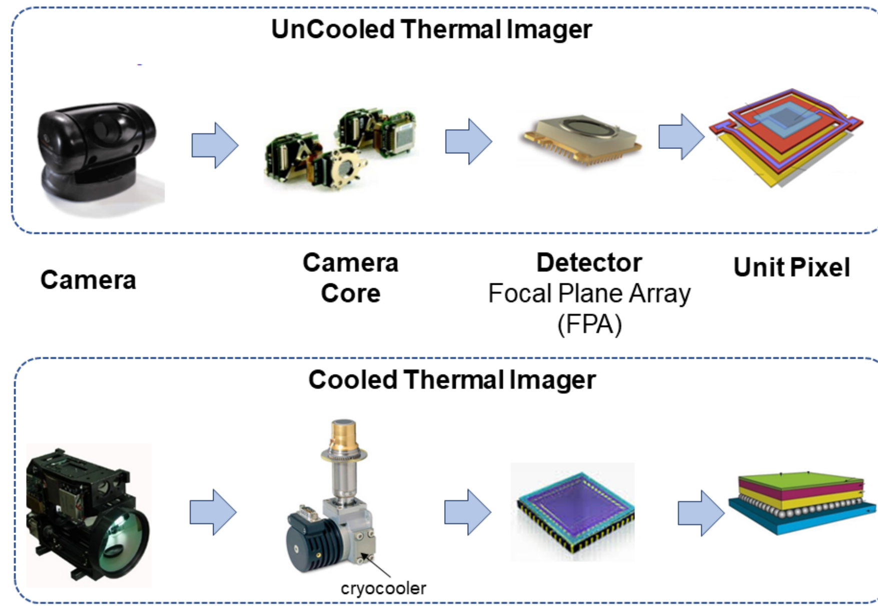

Figure 1.4: The difference between cooled and uncooled IR camera from technology perspective [9] [10] [11].

1.3 IR Detector Technologies

IR imaging systems have turned into mainstream instruments in various commercial and military domains. Thermal imaging systems have evolved into very portable, easy to use and reasonably priced instruments. From technology perspective IR imaging have two main categories: cooled and uncooled. Figure 1.4 shows the component wise breakdown of the IR technology. The cooled technology incorporates the IR detectors with required operating temperatures far below room temperature achieved by combined cryocooler. Mostly quantum well infrared photon (QWIP) detectors require cooling between 50 K - 200 K. The cooled cameras are extraordinarily sensitive to IR radiation due to substantially reduced thermal noise but at the expense of bulky size and more weight. These are highly sensitive and can detect slightest temperature difference, employed in MWIR and LWIR band for imaging where there is high thermal contrast. The imaging speed measured in frame per second (Hz) of cooled cameras are much higher, as well as the magnification capabilities are higher. Uncooled technology has become an excellent alternative to the expensive cooled system for many commercial and industrial purposes. Uncooled IR detectors operate at nominal room temperature 298 K ∼ 300 K. As they do not

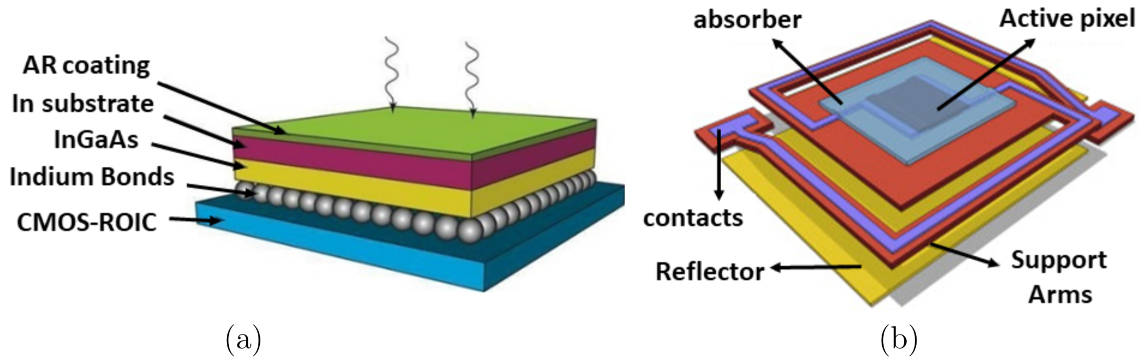

(a) (b)

Figure 1.5: Schematic depiction of a unit pixel in a) photon detector using indium bumps and flip-chip technology for hybridization to the interface ROIC [12], b) thermal detector monolithically integrated and suspended over the ROIC [13].

require any external cooling unit, they offer exceptional benefits in maintainability as well as significant reduction in size, complexity, and cost. Uncooled camera are mostly employed for imaging in LWIR bands where most of IR energy is emitted by terrestrial temperature targets. Figure 1.5 depicts the typical unit pixel architecture of photon and thermal FPAs.

1.4 Figure-of-Merits (FoM)

Listed below are particularly important figure-of merits to determine and compare the performance of any imaging detector [7].

(i) Responsive Area of Pixel (A_D): The geometric area of single pixel, typically, 25 µm × 25 µm or 17 µm × 17 µm for the thermal detector and 30 µm × 30 µm, 15 µm × 15 µm or even smaller for the photon detectors.

(ii) Time Constant (τ): To characterize the response time of the detector in µs or ms units .

(iii) Spectral Responsivity (R_v, R_i): Ratio of detector signal voltage or current to incident power/radiant flux on detector area at wavelength λ, measured in VW^{-1} or AW^{-1} for voltage or current responsivities, respectively.

(iv) Noise Spectral Density (V_N, I_N): Detector noise voltage or current density with respect to the square root of output bandwidth $\sqrt{BW}$ expressed in $V/\sqrt{Hz}$ or $A/\sqrt{Hz}$.

(v) Noise Equivalent Power (NEP): NEP is equal to the noise spectral density divided by the responsivity $V_N/\ R_v$ or $I_N/\ R_i$ expressed in W/$\sqrt{\text{Hz}}$.

(vi) Noise Equivalent Temperature Difference (NETD): NETD is the defined as the temperature change of a target that results signal-to-noise (SNR) equal to one, typically expressed in mK scale.

(vii) Specific Spectral Detectivity (D^*): Reciprocal of the spectral noise equivalent power normalized to eliminate the detector area, and the bandwidth of signal, expressed in cm$\sqrt{\text{Hz}}$W^{-1}.

(viii) Operating Temperature (T_D): Operating temperature of the detector specified in Kelvin, K.

Some of specifications of the cooled IR detectors produced by the renowned manufacturers are enlisted in Table 1, which shows that the smaller pixel size is one of the driving forces in the latest detector developments.

Table 1: System specifications of some of the commercially available cooled IR systems from major manufacturers

Company	**FPA format**	**Pitch (µm)**	**Detector material**	**Spectral range (µm)**	**Temp. (K)**	**NETD (mK)**
Raytheon [14]	1024×1024	30	InSb	0.6-5.0	50	23
	2048×2048	25	HgCdTe	0.6-5.0	32	
	2048×2048	15	HgCdTe/Si	3.0-5.0	4-10	
	2048×1024	25	Si:As	5-28	6.7	
Teledyne [15]	4096×4096	10	HgCdTe	1.0-5.4	37	
	2048×2048	18	HgCdTe	1.0-2.5	77	
Sofradir [16]	1280×1024	15	HgCdTe	3.7-4.8	77-110	18
	640×512	20	QWIP	8.0-9.0	73	31
	640×512	24	HgCdTe	MW/LW	77-80	15-20
Selex [17]	1024×768	16	HgCdTe	3-5	up to 140	15
	640×512	24	HgCdTe	8-10	up to 90	24
AIM [18]	640×512	15	HgCdTe	8-9		40
	384×288	40	Type II SL	MW		35/25
SCD [9]	1280×1024	15	InSb	3-5	77	20
DRS [19]	2048×2048	18	Si:As	5-28	7.8	
	2048×2048	18	Si:Sb	5-40	7.8	

Table 2: Commercial uncooled infrared microbolometer arrays [20], [21]

Company	Bolometer type	FPA format	Pitch (μm)	NETD (mK)
BAE	VO_x	640×480	17	50
		1024×768	17	
		640×480	12	
L-3	VO_x	320×240	37.5	50
	a-Si	640×480	30	50
	a-SiGe	1024×768	17	30-50
DRS	VO_x	320×240	25	35
	VO_x	320×240	17	50
	VO_x	1024×768	17	
		640×512	10	50
Raytheon	VO_x	320×240	25	30-40
		640×480	17	50
ULIS	a-Si	640×480	25	60
		1024×768	17	60
SCD	VO_x	384×288	17	35
		640×480	25	50
NEC	VO_x	640×480	23.5	75
Seek	VO_x	206×256	12	70
Flir	VO_x	80×60	17	100
Fraunhofer	a-Si	640×480	25	100
Mitsubishi	SOI diode	2000×1000	15	84
Toshiba	pn-Si	320×240	22	40

1.5 Outlook on Microbolometers

Photon detectors have been foremost choice for IR imaging technology since the beginning of twentieth century. However, the cooling requirement for the proper operation of photon detectors makes them bulky, heavy, expensive and inconvenient to use. In contrast to photon detectors, thermal detectors were comparatively less favored for commercial purpose in general and military systems specifically due to slow response time and less sensitivity. The Bell Laboratories has developed the first thermistor based microbolometer [23] [24]. The extensive research has been carried out in the 1970s for development of uncooled infrared detectors [25]. The research focus was mainly on the development of Vanadium oxide (VO_x) micromachined mi-

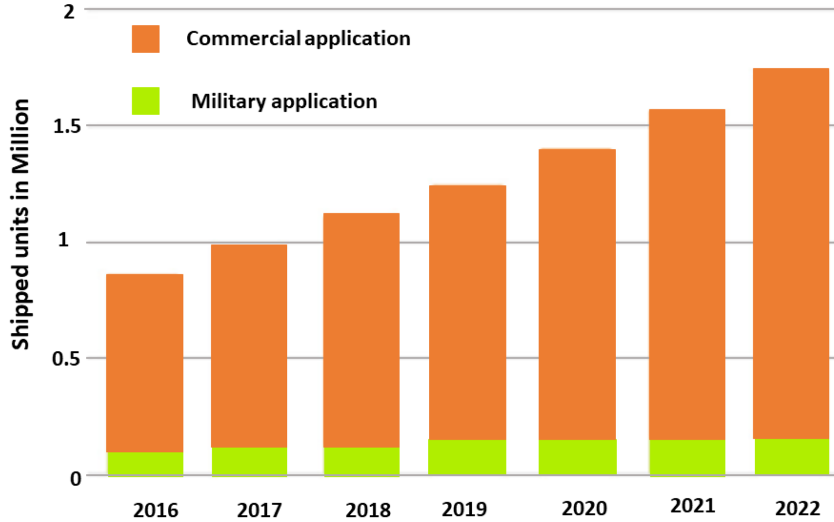

Figure 1.6: Global uncooled thermal camera (units) in commercial vs military applications [22].

crobolometers [Honeywell] and ferroelectric barium strontium titanate (BST) [Texas Instrument]. BST technology has its limitation of pixel size (50 µm), moreover, the need of mechanical chopper lowers the sensitivity of camera. Additionally, BST require thermoelectric cooling to stabilize the electrical polarization [10]. Subsequently, amorphous silicon (a-Si) turned into an attractive alternative for uncooled IR imaging in the 1990s owing to ease of its fabrication in existing Si foundries. Presently, VO_x based microbolometers are the dominant choice for the uncooled detector technology due to their lower production cost as compared to the other two technologies [26]. There is an ever growing demand in field of thermography (building inspection, agriculture, gas imaging, and pipeline inspection), personal vision systems, security and surveillance market. Thermography is still the dominant field while the surveillance in the public sector including traffic,parking places, etc, is also uprising demands in the market. Moreover, night vision in the cars including autonomous vehicles have boosted the uncooled market. In order to reduce the cost for consumer electronics, the new manufacturing and processing techniques are introduced such as wafer-level optics, wafer-level packaging.

The Yole report published in 2017 [22] shows that market trends in uncooled camera demands in commercial application are growing vastly every year as presented in Figure 1.6. Most of the market shared is captured by the VO_x microbolometer based uncooled detectors as indicated in Figure 1.7, thanks to the smaller pixel pitch

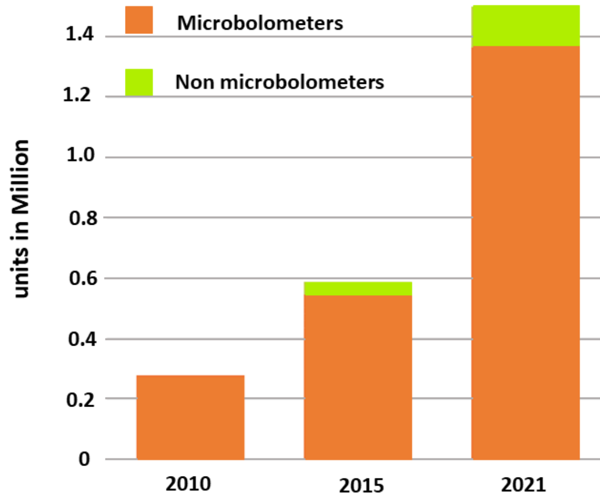

Figure 1.7: Microbolometers and non microbolometers thermal camera (units) in commercial applications [22].

and larger format arrays. Nevertheless, the other type of thermal detectors, thermopiles and pyroelectrics limited to their smaller FPA (32 × 32) and larger pixel pitch are also employed to fulfill the market demand which do not require very high sensitivity such as smart home or buildings applications.

1.6 Motivation and Objectives

In recent years the efforts are made for technical evolution for microbolometer in four different domains: IR optics, at the pixel level, ROIC integration, and packaging level. In general, the main motivations are to upgrade the performance, to reduce cost and to increase the integration capabilities. Newer paradigms at pixel level involve pixel size reduction, new materials, and new design to enhance the detection and integration capability with ease of fabrication [27].

For an uncooled thermal detector, the key design trade-off is between its sensitivity and the response time. Thermal sensitivity of microbolometer is defined as the change in resistance caused by the temperature change in the detector in consequence to the absorbed IR radiation and quantified as the temperature coefficient of resistance TCR of the detector material. To enhance the performance of the detector, higher TCR, as well as, lower noise is desired. Commercially available microbolometers employing VO_x and a-Si have TCR limited to 2-3 $\%K^{-1}$ [28] [29]. Silicon-germanium (SiGe) material has attracted growing interest as a promising candidate

for the long-wave infrared (LWIR) microbolometers. Amorphous $Si_{1-x}Ge_x$ film with embedded nanocrystals has been reported in [30] as the largest TCR of -6.6 %K^{-1} but the measured device noise is significantly larger than that of both VO_x [31] [32] and a-Si [33] [34] [35]. In contrary to amorphous $Si_{1-x}Ge_x$ film, monocrystalline SiGe enhances the thermal sensitivity and signal-to-noise ratio due to the inherent fringe benefit of ease of bandgap tailoring. Furthermore instead of single layer of Si or $Si_{1-x}Ge_x$, epitaxially grown $Si/Si_{1-x}Ge_x$ multi-quantum-well (MQW) structure has gathered much attention due to the fact that higher TCR can be obtained by optimizing device design parameters such as the number of wells, well width, and the amount of Ge content in the wells [36]. For a fixed amount of Ge content (x) in $Si/Si_{1-x}Ge_x$ MQW, either increasing number of wells or wider well layer can enhance TCR. Although higher Ge content is known to increase TCR values, all efforts so far have been limited to Ge content below 35 % in an epitaxially grown MQW structure [37] [38]. In fact, there are practical challenges involved in processing $Si_{1-x}Ge_x$ with higher Ge content such as the strain relaxation of the epitaxial $Si_{1-x}Ge_x$ layers which results in elevated surface roughness and defect formation. So far, there have not been systematic studies to investigate the effect of the device design parameters (higher Ge content, number of wells, doping concentration) in a single crystalline $Si/Si_{1-x}Ge_x$ MQW.

In order to design and develop a $Si/Si_{1-x}Ge_x$ MQW structure incorporating a higher Ge content (>35 %), an extensive study of electronic transport properties is required to optimize the detector for the desired performance. The computer-aided design (TCAD) tool can be used to obtain a priori estimate of the detector characteristics. These estimates can be used to investigate the device design challenges and optimization issues. The primary requirement for such modeling methodology is to reproduce the actual characteristics of a structure under consideration. They must be predictive models, not overly idealized. The theoretical analysis based on the quantum mechanical solution for a Si/SiGe MQW with Ge content 25 % and 40 % is reported in [39]. Additionally, a numerical model employing drift-diffusion formulation verified experimentally for 30 % Ge for such a structure is presented in [40]. However, the heterointerface boundary which dominates the carrier transport is not treated explicitly in either of any case. As a matter of fact, the thermionic emission

mechanism is considered important for accurate modeling, particularly in isotype heterojunction with high barriers [41].

This thesis presents a comprehensive physical device model to investigate the electrical characteristics, device design challenges and design trades-off involved in $Si/Si_{1-x}Ge_x$ MQW detector. The aim of the research is to develop the integrated modeling framework to investigate the effect of interdependent design variables such as Ge content and the doping profiles, the thickness and number of quantum wells on the device electrical characteristics. For this purpose, description of the carrier's dynamics governing the device behavior, specifically, the carrier density within the quantum wells and the thermionic transport across the heterointerface are explicitly considered for a physical model development. The simulation results of the proposed model are validated with the experimental data. The simulated and the experimental data are found consistent over a wide range of Ge content varied from 30 % up to 50 %. The primary objective of this work is to optimize Ge content in $Si/Si_{1-x}Ge_x$ MQW detector to achieve desired thermal sensitivity measured in terms of TCR for a potential microbolometer application.

1.7 Thesis Outline

This dissertation can be divided into two main parts: modeling and design framework (Chapter 3), experimental characterization and the model verification (Chapter 4).

Following the motivation and objectives are given in Chapter 1 of this thesis, Chapter 2 starts with a brief review of infrared detection mechanisms and literature review. The fundamentals of a resistive microbolometer design, the performance parameters to characterize a infrared detector, and key design trade-offs and challenges are discussed in detail.

Chapter 3 is dedicated to the $Si/Si_{1-x}Ge_x$ MQW detector design and physical modeling of carrier transport in the device, investigating the effect of various transport parameters and their calibration. The chapter also covers the self-consistent numerical model and its implementation in Sentaurus TCAD to investigate the physical phenomena effecting carrier dynamics.

The physical device model is verified and validated by comparing the simulation

results to the experimental data in Chapter 4. The experimental validation aids to optimize and improve the model accuracy. As the result of the experimental validation, the predictive capability of the model is employed to optimize the design parameters of the device to enhance the performance. The details of the device fabrication process and characterizations are also presented in Chapter 4.

Chapter 5 summarizes and concludes the work. Some potential directions for the further work to improve the modeling are suggested along with some required measurements to characterize the Si/SiGe MQW as a potential candidate for a microbolometer.

2 Chapter 2

An Overview of Resistive-Microbolometer

In this chapter, a review of fundamentals and principal detector operation of resistive microbolometers are presented. Key design parameters and trade-offs dictating the overall detector performance metric are briefly discussed.

2.1 Infrared Detection Mechanisms

2.1.1 Photon Detection

The photon detectors are classified into various types such as intrinsic, extrinsic, quantum well and photo-emissive devices [42], illustrated in Figure 2.1-a. The detection mechanism is based on bandgap engineering of material such that free charge carriers are generated based on the wavelength of incoming IR radiation. The absorbed IR radiation within the semiconductor material interacts with either bound to lattice atoms or impurity atoms or free electrons. Consequently, the output electrical signal is generated from electronic redistribution which is further processed by the integrated readout circuit (ROIC). This transition mechanism is endowed with fast response and high signal-to-noise ratio (SNR), which requires the cryogenic cooling to prevent the thermal generation of carriers. The photon detectors exhibit selective wavelength dependent response per unit radiation.

2.1.2 Thermal Detection

The incident IR radiation absorbed by a thermally isolated detector resulting the temperature change of the detector. Subsequently, this temperature variation is translated into a change in the electrical parameters (such as resistance or capacitance) to produce the output signal. Unlike photon detection, the output signal is not dependent upon the photonic nature of the incident radiation in thermal detection. Response of the thermal detectors are generally wavelength independent i.e. output signal does not depend upon the spectral content of incoming radiation rather on its radiant power. Figure 2.2 illustrates typical spectral response of a photon detector in comparison to a thermal detector. Moreover, a thermal detectors

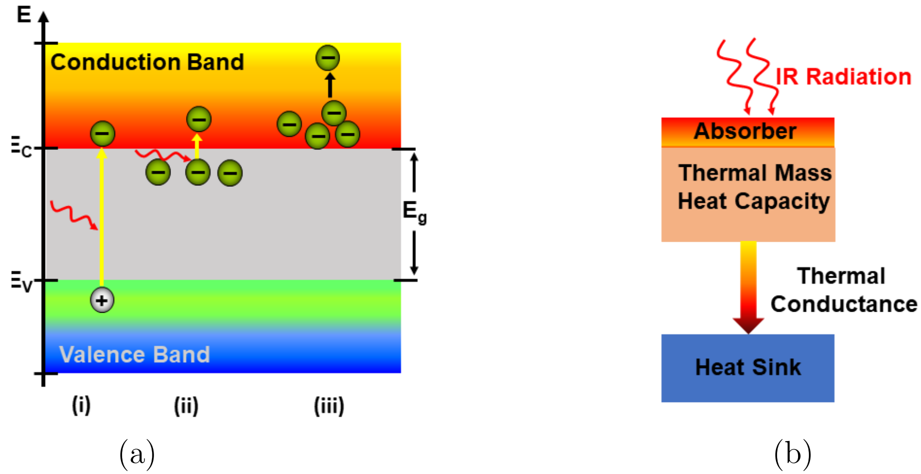

(a) (b)

Figure 2.1: a) Schematic representation of fundamental optical excitation process in i) intrinsic, ii) extrinsic, iii) free carrier absorption in photon detector (adapted from [20], b) thermal detection mechanism.

does not require cooling and can operate at room temperature. Broadly speaking, the thermal detectors provide wavelength independent, inexpensive and ease of detection at room temperature but at the expense of slow response and less sensitivity as compared to the photon detectors [20]. They are widely used in applications which do not require low noise and high speed operation.

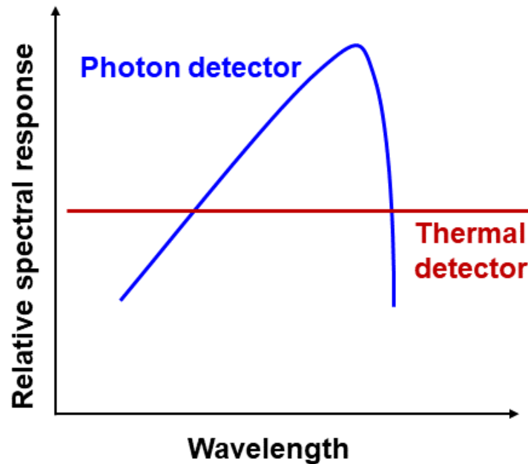

Figure 2.2: Comparison of relative spectral response of a photon detector and thermal detector. (adapted from [20])

The three main approaches are established in thermal detection: namely pyroelectric, thermoelectric and microbolometers. The pyroelectric detectors are based on a change in the internal electrical polarization due to its ferroelectric nature.

Under thermal drive due to absorbed IR radiations, the voltage across capacitor changes in consequence to the internal electric field change. The thermopile based thermoelectric detectors using the Seebeck effect between dissimilar metal produce voltage change across its terminals in response to the temperature difference. Due to their limited responsivity and less noise, there are only few efforts towards their development. The resistive-based microbolometer sensing principle relies on a change in electrical resistance of a detector (thermistor) caused by the change in temperature due to absorption of IR radiation. It is suspended over the readout substrate to provide thermal isolation.

2.2 Materials and System Developments

Principally, the growth and developments in thermal imaging applications in military, as well as, civilian domain is spanned over four generation systems. First generation includes scanning systems, second generation includes staring systems, third generation includes staring systems with large format FPAs + dual color mode, and fourth generation includes staring systems with larger format FPAs + multi-color mode, benchmarked in Figure 2.3. Additionally, the innovative materials research has profoundly impacted the infrared imaging development as shown in Figure 2.3.

Various materials have been investigated as potential candidates to improve the

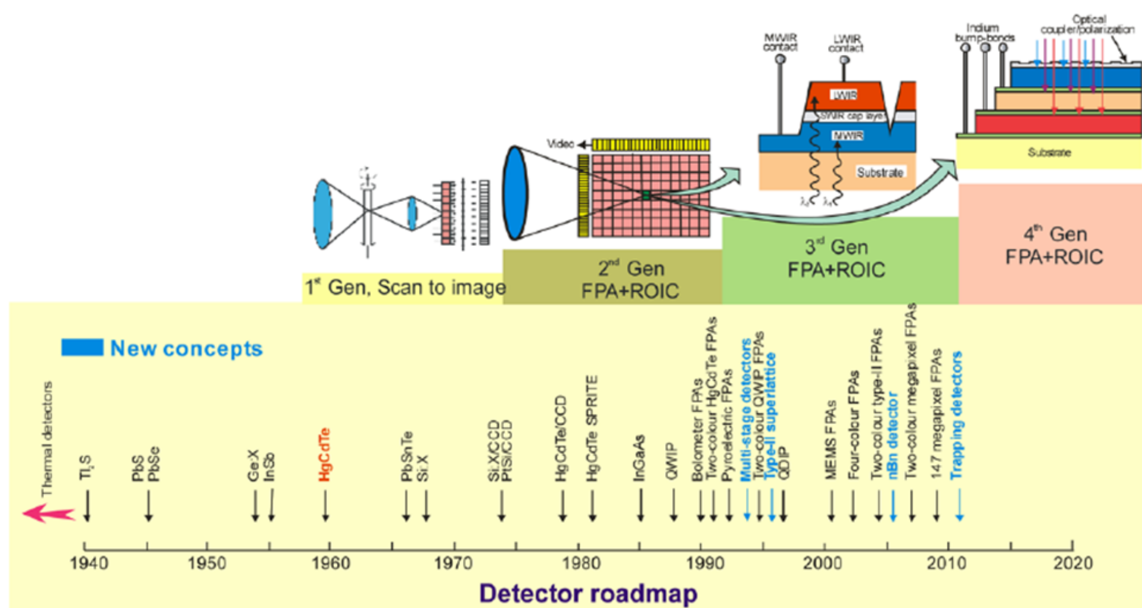

Figure 2.3: A brief history of the infrared detectors and systems development [27].

performance of the IR camera. Many materials have been investigated in the domain of photon detectors, mainly classified into two broad categories: materials from III-V and II-VI groups of the periodic table. Earlier, III-V binary alloys (InAs and InSb) were employed in MWIR band, followed by the development of ternary alloys composed of II-VI and IV-VI. Later on, HgCdTe (MCT) have inspired the IR detector development over the span of four decades. In the recent years, the bandgap engineering of various compounds lead to the considerable progress towards the innovative detector design. For instance, Type-II superlattices (T2SLs) and nBn detectors are two new emerging architectures with very promising features [27].

Within the domain of thermal detectors the material research involved limited material choice in comparison to photon detectors. For pyroelectric detector are lead zirconate titnate (PZT), barium strontium titanate (BST) and lead magnesium niobate (PMN) [42]. 2D thermopile polysilicon based arrays have been reported in [43], whereas some other works reported BiTe and BiSbTe based thermoelectric arrays [44]. For resistive-microbolometer, amorphous silicon (a-Si) [45] and vanadium oxide (VO_x) [46] are the two most commonly used detector materials.

Table 3: Summarizing status, limitation and advantages of existing state-of-the-art system for LWIR detectors [47]

	Bolometer	HgCdTe	Type II SLs	QWIP
Maturity	TRL9	TRL9	TRL2-3	TRL 8
Status	applications requiring medium to low performance	applications requiring high performance	Research and development	Commercial
Limitation	Low sensitivity Long time constants	susceptible to fabrication variations	Requires a significant investment $\geq$ \$100M	Narrow bandwidth
Advantages	Low cost and require no active cooling	Near theoretical performance	better than HgCdTe at 14um cut-off, commercial III-V fabrication techniques	Low cost applications very uniform material

Note: TRL-technology readiness level

In general, the evolution of IR technology paved the path to follow the SWaP

Table 4: Comparison of principal types of uncooled IR systems [31].

Specifications	Resistive bolometer	Hybrid ferroelectric	Monolithic thermoelectric
Responsivity	High	High	Low
Bias required	Yes	Yes	No
Chopper reqires	No	Yes	No
Response time (ms)	10-20	15-20	20-30
Dynamic Range	High	Low	High
Array format	Larger	Smaller	Smaller
Possibility of performance improvement	High	Low	Medium

Note: ferroelectric is bias-enhanced pyroelectric.

(size, weight and power) trend. Extensive efforts have been made to decrease the size, weight and power consumption of systems, thereby reducing the system costs. Foremost,the smaller pixel pitch in detector and ROIC designs will aid to fabricate larger format FPAs in the smaller area. Moreover, smaller pixel size will also eventually reduces the cost of optics. The cooling assembly and mechanisms in the cooled IR detectors are costly, bulky and requires cooling down time which also hinders the system speed. Increasing the operating temperature of detectors or new detector designs operating at room temperature will eliminate the need of cooling. These reductions would have profound impact on reducing overall size, weight and cost of IR systems. Table 3 summarizes briefly the state-of-the-art IR detector technologies with their advantages and limitations. The general comparison of the major uncooled detector types are enlisted in Table 4 which indicates that the resistive microbolometer is viable detector choice since it has more room for improvement.

2.3 Basic Principal and Detection Mechanism

Figure 2.4 depicts the simple schematic drawing of a typical resistive microbolometer unit pixel. A typical pixel consists of suspended and thermally isolated stack of thin films connected to ROIC pads through two long supporting legs. The sup-

porting legs are essential for thermal isolation of of IR sensitive layers from the substrate. Moreover, vacuum encapsulation is used for packaging to reduce thermal conductance through convection mechanism. The top layer of the stack is known as an absorber layer to enhance the incident IR absorption efficiency, thereby, the temperature of the underneath temperature-sensitive layer increases. To enhance the absorption further, a reflector layer on the substrate below the active layer is also included which eventually reflects back the incident IR radiation not fully absorbed by the detector, therefore, increases the IR coupling efficiency.

2.3.1 Temperature-Dependent Resistance

The resistivity of a temperature sensitive layer labeled as an active microbolometer in Figure 2.4, is strongly temperature-dependent and IR sensitive. Thus, the temperature variation due to incident IR radiation changes the overall electrical resistance of the active microbolometer. The resistance change is measured electrically by applying bias current or voltage through the ROIC.

For a metal thermal detector, temperature-dependent resistance $R(T)$ is expressed as the linear function of temperature change ΔT, given below:

$$R(T) = R_0(1 + \alpha\Delta T) \tag{2.1}$$

R_0 is detector resistance at ambient temperature T_{sub}. ΔT is the difference of

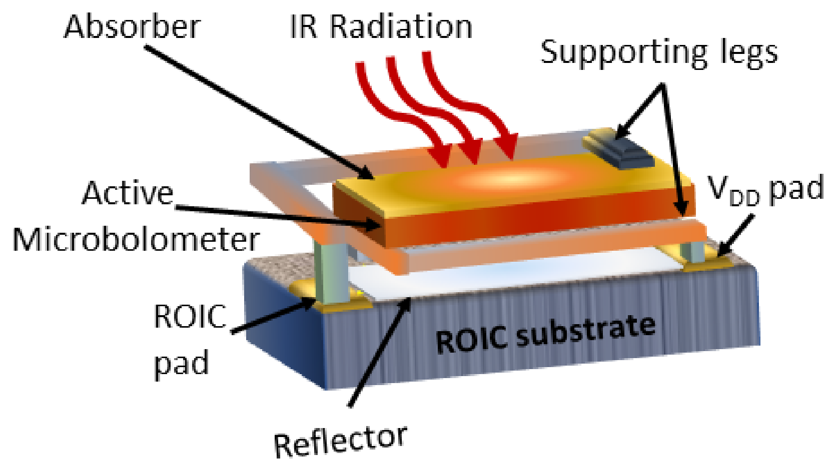

Figure 2.4: Schematic representation of a suspended microbolometer structure over ROIC substrate.

microbolometer temperature (T) due to absorbed radiation and the substrate temperature (T_{sub}) as:

$$\Delta T = T - T_{sub} \tag{2.2}$$

$R(T)$ in the metals increases as the temperature is increased due to increased phonon scattering which causes mobility degradation. For a semiconductor based microbolometer, $R(T)$ is approximated as a function of thermal activation energy (E_a) [48]

$$R(T) = R_0 \exp\left(\frac{E_a}{k_B T}\right) \tag{2.3}$$

where k_B is the Boltzmann's constant. Equation (2.3) shows that $R(T)$ depends exponentially on the temperature and it decreases as the temperature increases.

2.3.2 Temperature Coefficient of Resistance

The temperature coefficient of resistance TCR is defined as the percentage change in the resistance per kelvin change in the temperature. TCR is denoted by α, measured in %/K and expressed as follows:

$$\alpha = \frac{1}{R}\frac{dR}{dT} \tag{2.4}$$

TCR is positive in the case of metal thermal detectors, implies that the temperature dependent resistance increases at higher temperatures, whereas, TCR is negative in the case of semiconductors. Taking natural logarithm of (2.3) and then derivative with respect to T, we obtain TCR for a semiconductor based microbolometer as follows:

$$\frac{1}{R}\frac{dR}{dT} = \alpha = -\frac{E_a}{k_B T^2} \tag{2.5}$$

2.3.3 Thermal Conductance

Thermal Conductance (G_{th}) represents the thermal loss through the microbolometer under various heat transfer mechanisms. There are three fundamental thermal loss mechanisms via heat transfer processes namely, convection, radiation and conduction. Since microbolometers are encapsulated in vacuum package, therefore, the convection loss can be ignored. The major thermal loss happens via thermally

conducting legs of microbolometer, whereas radiation loss also contributes to the thermal loss [7], as illustrated in Figure 2.5. Hence the total thermal conductance can be expressed as:

$$G_{th} = G_{leg} + G_{rad} \tag{2.6}$$

Principally, the spectral exitance of a blackbody determines by the Plank's law given as [7]:

$$M_{\lambda}(T, \lambda) = \frac{2\pi hc^2}{\lambda^5(e^{(hc/\lambda k_B T)} - 1)} \ [\mathrm{W.m^{-3}}] \tag{2.7}$$

The Stefan-Boltzmann's law is applied to estimate the radiant flux per unit area, termed as total exitance M (W.m^{-2}) of a blackbody. Thus M in case of any object at ambient temperature T, can be given as follow:

$$M(T) = \int_0^{\infty} M_{\lambda}(T, \lambda) d\lambda = \sigma_B T^4 \tag{2.8}$$

where $\sigma_B = 5.607 \times 10^{-8}\,\mathrm{W.m^{-2}K^{-4}}$ is the Stefan-Boltzmann's constant. G_{rad} for a microbolometer can be determined by differentiating the Stefan-Boltzmann's law with respect to temperature, multiplied by twice the microbolometer area as both the top and bottom sides of the microbolometer will radiate heat and emissivity of object ε ($\varepsilon = 1$ in case of blackbody).

$$G_{rad} = 2\left(\frac{dA_{bolo}\varepsilon\sigma_B T^4}{dT}\right) = 8A_{bolo}\varepsilon\sigma_B T^3 \tag{2.9}$$

For a microbolometer operating at $T = 300\,\mathrm{K}$, with nominal device area of $(17\ \mu\mathrm{m})^2$, Equation (2.9)) $\implies G_{rad} = 3.54 \times 10^{-9}\,\mathrm{W.K^{-1}}$.

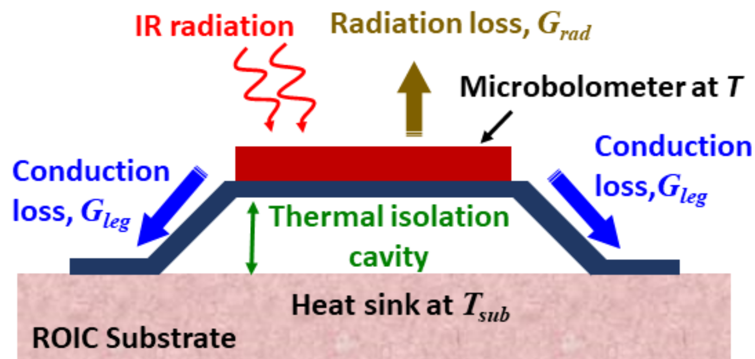

Figure 2.5: Thermal loss mechanisms through the microbolometer via conduction and radiation loss.

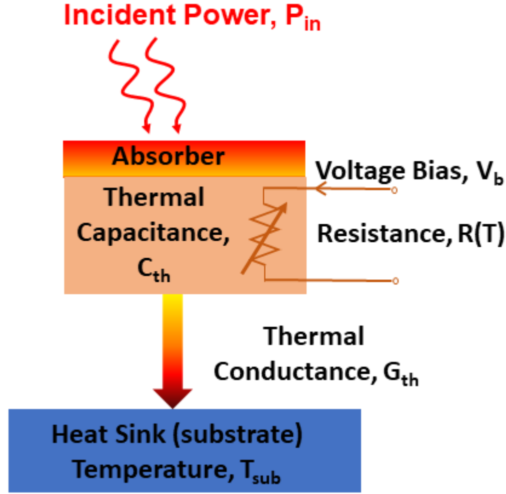

Figure 2.6: Thermal model of a microbolometer .

The thermal loss contribution via heat conduction through the legs can be determined by simplified heat transfer model [7]

$$G_{leg} = \lambda_c \frac{A_{leg}}{l_{leg}} \tag{2.10}$$

λ_c is the thermal conductivity of the material used as the supporting legs of microbolometers, A_{leg} is the cross-sectional area of the leg, and l_{leg} is the leg length. The total conduction loss is $2 \times G_{leg}$, because of two supporting legs from detector to the substrate. For the purpose of first-hand simple estimation of G_{leg}, assuming

$A_{leg} = 0.3\,\mu\text{m} \times 0.2\,\mu\text{m}$,

$l_{leg} = 34\,\mu\text{m}$ for an active microbolometer area of $(17\,\mu\text{m})^2$,

$\lambda_c = 19.2\,\text{W.m}^{-1}.\text{K}^{-1}$ using titanium nitride (TiN) as supporting leg material,

Equation (2.10) $\implies G_{leg} \approx 5 \times 10^{-8}\,\text{W.K}^{-1}$.

Nevertheless, it is rather evident from the first hand analysis that G_{leg} is usually order of magnitudes higher in value as compared to G_{rad} and dominates the thermal loss through the microbolometer. Thus, G_{rad} can be neglected which implies that $G_{th} \approx G_{leg}$.

2.4 Electrical-Thermal Behavior

To analyze the thermal behavior, we consider a detector representation in Figure 2.6 which consists of an absorber layer with the heat sensing material of thermal

heat capacitance C_{th} coupled via a low thermal conductance path G_{th} to a substrate acting as a heat sink at absolute temperature T_{sub}. Under no incident radiation, the temperature of the detector is same as that of substrate temperature. When exposed to the IR radiation, the thermal detector converts the incident radiant flux into the thermal energy and hence the detector temperature rises. The absorption efficiency is determined by an absorption coefficient of the detector material. The conversion of the resulting temperature variation into the resistance change is determined by the TCR of the detector.

Figure 2.7 represents an equivalent circuit representation of a microbolometer. As a matter of fact, the resistance R in microbolometer varies significantly with the ΔT due to absorbed IR radiation ηP_{in}, as well as, due to the undesirable bias heating effect termed as "Joule Heating ". Both of these source ηP_{in} and P_{joule} are added to the electrical circuit. In consequence to the Joule heating R decreases, which in turn further elevates the microbolometer temperature due to the power dissipation in the microbolometer. Thus, the higher bias current acts as a negative thermal feedback due to the negative TCR in a semiconductor-based microbolometer and deteriorates the detector operation. Nevertheless, this fact unfolds the closely inter-dependent thermal and electrical behavior of a microbolometer. The variable non-linear R of a microbolometer is represented by voltage-controlled current source (VCCS) under constant voltage bias V_b, where the current flowing through the microbolometer is proportional to V_b/R and R varies in proportion to ΔT and TCR. The series resistance R_s is included to account the contact resistance. The radiative and conductive thermal losses are included using their thermal equivalent values connected in parallel to the current source P_{in}.

2.4.1 Dynamic Behavior

The thermal behavior of a microbolometer can be analyzed using the heat balance equation (under no Joule heating) can be expressed as.

$$C_{th}\frac{d\Delta T}{dt} + G_{th}(\Delta T) = \eta P_{in} \tag{2.11}$$

P_{in} is the incident power in W.m^{-2}, η is the absorption coefficient of detector representing the amount of power absorbed in active area ($P_{absorbed}/P_{incident}$), and T_{bolo}

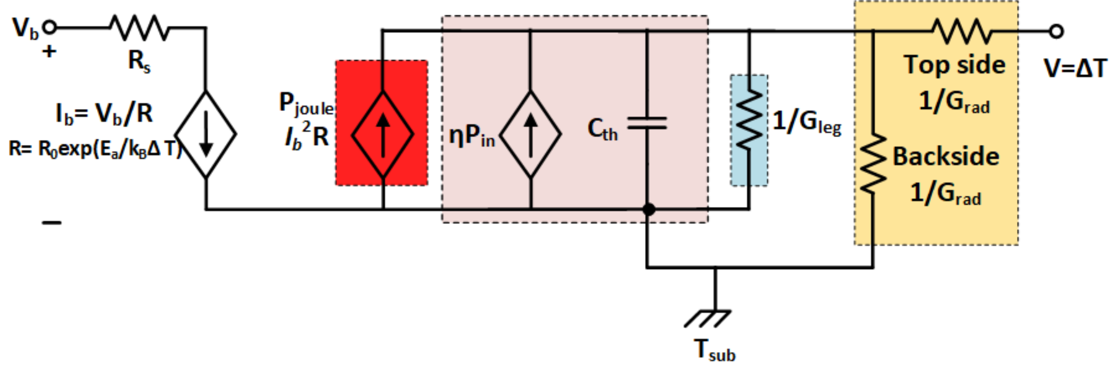

Figure 2.7: The equivalent circuit for a electrical-thermal model of a microbolometer, If $G_{leg} >> G_{rad}$, then G_{rad} can be ignored and $G_{th} \approx G_{leg}$ (adapted from [49]).

is the temperature of the microbolometer. The incident power is modulated such that P_{in}= $P_{in}\exp(j\omega t)$, where ω is the modulation frequency of incident IR power ($\omega = 2\pi f$) [31]. Equation (2.11) assumes no Joule bias heating, the solution of the equation is:

$$\Delta T = \frac{\eta P_{in}\exp(j\omega t)}{G_{th} + j\omega C_{th}} = \frac{\eta P_{in}}{G_{th}\sqrt{1+\omega^2\tau_{th}^2}} \tag{2.12}$$

τ_{th} is thermal time response time, expressed as

$$\tau_{th} = \frac{C_{th}}{G_{th}} \tag{2.13}$$

Equation (2.12) indicates that the temperature sensitivity (ΔT) of thermal detectors is proportional to the incident power, whereas, it varies in inverse proportion to the G_{th}. Therefore, it is desired to have ΔT as large as possible to enhance the detector response which implies that G_{th} must be very low. On the other hand, larger τ_{th} is manifested by the lower value of G_{th}, hence to reduce τ_{th} for faster response G_{th} should be larger. Both equations (2.12) and (2.13) illustrates one of the key design trade-off in terms of G_{th} for a resistive microbolometer.

Considering the simple circuit represented in Figure 2.8 with a battery of voltage V, a microbolometer of resistance R and a load resistor R_L, then the change is resistance ΔR due to ΔT can be expressed as:

$$\Delta R(T) = \alpha R_0 \Delta T = \frac{\eta\alpha f_F A_{bolo} R_0 P_{in}}{G_{th}\sqrt{1+\omega^2\tau_{th}^2}} \tag{2.14}$$

Ultimately, the change in voltage output ΔV (the signal voltage across R_L) caused by ΔT, under the bias current I_b is as follows:

$$\Delta V(T) = I_b \Delta R = \frac{\eta \alpha f_F A_{bolo} R_0 I_b P_{in}}{G_{th}\sqrt{1+\omega^2 \tau_{th}^2}} \tag{2.15}$$

where, A_{bolo} is the active microbolometer area and f_F is the fill factor which defines the percentage of the actual pixel area used for the IR collection.

When taking Joule heating into account, the heat balance equation (2.11) becomes:

$$C_{th}\frac{d\Delta T}{dt} + G_{th}(\Delta T) = P_{joule} + \eta P_{in} = \frac{d(I_b^2 R)}{dT}\Delta T + \eta P_{in} \tag{2.16}$$

where the first term on the right hand side can be expressed as

$$\frac{d(I_b^2 R)}{dT}\Delta T = \frac{d}{dT}\left(\frac{V^2 R}{(R+R_L)^2}\right)\Delta T = \left(\frac{V^2(R_L - R)}{(R+R_L)^3}\right)\frac{dR}{dT}\Delta T \tag{2.17}$$

V is the supply voltage, and R_L is the load resistance in series with the microbolometer. When (2.17) substituted into (2.16), then the equation is written as follows:

$$C_{th}\frac{d\Delta T}{dt} + G_{th,e}(\Delta T) = \eta P_{in} \tag{2.18}$$

$G_{th,e}$ is referred as effective thermal conductance and is defined as [31]:

$$G_{th,e} = G_{th} - G_{th,sub}(T_{JH} - T_{sub})\alpha\left(\frac{(R_L - R)}{R_L + R}\right) \tag{2.19}$$

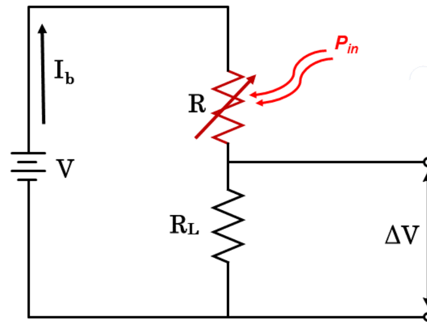

Figure 2.8: The electrical circuit representation of a microbolometer.

T_{JH} is the temperature increase in the microbolometer caused by the Joule heating. The steady-state solution of (2.18) becomes [31]:

$$\Delta T = \frac{\eta P_{in}}{G_{th,e}\sqrt{1+\omega^2\tau_{th,e}^2}} \tag{2.20}$$

where, the effective thermal time constant $\tau_{th,e}$ is

$$\tau_{th,e} = \frac{C_{th}}{G_{th,e}} \tag{2.21}$$

Similarly, (2.15) becomes

$$\Delta V(T) = \frac{\eta\alpha f_F A_{bolo} R_0 I_b P_{in}}{G_{th,e}\sqrt{1+\omega^2\tau_{th,e}^2}} \tag{2.22}$$

Equation (2.19) shows that the effective thermal conductance $G_{th,e}$ represents the difference in two terms. For the nominal device operation, $G_{th,e}$ must be positive i.e the second term must be less than the first term. If $G_{th,e}$ becomes negative (very low G_{th}), the microbolometer reaches burnout because of an exponential increase in the microbolometer temperature. As long as $G_{th,e}$ remains positive, the second term in (2.19) can be minimized by increasing the bias value (since the first term will remain same) to decrease $G_{th,e}$ which eventually enhances the voltage change as given in (2.22). On the other hand, $\tau_{th,e}$ will become large as $G_{th,e}$ decreases, which is undesirable in some applications.

2.4.2 Static Behavior

For unmodulated radiation i.e ($\omega = 0$), equation (2.12) can be written as

$$\Delta T = \frac{\eta f_F A_{bolo} P_{in}}{G_{th}} \tag{2.23}$$

f_F is the fill factor, η is the absorption efficiency and A_{bolo} is the active detector area. Thereby, when the microbolometer temperature increases by amount ΔT due to IR absorption, the corresponding change in resistance $\Delta R(T)$ can be expressed

in terms of TCR, as follows:

$$\Delta R(T) = \alpha R_0 \Delta T = \frac{\eta \alpha f_F A_{bolo} R_0 P_{in}}{G_{th}} \tag{2.24}$$

where α is the temperature coefficient of resistance. Finally, the change in the electrical resistance $\Delta R(T)$ caused by ΔT is measured by the voltage change (ΔV) across the detector. The voltage signal measured when biasing the microbolometer with a current I_b is

$$\Delta V(T) = \alpha R_0 I_b \Delta T = \frac{\eta \alpha f_F A_{bolo} R_0 I_b P_{in}}{G_{th}} \tag{2.25}$$

2.4.3 Microbolometer Temperature Resolution

The derivation and calculation presented here is adapted from the [50]. In order to estimate the change in microbolometer temperature when looking at the target at any temperature T_t with the background temperature T_B, the difference in the spectral exitance between the target and the background must be estimated within the spectral band 8 µm -14 µm.

$$\Delta M \simeq \Delta T_s \left(\frac{dM}{dT}\right)_{300\,\mathrm{K},\,8\,\mu\mathrm{m}-14\,\mu\mathrm{m}} \tag{2.26}$$

where the differential exitance change (dM) with respect to the differential temperature change (dT) can be calculated by taking the spectral integral of thermal derivative of Plank's law, as given in [51]

$$\left(\frac{dM}{dT}\right)_{300\,\mathrm{K},8\,\mu\mathrm{m}-14\,\mu\mathrm{m}} = 2.64 \times 10^{-4}\ [\mathrm{W.cm}^{-2}] \tag{2.27}$$

where the change is source temperature , $\Delta T_s = T_t - T_B$. Subsequently, the change in the radiant flux ($\Delta \Phi_s$) for a given change in ΔT_s is expressed as

$$\Delta \Phi_s = \frac{A_{bolo}}{4F_{\#}^2} \Delta M = \frac{A_{bolo} \Delta T_s}{4F_{\#}^2} \left(\frac{dM}{dT}\right)_{300\,\mathrm{K},\,8\,\mu\mathrm{m}-14\,\mu\mathrm{m}} \tag{2.28}$$

where $F_{\#}$ is the F-number of optics which is defined as the ratio of the focal length to the diameter of effective aperture of the camera lens. Thus, the resulting change

in the microbolometer temperature (ΔT_{bolo}) is calculated by combining (2.23) :

$$\Delta T_{bolo} = \frac{A_{bolo}\Delta T_s}{4G_{th}F_{\#}^2}\left(\frac{dM}{dT}\right)_{300\,\mathrm{K},\,8\,\mu\mathrm{m}-14\,\mu\mathrm{m}} \tag{2.29}$$

Assuming $F_{\#} = 1$, A_{bolo}= $17\,\mu\mathrm{m} \times 17\,\mu\mathrm{m}$

$G_{th} = 3 \times 10^{-8}\,\mathrm{WK}^{-1}$ *(as calculated previously in section 2.1.3)*

- If $\Delta T_s = 15\,\mathrm{K}$ (to see a target at $T_t = 310\,\mathrm{K}$ with background temperature $T_B = 295\,\mathrm{K}$), $\Delta\Phi_s \approx 2.8\,\mathrm{nW}$ and $\Delta T_{bolo} = 56\,\mathrm{mK}$.

- If $\Delta T_s = 50\,\mathrm{mK}$, $\Delta\Phi_s \approx 10\,\mathrm{pW}$ and $\Delta T_{bolo} = 200\,\mu\mathrm{K}$. Therefore, in order to develop a microbolometer with the specification of NETD of 50 mK, the microbolometer temperature resolution needs to be better than 200 µK.

2.4.4 Signal Readout

The resistive microbolometer can either be operated in constant current bias or constant voltage bias mode, depending upon the interface read-out design. The simplified readout circuit in a voltage bias configuration is shown in Figure 2.9 [52]. The circuit consists of an active microbolometer, a reference microbolometer and an integrator. The active microbolometer is the one exposed to the IR radiation, whereas, the reference microbolometer, generally referred as blind microbolometer, is optically isolated and thermally shorted to the substrate in order to provide fixed reference resistance. In the absence of IR, the current through the active microbolomter I_b and the current through the reference microbolomter I_{ref} are equal and there is no signal current I_{signal}. When the active microbolometer is exposed to IR, then the difference current due to the resistance variation ($I_{signal} = I_b - I_{ref}$) is integrated on integration capacitor by the help of an operational amplifier at a rate proportional to the magnitude of current. At the end of integration period, the voltage on V_{OUT} node represents the change in microbolometer resistance.

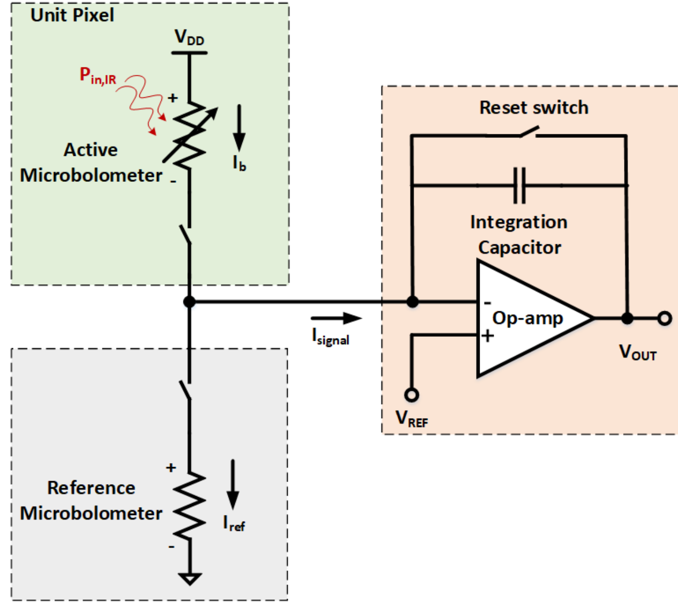

Figure 2.9: Simplified schematic of a unit pixel readout circuit for a microbolometer.

2.4.5 DC Responsivity

DC voltage responsivity ($\Re_v$) of a microbolometer measured in V/W, is defined as the ratio of output voltage change ΔV to the incident radiation power

$$\Re_v = \frac{\Delta V}{P_{in} A_{bolo}} = \frac{\eta \alpha f_F R_0 I_b}{G_{th}} \tag{2.30}$$

$\Re_v$ can be transformed into current responsivity ($\Re_i$) when microbolometer is operated in voltage bias mode [53] as given below:

$$\Re_i = \frac{\eta \alpha f_F V_b}{R_0 G_{th}} \tag{2.31}$$

DC responsivity of a microbolometer depends upon five important parameters as indicated by (2.30); i) TCR of the detector α, ii) absorption coefficient η, ii) fill-factor f_F, iv) thermal conductance G_{th}, v) applied bias V_b. At the present stage of technology, detector f_F ($> 92\,\%$) and η ($> 80\,\%$) are close enough to their ideal values, thus there is only limited room for improvement of these two parameters. Therefore, TCR and G_{th} are two primary parameters which can be improvised to enhance the microbolometer performance. A good thermal isolation (i.e low G_{th}) of microbolometer yields a higher responsivity. Higher TCR implies the larger change in the resistance of a microbolometer for a given change in the detector temperature.

2.5 Noise Sources

Noise is inherently present in any detection system due to random fluctuation of various elements in a system. There are four fundamental noise sources in a microbolometer, namely, Johnson noise, flicker noise, thermal fluctuation noise, and background fluctuation noise. The readout noise is not considered within the scope of this thesis. The total root mean square (RMS) noise voltage is the sum of the RMS noise voltages of all four sources, as these noise sources are the uncorrelated noise source [48]. The total noise measured as power spectral density (PSD, S_v) in V^2/Hz, depends upon the noise bandwidth, given as:

$$S_v = \frac{V_n^2}{BW} \tag{2.32}$$

V_n is the root mean-square (RMS) noise voltage and BW is the bandwidth. The noise bandwidth is the reciprocal to the integration time (τ_{int}) for the duration a bias pulse is applied i.e $BW = 1/2\tau_{int}$.

2.5.1 Johnson Noise

The thermal agitation of charge carriers causing random thermal motion of carriers in a resistive devices, under the external bias. This random fluctuation of charge gradients leads to the Johnson-Nyquist (thermal) noise. Increase in the temperature of microbolometer either due to IR absorption or self-heating will cause further increase in this noise. J.B Johnson had experimentally determined the thermal noise [54] in the resistor. The Johnson noise PSD in any resistor with the ambient resistance R_0 can be expressed as theoretically proven by Nyquist [55]

$$S_J = 4k_BTR_0 \tag{2.33}$$

The RMS voltage noise contribution by the Johnson noise (V_J) is expressed as

$$V_J^2 = 4k_BTR_0BW = \frac{2k_BTR_0}{\tau_{int}} \tag{2.34}$$

The Johnson noise is termed as "white noise" because of having uniform PSD across its entire spectrum. The Johnson noise can be reduced by cooling the detector as in

the case of photon detectors. On the other hand, for the uncooled detectors with a specific bandwidth the Johnson noise can only be reduced by decreasing the detector resistance, where the noise decreases proportional to the square root of R_0.

2.5.2 Flicker Noise

Another important noise source present in a microbolometer like in many physical systems is called flicker noise. The flicker noise component is primarily dominating in the lower frequency range and its spectral power per unit BW varies approximately as $1/f$. Thus, it is referred as $1/f$ noise or sometimes as the "pink noise". Beside frequency, it varies proportional to the applied bias across the detector, as it represents the slow fluctuations in the material resistance.

$1/f$ noise power spectral density ($S_{1/f}$) is approximated by [56]:

$$S_{1/f} = \frac{V_b^{\beta} k_{1/f}}{f^{\gamma}} \tag{2.35}$$

f is the frequency, γ is approximately close to 1 whereas β is close to 2, and $k_{1/f}$ is the flicker noise constant. $k_{1/f}$ is related to the Hooge's parameter α_H [57] and depends on the volume of the material. It is expressed as $k_{1/f} = \alpha_H/nV$, where n is the mobile charge carrier density and V is the volume of the resistor material. $k_{1/f}$ is considered as material-related noise parameter, strongly depending upon the resistor material type, the growth and deposition techniques, structural dimensions and electrical contacts. There is no straightforward analytical expression for RMS flicker noise, but experiments has indicated that its value is approximately expressed as [48] over the BW:

$$V_{1/f}^2 = \frac{V_b^2 k_{1/f}}{f} \tag{2.36}$$

Despite the fact $1/f$ noise dominates at lower frequencies, but at higher frequencies it falls below Johnson noise and this cross-over point is termed as the "knee frequency or the corner frequency". The knee frequency is determined by observing the overall noise, the frequency at which the Johnson noise becomes equal to $1/f$ noise in a 1-Hz interval [48]

$$4k_B T R_0 = \frac{V_b^2 k_{1/f}}{f_{knee}} \implies f_{knee} = \frac{V_b^2 k_{1/f}}{4k_B T R_0} \tag{2.37}$$

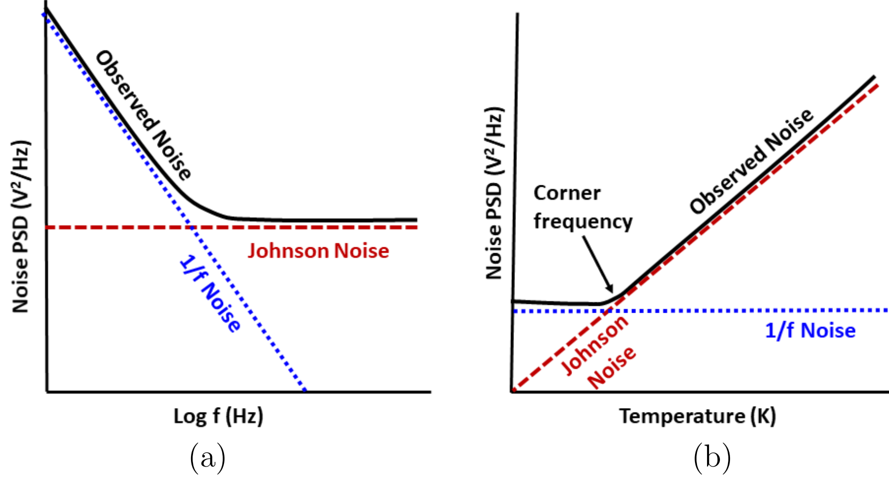

Figure 2.10: The observed noise as the sum of two major noise components $1/f$ and the Johnson noise a) as function of frequency b) as function of temperature.

Typically, the larger FPAs are operated in the serial readout mode through biased pulse, hence the electronic BW is sufficiently larger which implies that the Johnson noise is much greater than $1/f$ noise over the operational BW [31].

2.5.3 Temperature Fluctuation Noise

In addition to major noise source, there is third source of noise due to temperature fluctuation. The heat transfer among various objects give rise to thermal fluctuation. The random fluctuation of energy due to either conduction or convection phenomena induces random fluctuation in the detector temperature, which consequently results into random fluctuation voltage noise. The brief derivation of the temperature fluctuation noise is adapted from [31]. The mean square energy fluctuations in a system with thermal capacity C_{th} is

$$\overline{\Delta E^2} = k_B T^2 C_{th} \tag{2.38}$$

The detector temperature change ΔT and its stored energy ΔE are related as

$$\Delta E = C_{th} \Delta T \tag{2.39}$$

Hence, mean square temperature fluctuation ($\overline{\Delta T_f^2}$)can be derived from (2.39) and combined with (2.38)

$$\overline{\Delta T_f^2} = \frac{\overline{\Delta E^2}}{C_{th}^2} = \frac{k_B T^2}{C_{th}} \tag{2.40}$$

Furthermore, $\overline{\Delta T_f^2}$ can also be derived from the solution of the heat balance equation (2.11), the solution can be expressed in terms of $\overline{\Delta T_f^2}$ as given below:

$$\overline{\Delta T_f^2} = \frac{\overline{\Delta P_{in}^2}}{G_{th}^2 + \omega^2 C_{th}^2} \tag{2.41}$$

Thermal fluctuation is also a white noise source, therefore, (2.41) is integrated over all frequencies ($0 \rightarrow \infty$) to account the whole frequency spectrum, which results

$$\overline{\Delta T_f^2} = \frac{\overline{\Delta P_{in}^2}}{4 G_{th} C_{th}} \tag{2.42}$$

Equating (2.40) and (2.42) to solve for mean square power ($\overline{\Delta P_{in}^2}$)

$$\overline{\Delta P_{in}^2} = 4 k_B T^2 G_{th} \tag{2.43}$$

Substituting (2.43) into (2.41) gives $\overline{\Delta T_f^2}$ can be written in the final form as:

$$\overline{\Delta T_f^2} = \frac{4 k_B T^2 BW}{G_{th}(1 + \omega^2 \tau_{th}^2)} \tag{2.44}$$

Then, the corresponding mean square voltage can be expressed using (2.15) as:

$$V_{TF}^2 = \frac{k_B (2\alpha R_0 I_B T)^2}{G_{th}(1 + \omega^2 \tau_{th}^2)} = \frac{4 k_B G_{th} T^2 \Re_v^2 BW}{\eta^2} \tag{2.45}$$

As it can be seen clearly from (2.45), the only way to minimize the temperature fluctuation noise is by improving the thermal isolation of the detector. In other words, reducing the thermal conductance (G_{the}) through the microbolometer legs improves noise performance related to thermal fluctuations.

2.5.4 Background Fluctuation Noise

Background fluctuation noise is due to heat exchange between the detector and surrounding due to the radiative heat loss. The RMS noise voltage due to background fluctuation can be obtained by the substituting G_{rad} from (2.9) in the place of G_{th} in (2.45). Assuming ($\eta = \varepsilon$), background fluctuation noise rewrite as:

$$V_{BF}^2 = \frac{16 k_B \sigma_B A_{bolo} T^5 \Re_v^2 BW}{\eta} \tag{2.46}$$

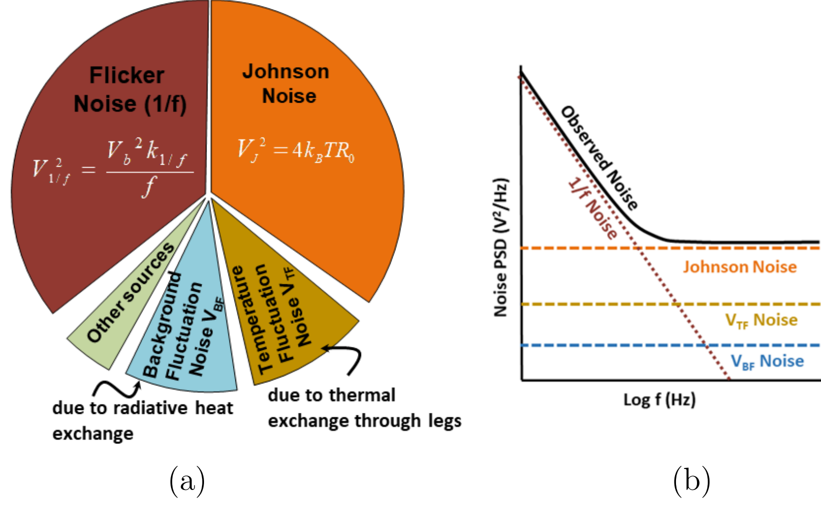

Figure 2.11: a) The contribution of the major noise sources to the total detector noise, b) The observed noise as the sum of all major noise components.

2.5.5 Total System Noise

The RMS noise voltage of system can be expressed by taking into account the noise contribution from all the four noise sources as shown in Figure 2.11.

$$V_N^2 = V_J^2 + V_{1/f}^2 + V_{TF}^2 + V_{BF}^2 \tag{2.47}$$

2.6 Detector Figure of Merits

2.6.1 Noise-Equivalent Power

The noise equivalent power (NEP) of a microbolometer is defined as the absorbed IR radiation in microbolometer producing the output signal (voltage or current) equivalent to the noise power. In other words, NEP can be be expressed as ratio of total noise voltage V_N to the responsivity of the detector.

$$NEP = \frac{V_N}{\Re_v} = \frac{\sqrt{V_J^2 + V_{1/f}^2 + V_{TF}^2 + V_{BF}^2}}{\Re_v} \tag{2.48}$$

2.6.2 Specific Detectivity

NEP is a convenient performance parameter for predicting minimum detectable power, however, it is not area-normalized. Detectors have different NEP based on the active area. Detectivity is a more generalized figure-of-merit. The reciprocal of

NEP normalized to the square root of detector area and BW is termed as specific detectivity D^* .

$$D^* = \frac{\sqrt{A_{bolo}BW}}{NEP} = \frac{\Re_v\sqrt{A_{bolo}BW}}{V_N} \tag{2.49}$$

For measurement one should take into account BW of microbolometer/readout, because the total noise can be reduced by reducing BW.

2.6.3 Noise Equivalent Temperature Difference

Noise Equivalent Temperature Difference (NETD) is the most relevant figure of merit for microbolometers in the thermal imaging applications. It is a measure for how well a thermal imaging detector is able to distinguish between very small differences in thermal radiation in the image. NETD is typically expressed in mK.

NETD can be calculated by estimating the spectral differential exitance (dM/dT) by unit area of a blackbody at certain temperature within the spectral band from λ_1 to λ_2. NETD is expressed as [31]:

$$NETD = \frac{4F_{\#}^2 V_N}{\tau_0 A_{bolo}\Re_v(dM/dT)_{T,\lambda_1-\lambda_2}} = NEP\frac{4F_{\#}^2}{\tau_0 A_{bolo}(dM/dT)_{T,\lambda_1-\lambda_2}} \tag{2.50}$$

τ_0 is the transmittance coefficient of optics, $F_{\#}$ is the F-number of the optics. NETD can be written as function of D^*

$$NETD = \frac{\sqrt{BW}4F_{\#}^2}{D^*\tau_0\sqrt{A_{bolo}}(dM/dT)_{T,\lambda_1-\lambda_2}} \tag{2.51}$$

2.6.4 State-of-the-Art Microbolometers

Vanadium oxide (VO_x) microbolometers are one of the most prominent semiconductors based microbolometers in the current market. Table 5 summarizes the state-of-art VO_x microbolometer performance specifications. a-Si is the second most commonly used microbolometer. Performance specifications of a-Si based microbolometer are listed in Table 6 .

Table 5: Performance specification of VO_x microbolometer from Raytheon [28]

Parameter	Value
Detector Type	Uncooled VO_x
Pixel Size	25 µm × 25 µm
Array Format	320 × 240
G_{th}*	35 - 75 nW/K
τ_{th}*	3 to 15 ms
Fill-Factor (f_F)	> 70 %
Spectral Response	8 - 14 µm
Frame Rate	60 Hz
Absorption	> 80 %
Responsivity (f/1)	$> 2.5 \times 10^7$ V/W or 20 mV/K scene
Resistance	20 - 200 kΩ
TCR	2.2 %/K
Output Noise	1.0 mV RMS
NETD @f/1, 30 Hz	< 30 mK
τ_{int}	25 µs
Power Dissipation	150 mW

*- Value of the variable depending upon design of pixel.

Table 6: Performance specification of a-Si microbolometer from ULIS [29]

Parameter	Value
Detector Type	Uncooled a-Si
Pixel Size	17 µm × 17 µm
Array Format	1024 × 768
Spectral Range	8 - 14 µm
τ_{th}	10 ms
Scene Dynamic Range	-20 °C - 80 °C
Frame Rate	50 Hz
Responsivity	12.1 mV/K
Fixed Pattern Noise	295 µV
NETD (f/1 @ 300K)	35 mK
Power Dissipation	60 mW

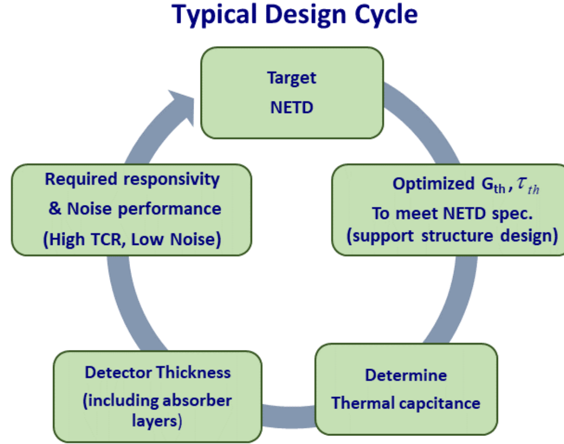

Figure 2.12: A typical design flow and procedure to optimize the performance specification of a microbolometer.

2.7 Design Constraints and Trades-off

A typical design cycle for a microbolometer is illustrated in Figure 2.12. For a desired NETD, the support structure is designed for required G_{th} and τ_{th}. Based on these specification, C_{th} and the total detector thickness is determined. Then, the detector performance specifications are optimized in terms of TCR, noise and the desired responsivity.

2.7.1 Pixel Pitch

Reducing the pixel pitch is particularly desirable for a LWIR camera to be in-line with the SWAP trend. There are two vital reasons associated with the smaller pixel size: First, the cost of expensive optical materials for lenses. Secondly, the spatial resolution to aid detection and identification range of the IR system. Germanium (Ge), zinc selenide (ZnSe), zinc sulfide (ZnS) are the materials majorly used for the optical lenses and coating. Reducing the pixel pitch decreases the lens diameter and thus cut downs the cost. The smaller pixels can be accompanied with larger format array to enhance the IR system resolution. The smaller pixel pitch poses a great deal of challenge to achieve high fill factor and low thermal conductance. The latest uncooled FPAs includes detectors with pixel pitch of 17 µm, 15 µm or even 12 µm.

2.7.2 Thermal Conductance and Capacitance

The current existing detectors mostly comprise the metallic or semiconductor sensing materials with the metallic legs or the stack of materials to support the suspended structure. The thermal loss from the detector is dominated by the conductive loss through the supporting legs, which is approximately 2 - 3 orders of magnitude higher than the radiative loss as shown in the section 2.1.3. The support materials yield the additional thermal conductance and capacitance overheads. The thermal conductance is a critical design parameter since the NETD varies proportional to it. The thermal conductive loss can be attenuated by the careful leg design parameters such as increasing the leg length, reducing the cross-sectional area or using the materials with lower thermal conductivity. Nevertheless, the lower thermal conductance must be accompanied simultaneously with the lower thermal capacitance in order to fulfill the thermal time constant constraint.

2.7.3 Thermal Absorption Efficiency

Typically, quarter-wavelength cavities are designed to enhance IR coupling efficiency to the detector. Current state-of-the-art microbolometer are equipped with absorption efficiency in the range of 80 % - 90 %. Hence, there is not enough room to play with the absorption efficiency.

2.7.4 Noise and Integration Time

Both $1/f$ noise and the Johnson noise components eminently contribute to the total noise of detector. As it is illustrated in (2.34), the Johnson noise depends on the integration time but $1/f$ noise is not affected as such with the integration time. Therefore if the noise is dominated by the Johnson noise, the total noise can be reduced significantly by the larger integration time or by increasing the bias voltage. On contrary, if $1/f$ is the dominant noise component then the larger integration time does not improve the overall noise performance. However, it should be noted that the integration time is constrained by the imaging frame rate (integration time= 1/frame rate divided into the total number of rows in FPA for a row-wise readout mode), thus for the higher frame rates the integration time can not take very large value. If both noise components are comparable, it is not advantageous to increase

either the integration time or the bias voltage.

2.7.5 High TCR and Low 1/f Noise Material

Both the DC responsivity given in (2.30) and NETD expression in (2.50) explicitly indicate that a material with the higher TCR would largely impact the overall performance of a detector. However, the higher TCR comes at the cost of larger resistance which inevitably increases the Johnson noise and $1/f$ noise. Therefore beside larger TCR, increasing either the bias voltage or the integration time to reduce the Johnson-dominated noise leads to the lower NETD value.

Commercially available microbolometers are either made of VO_x, a-Si or Si diode having TCR of $2-3\,\%K^{-1}$, $3.2-3.9\,\%K^{-1}$, and $0.2\,\%K^{-1}$, respectively as presented in Table. Both VO_x, and a-Si offers limited TCR and noise performance. Moreover, they are grown monolithically over the readout substrate which limits the processing flexibility too. The perpetual research in the recent years revealed a single crystal SiGe multi-quantum well (MQW) based device as a potential candidate for a microbolometer. SiGe is an attractive material choice to enhance TCR attributed to the amount of Ge content in the alloy, and lower $1/f$ noise due to its single crystal growth. Unlike VO_x and a-Si, the heterogeneous wafer-to-wafer integration is employed for bonding which offers the processing flexibility for the material system growth. The research in the domain of SiGe MQW has demonstrated 30 - 32 % Ge content [36], [37], [58], [59] in the epitaxially grown stacks, where 65 % Ge content is shown in stack grown by the inter-diffusion of Si and Ge-delta layer [38]. In the next chapter, we present the design and modeling of a single crystal $Si/Si_{1-x}Ge_x$ MQW with the Ge content varied from 30 % up to 50 %.

3 Chapter 3

Detector Design and Modeling

An understanding and description of the underlying material system is inevitable for the purpose of an investigation into the operation of $Si/Si_{1-x}Ge_x$ MQW device. The quantum mechanical interactions occurring between carriers and their surroundings in a crystalline solid fundamentally govern the macroscopically measurable characteristics of a detector. Computer simulations can be used to investigate the behavior of a device under realistic scenarios. Technology computer aided design (TCAD) modeling and simulation is used to predict the device performance which aids to expedite the device optimization and process development for new technologies and it provides remarkable physical insight into a real structure. Sentaurus TCAD platform provides integrated platform for comprehensive process and device simulation. In the first half of the chapter, electronic properties of Si, SiGe have been discussed to extract and calibrated the transport parameters through the device. Later half of the chapter describes a comprehensive physical device model and the self-consistent numerical implementation of the model in Sentaurus workbench (SWB) to investigate physical phenomena improvising the carrier dynamics and the predictive behavior of Si/SiGe MQW.

3.1 Material and Electronic Properties of SiGe Alloy

3.1.1 Crystal Structure

Both Silicon (Si) and Germanium (Ge) are group IV semiconductors and crystallize in the diamond lattice structure Figure 3.1. Si is the one of most abundant element in the earth's crust and having wide range of applications in commercial domains e.g building materials, glasses and ceramics, alloys and in electronics. Ge is much less abundant in nature but is very attractive material for a wide variety of applications like infrared optics [61], electronic chips [62] and solar electronics due to its outstanding electronic and photonic properties.

Chemically stable alloys of SiGe can be formed because of rigorous miscibility of Si and Ge over the entire compositional range. Nevertheless, the alloy preserves the

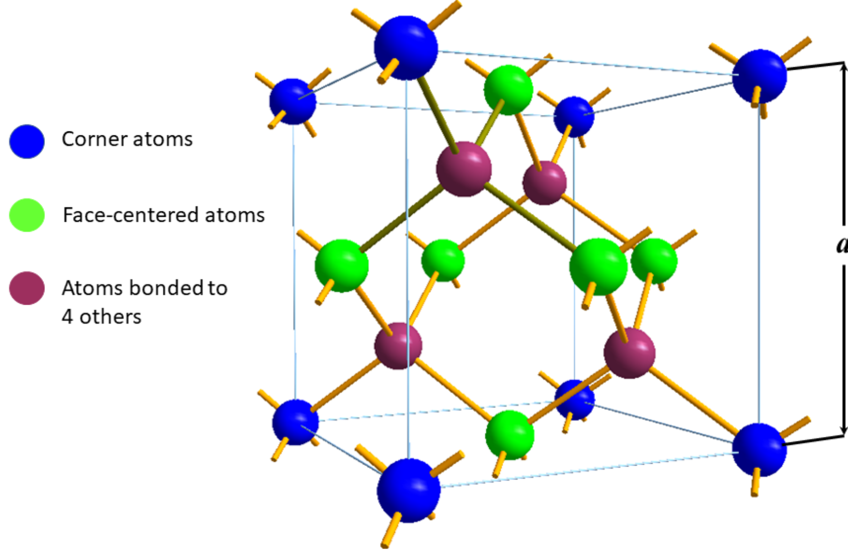

Figure 3.1: Unit cell of diamond lattice (adapted from [60]).

inherited diamond structure with a linearly interpolated lattice constant determined by Vegard's Law (3.1)

$$a(Si_{1-x}Ge_x) = a_{Si} + x(a_{Ge} - a_{Si}) \tag{3.1}$$

where a is the lattice constant and x is the Ge content (mole fraction) expressed in percentage. The lattice constant of pure Si and Ge are 5.431 Å and 5.658 Å respectively with a lattice mismatch of 4.17 % at a temperature of 300 K. The lattice constant of a $\mathrm{Si}_{1-x}\mathrm{Ge}_x$ increases with the increase of Ge content x [63]. During the "pseudomorphic" growth, the SiGe alloy is forced to adopt the lattice constant of the underlying Si substrate maintaining the in-plane crystal symmetry. The lattice constant of the alloy is compressed in the growth plane (shown in Figure 3.2) to match the substrate while it expands in the orthogonal direction distorting the crystal symmetry, in accordance to the Poisson ratio. Subsequently, the resultant strained energy is stored in the film and termed as "strained" SiGe film. Alternatively, the "relaxed" SiGe film can be grown without any compression where the lattice constant of the film is proportional to the natural lattice constant determined by the Si and Ge content [64]. In this case, the SiGe film relaxes due to misfit dislocations which causes defects in a crystal structure as presented in Figure 3.2.

The thickness of a strained SiGe film is limited by the amount of strained energy

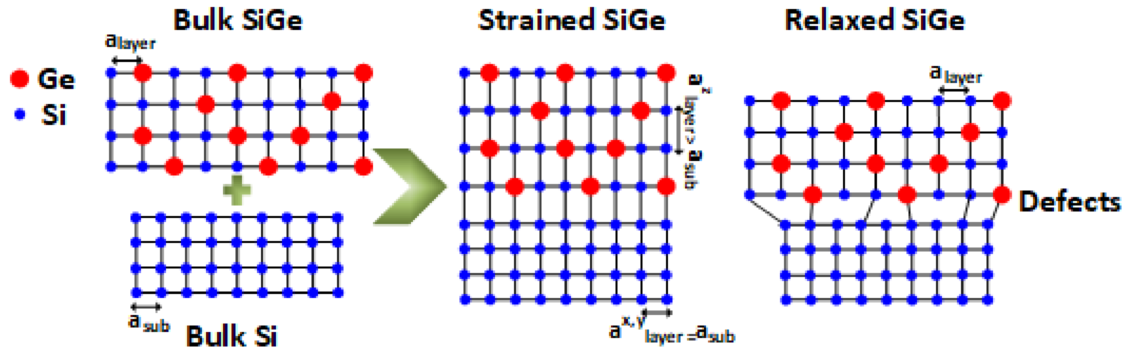

Figure 3.2: Schematic representation of both compressively strained and relaxed SiGe on a Si Substrate (adapted from [64]).

stored within the film. Above certain thickness, the strain energy becomes excessively large to retain the local balance. Subsequently, the SiGe film tends to relax by releasing the strain energy via incorporation of misfit dislocations. The maximum thickness until where a thermodynamically stable strained SiGe film can be epitaxially grown is referred as "critical thickness". The critical thickness sets the upper limit on the amount of Ge content that can be added to strained $Si_{1-x}Ge_x$. Typically, the critical thickness for a given amount of Ge content is estimated by well-known Mathews & Blakeslee [65] and People & Bean [66] theory. The critical thickness of a strained $Si_{1-x}Ge_x$ layer as a function of Ge content is presented in Figure 3.3.

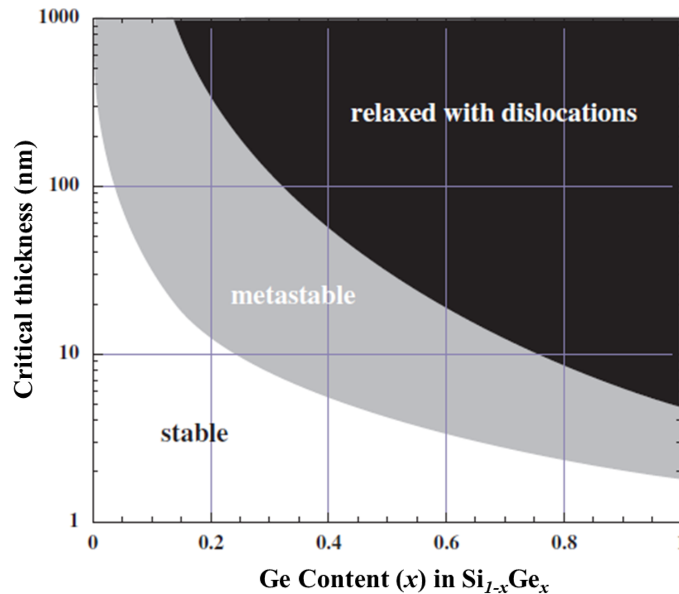

Figure 3.3: The critical thickness versus Ge content (x) for pseudomorphic $Si_{1-x}Ge_x$ layers grown on bulk (100) Si [64].

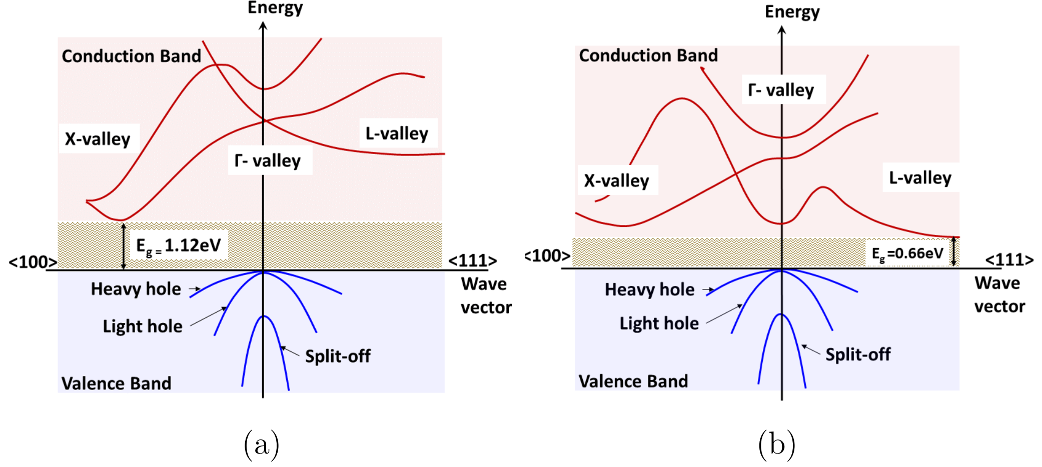

Figure 3.4: Energy band structure with degenerated conduction and valence bands (a) Si and (b)Ge [67].

3.1.2 Band Structure

The band structure of a semiconductor device plays a fundamental role in device modeling to determine the device characteristics. The energy and wave function of a carrier determines the state of a carrier and the overall band structure is estimated by the sum of these energies. The static and dynamic properties of carriers are mainly dependent on energy band structure.

Both Si and Ge have an indirect bandgap of 1.12 eV and 0.66 eV, respectively at 300 K. The valence band edge for both materials lie at $k = 0$ (Γ point) consisting of degenerate heavy-hole (HH) and light-hole (LH) with a split-off (SO) band lower in energy [64]. The terms "heavy" and "light" is used to differentiate the masses of the holes in each band relative to the other band of the unstrained case only. The main difference exists in conduction bands among Si and Ge. Si has the conduction band minima at the X-points whereas Ge has the conduction band minima at the L-points of Brillouin zone as shown in Figure 3.4.

The resultant $Si_{1-x}Ge_x$ alloy also exhibits indirect bandgap which varies with the added Ge content from the Si bandgap to the Ge bandgap. The resultant band structure of an unstrained $Si_{1-x}Ge_x$ alloy is Si-like for $x < 0.85$ with minima at the X-point and Ge-like for $x > 0.85$ with minima at the L-point due to abrupt changes in conduction band. The strain plays a critical role in altering the band structure of a strained $Si_{1-x}Ge_x$. The strain can be resolved into two components which mainly affects the band structure: the hydrostatic and the uniaxial strain. All the three

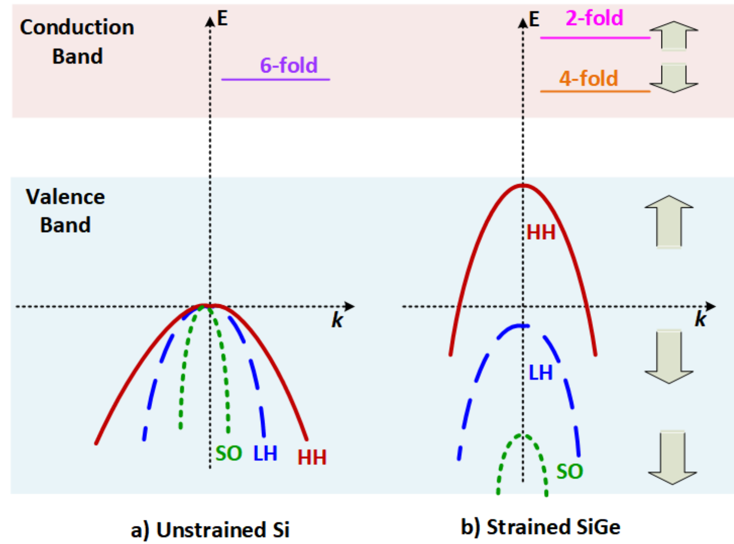

Figure 3.5: A schematic representation of the conduction and valence energy bands splitting of a compressively strained SiGe (b) in contrast to bulk Si (a).

valences bands (HH, LH and SO) are uniformly shifted under hydrostatic strain whereas uniaxial strain splits the degenerated HH and LH. Additionally, the strain lifts the six-fold conduction band degeneracy by lowering the 4-fold in-plane valleys below the 2-fold out-of-plane valleys, as represented in Figure 3.5. Despite of the strain, the shape of conduction band remains unaltered, but a substantial proportion of electrons are redistributed in 4-fold valleys which has lower out-of-plane mass. Thus, the electron mobility is direction-dependent and it increases in the out-of-plane direction. However, the shape of valence band is affected significantly due to reduction in the effective masses, therefore, enhances the hole mobility in both out-of-plane and in-plane directions due to reduced inter-band scattering [68].

3.2 Detector Design

The detector design consists of a heterostructure formed by alternating intrinsic layers of $Si_{1-x}Ge_x$ and Si as shown in Figure 3.6-a. The intrinsic stack of $Si/Si_{1-x}Ge_x$, denoted by i-MQW where i refers to the intrinsic regions, is sandwiched between heavily boron doped p^+-Si for ohmic contacts yielding the active area of detector with desired p-i-p profile. The final band-edge alignment of $Si/Si_{1-x}Ge_x$ forms a Type-I quantum well [69] where both valence band offset (ΔE_V) and conduction band offset (ΔE_C) are positive. In other words, the conduction and valence band edges of SiGe are contained within the band edges of Si whereby the valence

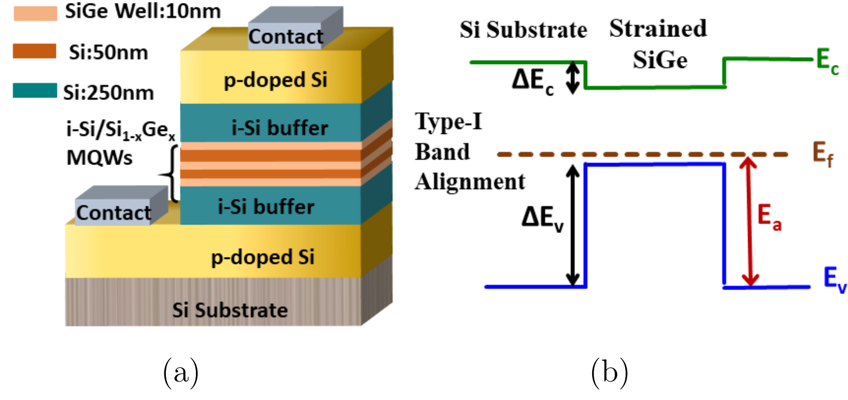

Figure 3.6: a) $Si/Si_{1-x}Ge_x$ stacked structure with Si buffers and p-doped Si layers b) The schematic representation of energy band alignment showing Type-I quantum well formation in SiGe layer.

band offset ΔE_V is quite large as compared to ΔE_C and creates a potential well for holes in $Si_{1-x}Ge_x$ layer as shown in Figure 3.6-b.

As discussed in the preceding section, the strain in an epitaxial $Si_{1-x}Ge_x$ alloy has a significant impact on the band structure by splitting the HH and LH in the valence band. The valence band offset (ΔE_V) increases as the amount of Ge (x) increases in $Si_{1-x}Ge_x$ manifested by the strain, without any appreciable change in the conduction band offset (ΔE_C) [70]. ΔE_V corresponds to the effective barrier height, thus the increasing the effective barrier height resulting more confined states and carriers within the $Si_{1-x}Ge_x$ well. The hole Fermi energy (E_f) lies near the top of valence band (shown in Figure 3.6-b) because of the heavy boron doping in the contact layers and the exact position of E_f depends upon the underneath p-doping levels. It lies deep into the valence band as the p-doping increases in the device and consequently the effective barrier height will decrease. Therefore, the precise and well-controlled doping in the device is essential to maintain the effective barrier height. A larger ΔE_V is particularly desirable as it corresponds to a higher activation energy (E_a) and thus the higher TCR. The activation energy E_a for this device is defined as given below:

$$E_a = E_f - E_V \tag{3.2}$$

where E_V corresponds to the valence band edge of Si. E_a increases due to the larger band offset as a result of increase in the Ge content (x) in the $Si_{1-x}Ge_x$ well.

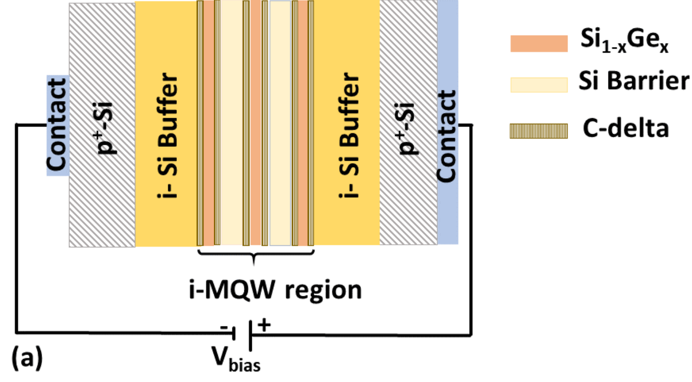

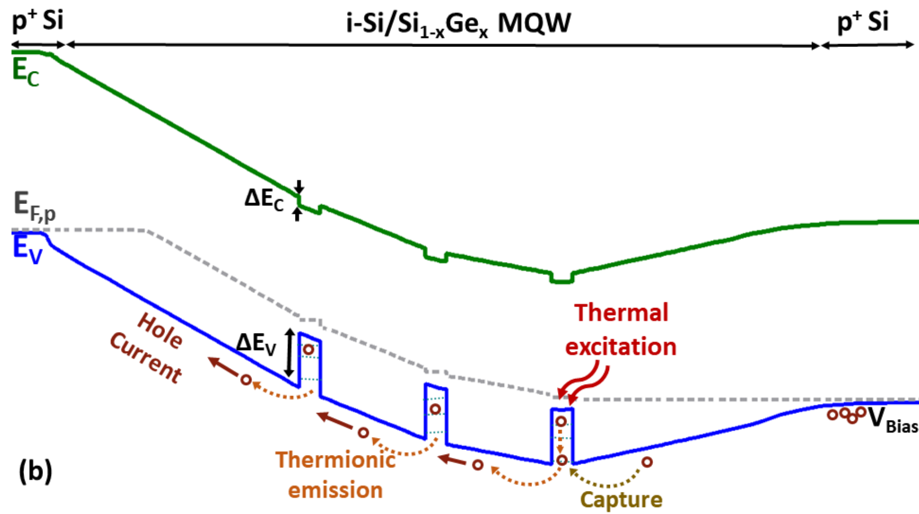

Figure 3.7: a) Cross sectional view of MQW structure b) Energy band diagram of device with three i-$Si_{1-x}Ge_x$ MQW under applied bias.

3.2.1 Effect of Carbon-delta Layers

It is essential to suppress the intermixing between Si and Ge at the heterointerface during the fabrication to obtain a high performance Si/$Si_{1-x}Ge_x$ heterodevice which requires an atomic-order abrupt heterojunction. Incorporating the carbon delta layers (C-delta) at Si/$Si_{1-x}Ge_x$ is not only effective to control its lattice strain and boron diffusion but significantly suppresses the Si and Ge mixing [71]. The results presented in [72] suggest that the presence of C atomic-layer at the heterointerface suppresses the strain relaxation as well as intermixing between Si and Ge especially in the case of higher Ge content in the thin film structures of nm-order thickness. Addition of C-delta layers at the heterointerface as shown in Figure 3.7-a,

confer a thermally stable, high quality and steeper Ge profile.

Considering both the band lineup at the interface as well as the strain effects, the estimation of the band offsets and the fundamental gap for $Si_{1-x}Ge_x$(C) alloys are presented in [73]. The investigations confirms that the carbon effect on the band structure is smaller than on the crystallographic structure and "Ge effects" (smaller band gap than Si and valence band offset to Si) dominates significantly in a completely strained-compensated ternary alloy.

3.2.2 Effect of Boron Autodoping

During the epitaxial growth at any instance, when a lightly doped region (i-Si buffer or i-MQW in our case) is exposed to a heavily doped region (p^+ Si) transport of dopant occur both through the solid and gaseous phases inadvertently. As a matter of fact during the high temperature epitaxial steps, the buried layer act as sources of unintentional doping. This phenomenon of unintentional doping is referred as background doping/autodoping which implies the impurity redistribution during the epitaxial growth. Autodoping is typically classified into two types: vertical and lateral. Vertical autodoping corresponds to dopant incorporation to the epitaxial layer grown over the heavily doped buried layer, whereas lateral autodoping refers to incorporation of dopant to the adjacent layers. Autodoping is rather complicated process and various process parameters intricate it further. Overall, autodoping process can be breakdown into the steps given below and illustrated in Figure 3.8 [74]:

(i) Solid-state diffusion of the impurities until surface

(ii) Evaporation from surface to the gas phase

(iii) Gas phase mass transport

(iv) Adsorption of impurities into the growing layer

Substrates are treated at high temperature during baking, which causes the out diffusion of the dopants present in the substrate. Subsequently, the composition of gas stream is modulated due to out diffusion and reintroduced into the epitaxial layer, thereby, changing the doping level in the epitaxial grown layers. Thus, the

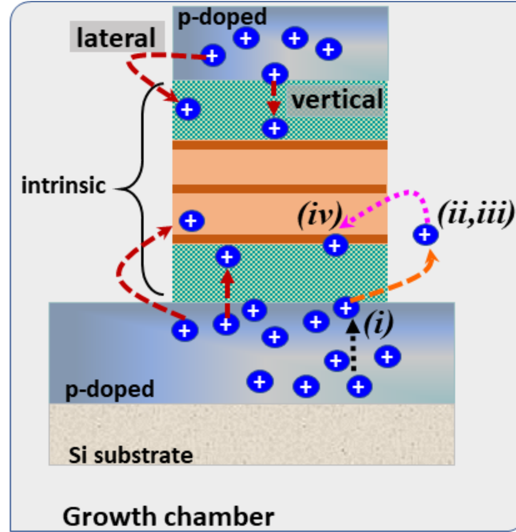

Figure 3.8: a) Cross sectional view of MQW structure b) Energy band diagram of device with three i-$Si_{1-x}Ge_x$ MQW under applied bias

high purity intrinsic buffer layers cannot be realized practically due to autodoping. Depending on process conditions, the autodoping can be as high as $1 \times 10^{17}\,\text{cm}^{-3}$. The physical device characteristics will be significantly affected due to autodoping. Inevitably, it is crucial to determine the doping profile of the structure for the device modeling perspective.

3.2.3 Current Transport

In the 2D MQW with the thickness or well width t, carriers are free to move in xy plane but confined in z direction, unlike 3D bulk materials where carriers are free to move in all directions. The adjacent barrier layers having adequate energy offsets to substantiate the carrier confinement in the lower energy states within the wells. The 3D continuum energy levels are quantized into discrete sub levels. The current transport mechanism in a Si/$Si_{1-x}Ge_x$ MQW involves the thermal emission of holes as a result of thermal agitation due to absorbed IR radiation. Under the thermal excitation, the holes leaves from the $Si_{1-x}Ge_x$ well to the valence band edge of the interface Si barrier. The holes are then transported in the direction of an applied electric field under the external bias voltage V_{Bias} as shown in Figure 3.7-b.

3.3 Physical Transport Parameters

The primary aim of device simulation is to analyze the physical processes in the interior of a device and to reliably predict the device behavior. The accuracy of the physical models and the calibrated transport parameters used in device simulation is very critical for reliable prediction of the device electrical characteristics. The carrier transport parameters such as the effective masses (m_n^*, m_p^*), the density of states (DOS), the carrier mobilities (μ_n, μ_p) and the carriers lifetimes (τ_n, τ_p) primarily depend upon the energy band structure. Moreover, the layer composition and strain also significantly influence these properties. As in strained SiGe, the energy band degeneracy and bands reshaping are significantly modified as a consequence of strain impact, therefore, all the transport parameters needs be carefully determined and calibrated as a function of the Ge content (x) in the alloy.

3.3.1 Electron and Hole Effective Masses

The effective masses are the key variables to dictate the density-of-states (DOS) and the mobility (μ_n, μ_p) which particularly effect the electrical characteristics of the device. The effective masses varies with the amount of Ge and the boron doping. However, the experimental values of effective masses are not available in literature, as it is rather cumbersome to determine the effective masses experimentally [63]. Nevertheless, there are extensive works to empirically investigate the effective masses empirically [75–77].

There are various types of effective masses associated with holes and electrons such as directional i.e. transverse (m_z), longitudinal (m_{xy}), density-of-states (m_d) and conductivity (m_c) effective masses. The shape of energy levels are described by the directional effective masses, essentially depicting the anisotropic transport properties. m_{xy} leads the flatter energy bands while m_z causes larger curvature energy bands. Furthermore, the directional effective masses (m_z, m_{xy}) are required for modeling DOS effective mass m_d^* and conductivity effective mass m_c^*. m_d^* is mainly required to model scattering mechanism whereas m_c^* is essential to model anisotropic mobility enhancement [76]. It has been shown that in case of the strained $Si_{1-x}Ge_x$ with Ge content from 0 to 0.5, m_z for an electron is approximated to $0.93m_0$ whereas m_{xy} is $0.19m_0$, same as that of the effective mass values in bulk

Table 7: Electron effective masses in bulk Si [78] and strained $Si_{1-x}Ge_x$ on (100) Si substrate [76, 79] at 300 K.

	Bulk Si	**Strained SiGe Ge Content <0.5**
Longitudinal mass (m_z)	$0.98m_0$[a]	$0.93m_0$
Transverse mass (m_{xy})	$0.19m_0$	$0.19m_0$
DOS mass (m_d^*)	$1.08m_0$	$0.83m_0$
Conductivity mass (m_c^*)	$0.26m_0$	$0.19m_0$

(a) m_0 is the rest mass of a free electron.

Si [76]. Thus, it can be concluded that directional effective masses of electrons are not significantly modified by strain, whereas m_c^* is orientation dependent and m_d^* decreases with increasing Ge content in strained $Si_{1-x}Ge_x$ which implies the electron mobility enhancement in the strained alloy.

The m_{xy} (in-plane mass) and m_z (out-of-plane) hole effective masses are calculated using $k.p$ band model and 6x6 Hamiltonians by Chun and Wang in [77]. In their work, the biaxial strain effect was treated same as the uniaxial stress since hydrostatic stress simply shifts all the energy levels in valence band uniformly without affecting the effective mass, taking into account the coupling to the conduction band. The strains effects on m_z and m_{xy} were investigated as function of Ge content for all hole masses components (HH, LH, SO). The directional dependences of effective masses are calculated from the energy curvature as follow:

$$\frac{1}{m_i} = \frac{1}{\hbar^2}\frac{\partial^2 E}{\partial k_i^2} \tag{3.3}$$

The index i denotes the direction of interest and $\hbar$ is the reduced Plank's constant. The results in [77] demonstrates that $m_{z,HH}$ remains unaltered, $m_{z,LH}$ increases and $m_{z,SO}$ decreases, respectively when compared to the unstrained case. The impact of strain on m_{xy} is opposite to that of m_z for LH and SO i.e $m_{xy,LH}$ decreases whereas $m_{xy,SO}$ increases, moreover, $m_{xy,HH}$ becomes smaller than that of $m_{xy,LH}$ when the strain induced splitting energy exceeds the coupling energy. Overall, all the hole effective masses decreases as the Ge content increases in the strained $Si_{1-x}Ge_x$ alloy, which has also been demonstrated experimentally through cyclotron resonance study of 2D holes in $Si_{1-x}Ge_x$ quantum well for various Ge con-

Table 8: The extracted longitudinal m_z and transverse m_{xy} effective masses of holes in strained $Si_{1-x}Ge_x$ on (100) Si substrate as function of Ge content [77].

Ge content (x)	Ladder	m_z	m_{xy}
0.3	HH	0.27	0.16
	LH	0.24	0.17
	SO	0.13	0.24
0.4	HH	0.26	0.15
	LH	0.23	0.16
	SO	0.12	0.23
0.5	HH	0.25	0.13
	LH	0.23	0.14
	SO	0.1	0.22

tents [80]. Unlike electron, m_c^* for holes are significantly reduced in $Si_{1-x}Ge_x$ [75]. Furthermore, m_d^* for holes shows strong dependency on the energy in the strained alloys [81]. Thus, the overall decrease in the hole effective masses enhances the hole mobility in the strained $Si_{1-x}Ge_x$ alloy.

3.3.2 Effective Density of States (DOS)

The density-of-states (DOS) is defined as number of available states in the respective energy level under the parabolic band assumption. To determine the carrier density in a device, foremost, the number of available states at each energy level has to be determined. The carrier concentration is then obtained by multiplying DOS with the probability that a state is occupied. The effective mass and DOS are closely related. Suppose, a flat energy band (having smaller slope) and a energy band with larger curvature/slope are considered, both with the same number of states along k-axis within the fixed energy interval. Then, a larger slope of energy band which essentially implies smaller effective mass, results less DOS as compared to the flat band (in consequence to the large effective masses) which results in higher DOS within the same energy interval as shown in Figure 3.9.

The effective DOS for Si in the conduction band (N_C) is modeled as a a function of the electron effective masses ($m_{d,e}^*$) [78]:

$$N_C = 2\left(\frac{2\pi m_{d,e}^* k_B T}{h^2}\right)^{3/2} \tag{3.4}$$

where k_B is the Boltzmann's constant, T is the absolute temperature and h is the Plank's constant. The temperature-dependent DOS in the conduction band can be computed as a function of the electron temperature (T_n) using DOS at the room temperature N_C(300K)

$$N_C(T_n) = N_C(300\,\mathrm{K}) \left(\frac{T_n}{300\,\mathrm{K}}\right)^{3/2} \tag{3.5}$$

Similarly, the effective DOS for Si in the valence band (N_V) is modeled as a function of the hole effective mass ($m^*_{d,h}$), [78]:

$$N_V = 2\left(\frac{2\pi m^*_{d,h} k_B T}{h^2}\right)^{3/2} \tag{3.6}$$

and the temperature-dependent DOS in the valence band is computed as a function of the hole temperature (T_p):

$$N_V(T_p) = N_V(300\,\mathrm{K}) \left(\frac{T_p}{300\,\mathrm{K}}\right)^{3/2} \tag{3.7}$$

3.3.3 Intrinsic Carrier Density

The temperature-dependent intrinsic carrier density (n_i) is determined by using (3.5) and (3.7) for undoped Si:

$$n_i(T) = \sqrt{N_C N_V}\exp\left(-\frac{E_g(T)}{2k_B T}\right) \tag{3.8}$$

For a heavily doped device as in our case, the carrier statistics are determined us-

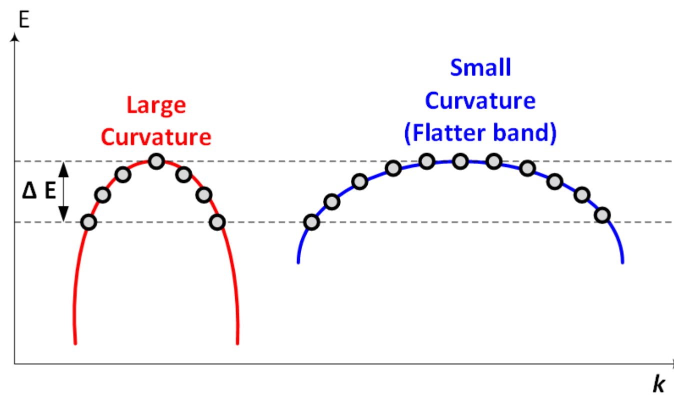

Figure 3.9: Valence energy band with larger and smaller curvatures shapes, illustrates the density-of-states difference among two bands in a fixed energy interval.

ing the effective intrinsic density ($n_{i,eff}$) corrected with doping-dependent bandgap narrowing (E_{bgn})

$$n_{i,eff}(T) = n_i \exp\left(-\frac{E_{bgn}}{2k_B T}\right) \tag{3.9}$$

3.3.4 Bandgap and Bandgap Narrowing (BGN)

The bandgap reduction dominantly occurs in the valence band due to Ge addition in SiGe alloy. The lattice temperature-dependent bandgap $E_g(T)$ of $Si_{1-x}Ge_x$ alloy is approximated as [82] and modeled as a function of Ge mole fraction:

$$E_g(T) = E_{g,T_0} - \frac{\alpha T^2}{T + \beta} \tag{3.10}$$

Here E_{g,T_0} represents the bandgap of bulk Si at zero kelvin which has value 1.17 eV. α and β are the material related parameters with values 4.73×10^{-4} eV/K and 636 K, respectively and T is the absolute lattice temperature. Additionally, the bandgap model is mole fraction dependent, the values of E_{g,T_0} for various Ge contents is interpolated between bandgap of Si and Ge using [70]. As the Ge content increases, the bandgap reduces in binary alloy whereas presence of few percent of carbon content in ternary allow lowers the bandgap narrowing as compared to the binary alloy for the same amount of Ge content. The effective bandgap ($E_{g,eff}$)in consequence to bandgap narrowing (E_{bgn}) is written as:

$$E_{g,eff}(T) = E_g(T) - E_{bgn} \tag{3.11}$$

Various types of the bandgap models are available in literature, Bennett-Wilson [83], Jain and Roulston [84], Slotboom [85] and del Alamo [86]. The difference between these various models essentially depends on how the bandgap narrowing (E_{bgn}) due to high impurity concentration is addressed in the model. Typically, Slotboom BGN model assuming Boltzmann statistics is valid for both n-type and p-type impurities with net impurity concentration (N_{tot}) above $\sim 10^{17}$ cm^{-3}, and described as (3.12):

$$E_{bgn} = A_{bgn}\left[ln\left(\frac{N_{tot}}{N_{ref}}\right) + \sqrt{\left(ln\left(\frac{N_{tot}}{N_{ref}}\right)\right)^2 + 0.5}\right] \quad (3.12)$$

As it can be seen from (3.12), the net apparent band gap narrowing is positive and increases with doping level. The corrected value of parameters in (3.12) for both n-type and p-type impurity concentration in Si employed in our model are $A_{bgn} = 6.92\times10^{-3}$ eV and $N_{ref} = 1.0\times10^{17}$ cm^{-3} [87].

3.3.5 Electron and Hole Mobility

Mobility is a critical transport parameter influencing the device characteristics. It relates the average drift velocity of carriers under the electric field drive. Mobility is directly associated with various scattering/collision mechanisms degrading the overall carrier mobility, namely:

- **Phonon / Lattice scattering** is caused by the interaction of lattice atoms and phonon, this interaction is strongly dependent on the temperature.
- **Impurity scattering** plays an important role in determining the behavior of devices due to the heavy impurity concentrations.
- **Carrier-Carrier scattering** causes significant mobility degradation.

Wide variety of well established and calibrated mobility models to cater phonon scattering [88,89], doping-dependent mobility degradation [90,91] and carrier-carrier scattering model [92, 93] are available in the commercial device design tool such as Sdevice in our case. Philips unified mobility model proposed by Klassen in [94], which not only addresses temperature dependence of the mobility but takes into account carrier scattering as well. Moreover, the high electric field effects must also be taken into account while determining the overall carrier mobility. Due to presence of high electric field, the carrier drift velocity saturates and does not remain proportional to the electric field. High-field saturation model by Canali [95] derived from [96] under various driving forces, is provided in Sdevice to retreat the high-field effects.

In Si/Si$_{1-x}Ge_x$ MQW model, the lattice temperature-dependent mobility model [88] together with the doping-dependent mobility model [90] are employed. Typ-

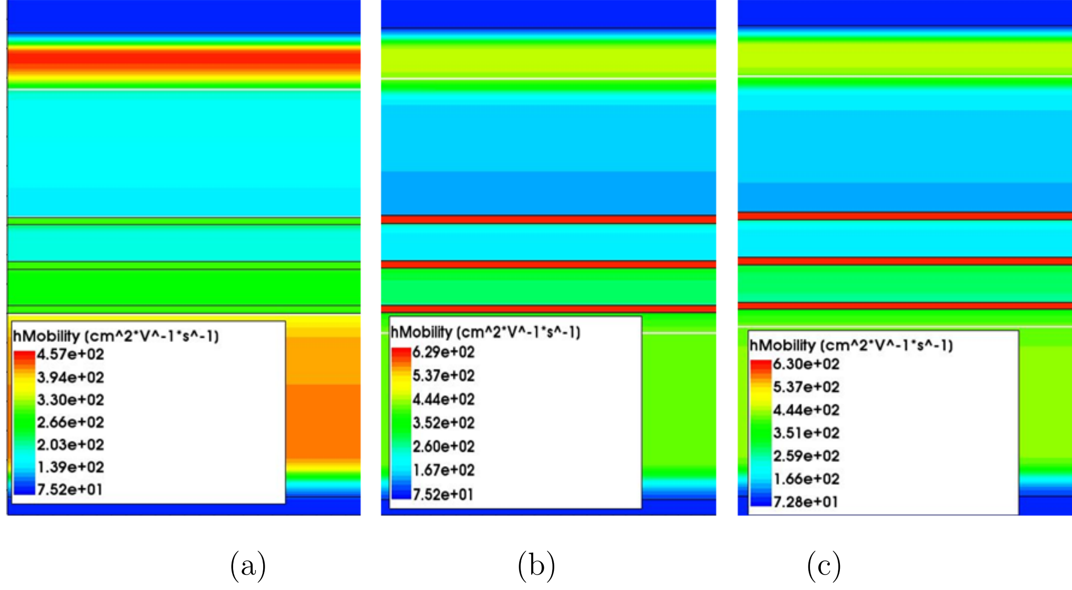

Figure 3.10: Hole mobility in Si/SiGe MQW at 300 K: a) Relaxed SiGe layers, b) Strained SiGe layers using mobility model from (3.13), c) strained SiGe layers using Philips mobility model.

ically, different mobility contributions are combined by Matthiessen's rule (3.13) which gives the overall low-field mobility(μ_{low}).

$$\frac{1}{\mu_{low}} = \frac{1}{\mu_{LS}} + \frac{1}{\mu_{IS}} + \frac{1}{\mu_{CS}} + ... \tag{3.13}$$

μ_{LS}, μ_{IS}, μ_{CS} are the mobility degradation components due to lattice scattering, impurity scattering and carrier-carrier scattering, respectively. Furthermore, μ_{low} is unified with the high-field saturation model [95] under the gradient of quasi-fermi potential ($\nabla\Phi_p$) as driving force to model the net carrier mobility (μ_{net}). The model parameters are calibrated as a function of mole-fraction (x) for the $Si_{1-x}Ge_x$ alloy.

$$\mu_{net} = f(\mu_{low}, \nabla\Phi_p) \tag{3.14}$$

On the other hand, Phillips unified mobility model [94] which unifies the temperature -dependent and the doping-dependent mobility degradation factors. Philips unified mobility model is equipped with the unique feature to model majority and minority and is recommended for HBTs and MOSFETs modeling [63]. The hole mobility in Si/SiGe MQW determined by either using Philips mobility model or by combing various scattering mechanisms mobility as stated in (3.13) gives nearly the same results as shown in Figure 3.10-b,c. Additionally, it is also obvious from Fig-

ure 3.10 that the mobility in the strained SiGe alloy is much higher in comparison to the relaxed SiGe alloy. The mobility enhancement in the strained SiGe alloy is attributed to the anisotropic hole masses as previously discussed in section 3.3.1.

3.3.6 Carrier Generation-Recombination Models

The physical processes related to mechanisms of generation and elimination of the mobile carriers are termed as Generation-Recombination process. Generation-recombination processes are particularly important in the semiconductor device physics. The process by which both carriers annihilate each other is termed as recombination process. The carrier generation is the process where electron-hole pairs are generated due to excited electrons. The Shockley-Read-Hall (SRH) recombination model and Auger recombination models are included in the carrier transport modeling.

A. SRH Recombination Model

The statistics of holes and electrons recombination through the traps/defects are described by the SRH recombination. The net trap-assisted recombination is given by [97]:

$$R_{net}^{SRH} = \frac{np - n_{i,eff}^2}{\tau_p(n + n_1) + \tau_n(p + p_1)} \tag{3.15}$$

where p and n are hole and electron densities, τ_p and τ_n are the hole and electron life times, respectively. The variables p_1 and n_1 are defined as:

$$p_1 = n_{i,eff} \exp\left(\frac{-E_{trap}}{k_B T}\right) \tag{3.16}$$

$$n_1 = n_{i,eff} \exp\left(\frac{E_{trap}}{k_B T}\right) \tag{3.17}$$

E_{trap} is the difference between the defect level and intrinsic level, with the default value of zero and can be specified in the input parameter file. The temperature dependence of the SRH lifetimes is modeled using power law [97] and the doping dependence of the SRH lifetimes is modeled with the Scharfetter relation [98].

B. Auger Recombination Model

Auger recombination is particularly significant in heavily doped regions of device

having higher carrier densities. The rate of band-to-band Auger recombination is given by:

$$R_{net}^{Auger} = \frac{C_n n + C_p p}{np + n_{i,eff}^2} \tag{3.18}$$

C_n and C_p are temperature-dependent Auger coefficients [98, 99].

3.4 Carrier Transport Modeling

The modeling approach in this work comprises the region-wise segregated device illustrated in Fig. 3.11 to treat explicitly the carrier's transport dynamics throughout the device. The device is segregated into three main regions:

(i) *Region* 1: Bulk Si

(ii) *Region* 2: $Si_{1-x}Ge_x$ MQW

(iii) *Region* 3: $Si/Si_{1-x}Ge_x$ Heterointerface

The carrier's distribution in *Region* 1: Bulk Si is approximated using Boltzmann's statistics. The confined holes distribution in *Region* 2: $Si_{1-x}Ge_x$ MQW is calculated by solving the Schrodinger equation. *Region* 3: heterointerface between Si and $Si_{1-x}Ge_x$ is approximated by the thermionic emission of holes through the $Si_{1-x}Ge_x$ well. The net current density is modeled by the self-consistent solution of the Poisson-Schrodinger solver coupled with the drift-diffusion transport formulation.

The electrical behavior of the device is described by Poisson's equation along with the current continuity equations and the current transport equations. The basic equations governing dynamics of the carriers in the device relates the fundamental variables electrostatic potential, carrier concentration and ionized dopant concentrations as follows:

A. *Poisson's Equation*

Poisson's Equation correlates the electrostatic potential ϕ to net charge density ρ. Poisson's equation is derived from first Maxwell's equation 1 based on the Gauss's law to describe electromagnetism (3.19):

$$\nabla . \overrightarrow{D} = \rho \tag{3.19}$$

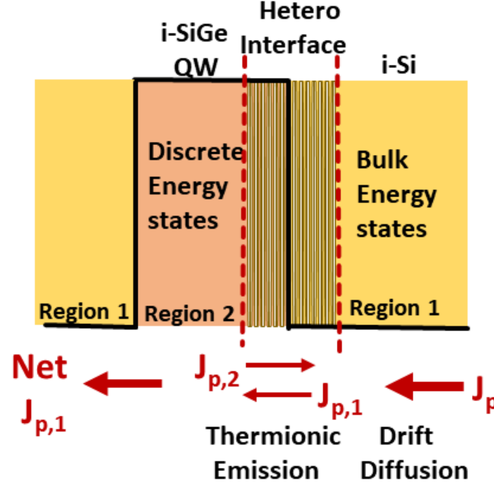

Figure 3.11: The regions-wise segregation of the device treated explicitly to model the carrier transport through the device

$\overrightarrow{D}$ stands for the electric displacement vector related to electric field $\overrightarrow{E}$ as $\overrightarrow{D} = \varepsilon.\overrightarrow{E}$, where ε is the electrical permittivity. Employing $\overrightarrow{E} = -\nabla\phi$ leads to Poisson's equation (3.20)

$$\nabla.(\nabla\phi) = -\frac{\rho}{\varepsilon} = -\frac{q}{\varepsilon}(p - n + N_D - N_A) \tag{3.20}$$

q is the electronic charge, n and p are the free electron and hole densities, N_A and N_D are the concentrations of ionized donors and acceptors, respectively.

B. Current Continuity Equation

The continuity equations (3.21) and (3.22) describe charge conservation and evolution of the carriers as a result of carrier generation and recombination processes to maintain a constant current along the device [78]:

$$\frac{\partial p}{\partial t} = -\frac{1}{q}\nabla.J_p + (G_p - R_p) \tag{3.21}$$

$$\frac{\partial n}{\partial t} = \frac{1}{q}\nabla.J_n + (G_n - R_n) \tag{3.22}$$

J_p, J_n are the hole and electron current densities, G_p and G_n are the hole and electron generation rates, R_p and R_n are the hole and electron recombination rates.

C. Drift-Diffusion Carrier Transport Model

The current densities are expressed in terms of gradient of quasi-Fermi potentials as follow [78]:

$$J_p = -q\mu_p p \nabla \Phi_p \tag{3.23}$$

$$J_n = -q\mu_n n \nabla \Phi_n \tag{3.24}$$

Φ_p and Φ_n are the hole and electron quasi-Fermi potentials, μ_p and μ_n are the hole and electron mobilities, respectively. Φ_p and Φ_n are related to the carrier densities, assuming the Boltzmann's approximation they are expressed as follows [78]:

$$p = N_V \exp\left(\frac{q(\phi - \Phi_p)}{k_B T}\right) \tag{3.25}$$

$$n = N_C \exp\left(\frac{q(\phi - \Phi_n)}{k_B T}\right) \tag{3.26}$$

N_V and N_C are the effective density-of-states, $E_{F,p} = -q\Phi_p$ and $E_{F,n} = -q\Phi_n$ are the qausi-Fermi energies for holes and electrons, respectively. k_B is Boltzmann's constant and T is the lattice temperature. By substituting Φ_p and Φ_n from (3.25) and (3.26) into the current densities expressions (3.23) and (3.24), J_p is written as follows [78]

$$J_p = -q\mu_p p \nabla \phi - qD_p \nabla p - \mu_p p k_B T \nabla ln N_V \tag{3.27}$$

$$J_n = -q\mu_n n \nabla \phi + qD_n \nabla n - \mu_n n k_B T \nabla ln N_C \tag{3.28}$$

The first terms in (3.27) and (3.28) refer to the drift components proportional to the electric field and second terms address contribution due to the carrier concentration gradient. The final terms including the gradient of effective densities, account for the bandgap narrowing effect. The diffusivity or diffusion coefficient D_p is given by Einstein relation (3.29) which relates the two critical parameters diffusivity and μ_p and μ_n to characterize carrier transport under drift and diffusion processes, as given below:

$$D_p = \frac{k_B T \mu_p}{q} \tag{3.29}$$

$$D_n = \frac{k_B T \mu_n}{q} \tag{3.30}$$

Total current density is J is calculated as a sum of both hole and electron currents, given as:

$$J = J_p + J_n \tag{3.31}$$

In our case p-i-p Si/Si$_{1-x}$Ge$_x$ MQW device, the majority holes constitute the primary carrier transport through the device, therefore, the current density concerns uniquely the holes in rest of the discussion. J_p in a conventional drift-diffusion formulation is written as [78]

$$J_p = -q\mu_p p \nabla \phi - q D_p \nabla p \tag{3.32}$$

D. Quantum-Confined Hole Density

1) *Localized Quantum-well Model*:

To model the quantum-well, the quantum-well quantization model in SDevice is employed for each local quantum-well. The 1D Schrodinger equation is solved iteratively using the Schrodinger parameters for an explicit hLadder ($m_{z,v}$, $m_{xy,v}$, d_v, ΔE_v) to define the properties of the various valence bands considering arbitrary strain and holes (HH, LH, SO). The vth specification for a carrier defines the quantization mass m_z, the mass perpendicular to the quantization direction m_{xy}, the ladder degeneracy d_v, and a nonnegative band edge shift ΔE_v. The hole density p within the Si/Si$_{1-x}$Ge$_x$ MQW is approximated by finding quantized Density-of-states (DOS), together with the local electric field F and local thickness t where p for each well is computed individually [82]. The solution of Schrodinger equation provides a quantized description of the DOS in the presence of quantum confining potential variations. Once the Eigen energies $E_{j,v}(F,t)$ and the wave functions of holes are calculated for all sub-bands of band v, then p for 1D confinement is determined using (3.33):

$$p = -\frac{k_B T}{t\hbar^2 \pi} \sum_v d_v m_{xy,v} \sum_j F_0 \left(\frac{E_{F,p} - E_V - E_{j,v}(F,t)}{k_B T} \right) \tag{3.33}$$

$E_{j,v}(F,t)$ are measured at the center of a wells with respect to the local band

edge E_V. $m_{xy,v}$ refers to the effective masses associated with all subbands, $\hbar$ is the reduced Plank's constant and F_0 is Fermi integral of zero order.

2) *Density Gradient Quantization Model*:

The lower-order quantum effects can be addressed by treating the state of carriers depending upon density-gradient (DG). DG is an extension of a classical approach to investigate the quantum confinement and quantum statistics effects, moreover, computationally it is quite advantageous [100]. The density modification can be represented by modeling a potential like quantity Λ_p for holes (3.34) using the Fermi integral $F_{1/2}$ in (3.35). Λ_p is given by the partial differential equation (3.34):

$$\Lambda_p = \frac{\gamma\hbar^2}{6m_p}\frac{\nabla^2\sqrt{p}}{\sqrt{p}} \tag{3.34}$$

γ is a fit factor depending on Ge mole fraction.

$$p = -N_V F_{1/2}\left(\frac{E_{F,p} - E_V - \Lambda_p}{k_B T}\right) \tag{3.35}$$

N_V is the effective density-of-states

E. Transport Across Heterointerface

Thermionic emission dominates the conduction mechanism over the tunneling phenomena at an abrupt heterointerface in the MQW attributed to the existence of the thick barriers [41]. The thermionic emission current is regarded as a boundary condition to relate quasi-Fermi levels on both sides of the heterointerface (Si/$Si_{1-x}Ge_x$), where the conventional drift-diffusion transport equations cease to be valid. Without considering heterointerface boundary condition, a numerical device solver does not solve current continuity equations across the interface but assumes continuous quasi-fermi levels across the interface which overestimates current through the device. The thermionic emission mechanism is important to be considered for accurate modeling, particularly in isotype (p-p, n-n) heterojunction with high barriers [41].

Given the valence band discontinuity such that $\chi_2 + E_{g,2} < \chi_1 + E_{g,1}$ where χ_i, and $E_{g,i}$ refers to the electron affinity and the bandgap associated with *Region*

1 and *Region* 2 as shown in Fig. 3.11. Considering $J_{p,2}$ is the hole current density leaving $Si_{1-x}Ge_x$ and $J_{p,1}$ is the net current density entering Si, the hole emission at the valence band discontinuity is formulated as (3.36)

$$J_{p,1} = -q\left(v_{p,1}T_{p,1}p_1 - \frac{m_{p,1}}{m_{p,2}}v_{p,2}T_{p,2}p_2 \exp\frac{\Delta E_V}{k_B T_{p,2}}\right) \tag{3.36}$$

p_i refers to the hole concentrations, $T_{p,i}$ refers to the hole temperatures, $m_{p,i}$ refers to the hole effective masses, $v_{p,i}$ refers to the emission velocities on both sides of the heterointerface. The emission velocity $v_{p,i}$ is defined as :

$$v_{p,i} = \sqrt{\frac{k_B T_{p,i}}{2\pi m_{p,i}}} \tag{3.37}$$

The initial lattice temperature is set to the input global temperature. Based on the specified thermal boundary condition, the average lattice and carrier temperature $T_{p,i}$ are determined by the simulation.

3.5 Numerical Simulation Framework and Methodology

The equations (3.20 - 3.36) related to the physical phenomena discussed in preceding section, form a complete system of the nonlinear partial differential equations which are solved self-consistently in the SWB taking into account the essential input files specifying the device geometry, the candidate doping profiles, the mesh definitions and the material related parameters. The fully integrated simulation frame work and methodology is described briefly in this section.

3.5.1 2-D Device Structure

Sentaurus Device Editor (SDE) facilitates to parameterize cross-sectional areas of device physical layers as well as the desired boron doping levels in the respective layers. 2D structure comprising three $Si_{1-x}Ge_x$ layers (MQW) of 10 nm thickness sandwiched between intrinsic Si barriers (i-Si) of thickness 50 nm, is constructed in SDE in batch mode by the script. The stacked structure is separated by the top and bottom intrinsic Si buffer layers of thickness 250 nm. Thickness of the Si buffer layers is optimized in order to reduce the auto/background doping in the

$Si/Si_{1-x}Ge_x$. Finally, heavily p-doped Si layers are used for the top and bottom contacts, as shown in Figure 3.12. The Ge content (x) is varied from 30 % up to 50 % in the $Si_{1-x}Ge_x$ MQW.

3.5.2 Generating Mesh and Doping Profile

The next step is to define the doping profiles and refinement parameters for the coordinates of the nodes at which the transport equations need to be discretized. A carefully specified mesh is essential to avoid any numerical convergence problems for the partial differential equations during discretization. A rectangular grid has been employed for meshing where the nodes are defined by the intersections of horizontal and vertical lines. Additionally, the mesh refinement is also performed in the regions having steep doping gradient, specifically near the Si/SiGe hetero-interface, as shown in Figure 3.13 to obtain the desired mesh density.

Similarly, a rectangular window has been used for placing the constant profile in the various device regions. Smoothing of the otherwise abrupt doping profile at the boundaries can be obtained by a parameter known as "Decay length" as illustrated in Figure 3.14. The doping profiles are smoothed using an error function with an inflection length specified by the decay length parameter. Figure 3.15 shows the highest doping level of $1{\times}10^{19}\,cm^{-3}$ in the Si regions to form the top and bottom ohmic contacts.

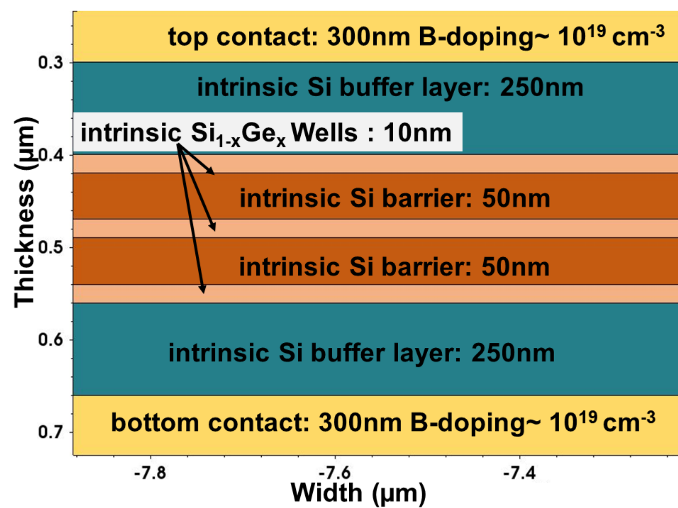

Figure 3.12: The 2D structure in SDE with three $Si_{1-x}Ge_x$ MQW with an active area of 17 µm × 17 µm

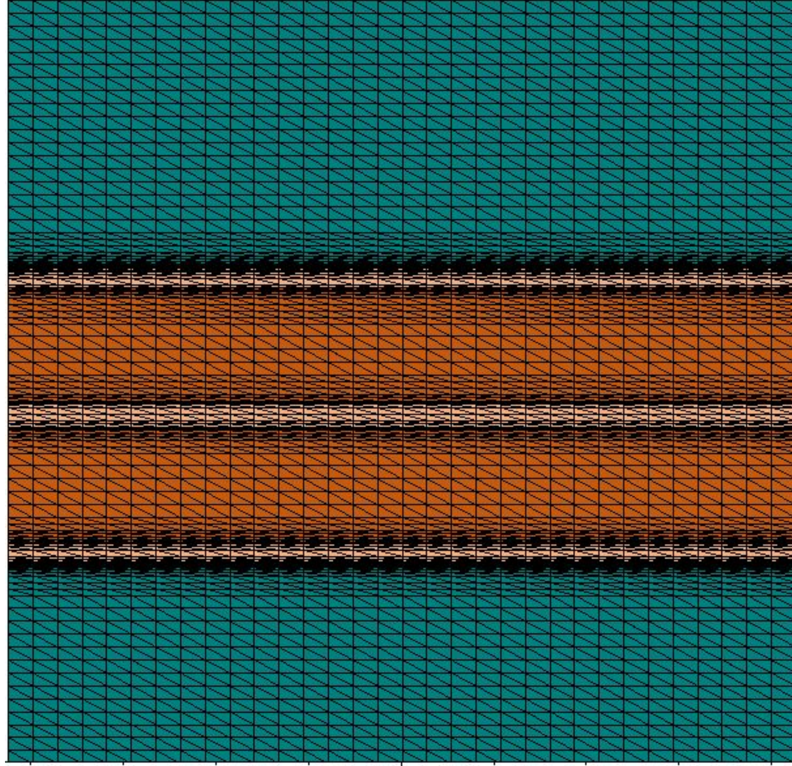

Figure 3.13: Discretization of simulation domain illustrating the rectangular meshing of the structure with the desired density and refinement near the Si/SiGe heterointerface.

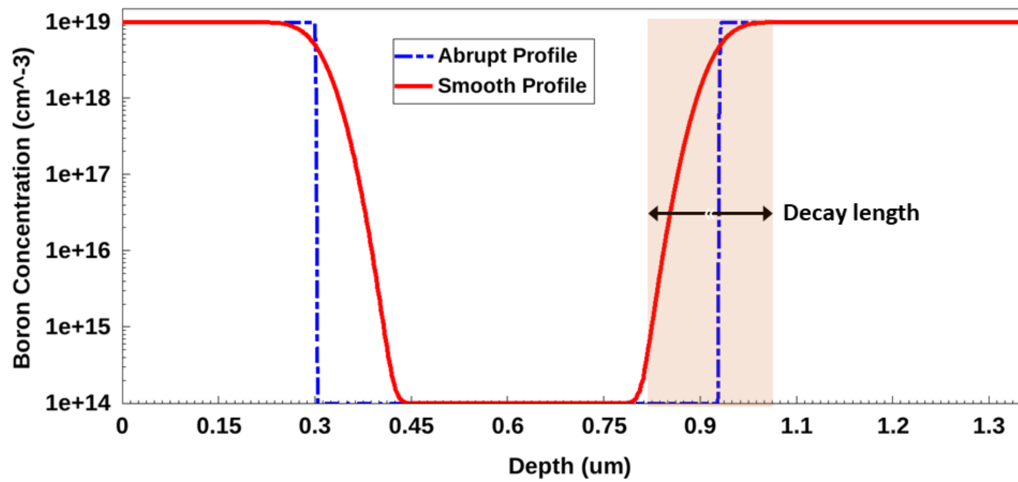

Figure 3.14: Abrupt doping profile versus smoothed edge profile obtained by defining the decay length parameter.

3.5.3 Boundary Conditions

A. Electrical Boundary Conditions

The fundamental transport equations are solved on a user defined bounded domain. The simulation domain is selected such that the boundary conditions are

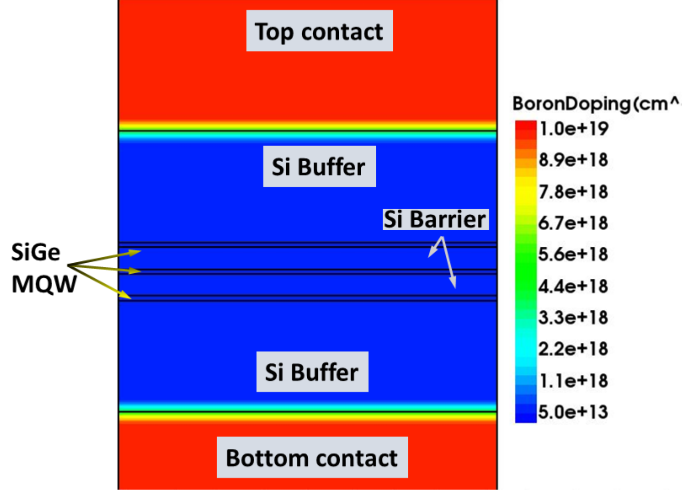

Figure 3.15: Initial boron doping profile placement in the 2D structure illustrating the heavily doped top and bottom Si regions for the ohmic contacts, nearly intrinsic Si buffer regions and Si/Si $_{1-x}$Ge$_x$ MQW stack.

well-satisfied to avoid inaccuracies and convergence problems during the numerical solution .The initial bias at the electrical contacts were defined as a voltage source with zero internal resistance to adjust the potential instantaneously during the simulation. Dirichlet boundary conditions [101] for the solution of the partial differential equations is assumed at the ohmic contacts including the generic ohmic contact conditions, such that:

(i) p and n are at their equilibrium values, determined by the charge neutrality conditions and designated as condition for Poisson's equation given as:

$$p + N_D = n + N_A \tag{3.38}$$

(ii) Holes and electrons quasi-Fermi potentials (Φ_p, Φ_n) are equal to the Fermi potential of the metal (Φ_M) being modulated by the external bias voltage V_{Bias}, yields conditions for the continuity equations:

$$\Phi_p = \Phi_n = \Phi_M \tag{3.39}$$

(iii) The hole and electron temperatures (T_p and T_n) are also at their equilibrium values, and equal to the lattice temperature T determined by the energy balance equation.

B. Thermal Boundary Conditions

Thermal boundary conditions are specified to determine the lattice temperature. At the thermal interface, non-homogeneous Neumann boundary conditions [101] are imposed as given below, via the thermal path having thermal resistance R_{th} (or thermal conductance)

$$\kappa\hat{n}.\nabla T = \frac{T_{ext} - T}{R_{th}} \tag{3.40}$$

κ is the thermal conductivity, $\hat{n}$ denotes the unit vector in the direction of outer normal, T_{ext} is the outer temperature, ∇T is the temperature gradient. In case of an ideal heat sink when $R_{th} \rightarrow 0$, Dirichlet boundary conditions are imposed.i.e. $T = T_{ext}$. The thermal resistance or thermal conductance values are specified for the thermal contacts as input in the thermal contact section in the Sdevice model by the parameter "*SurfaceResistance*" expressed in [$\mathrm{cm^2KW^{-1}}$]. We have specified R_{th} equivalent to G_{th} as calculated in section 2.3.3.

Lattice temperature describes the bias-dependent or current dependent self heating effect in the device. Global heat balance equations are employed to compute the global temperature where the total heat flux at the thermal boundary with finite resistance is equal to the dissipated power.

3.5.4 The Self-Consistent Solution Implementation

Typically, SDevice tool first discretizes the partial differential equations using box integration method [101] at user-defined nodes, then using the Bank and Rose scheme to iteratively solve nonlinear system by Newton method [102] subject to the appropriate boundary conditions. The numerical modeling methodology based on the region-wise segregated device illustrated in Figure 3.11 was implemented using two switch statements (*Quantization and Thermionic*) to investigate the effect of each physical phenomena detailed out previously in Section 3.4.

- *Case I: Baseline Solver*
  (Quantization=off, Thermionic=off)
  The baseline solver begins with the initialization as described in the flow chart in Figure 3.16, solving Poisson's equation only. Based on the initial bias at the contacts, it determines the initial values for ϕ, Φ_p, Φ_n, satisfying all the

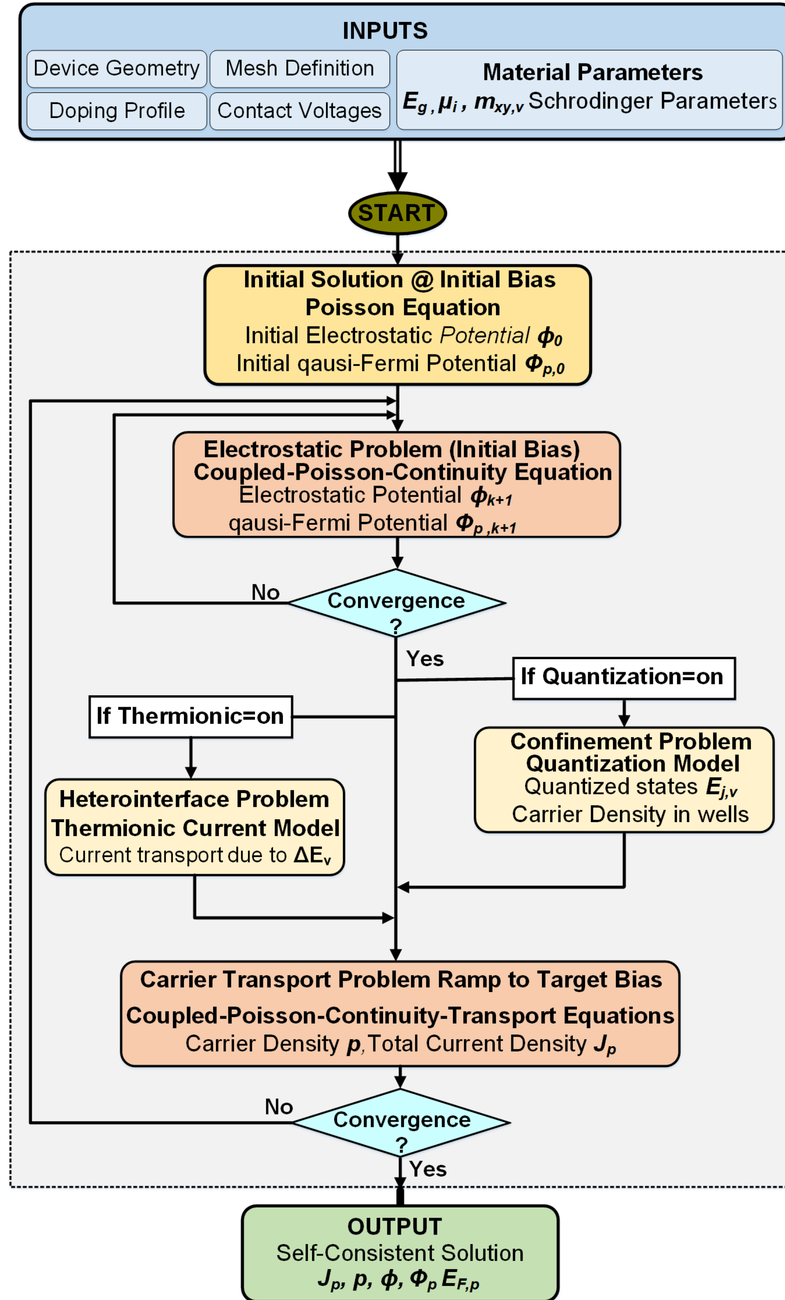

Figure 3.16: The flow chart of the self-consistent numerical framework and methodology implemented for the device simulation.

boundary conditions. In the second step, it solves the electrostatic problem by coupling Poisson-Continuity equations under initial bias condition. Finally, the solver proceeds to determine steady-state equilibrium solutions for each bias step iteratively. The energy band structure, ϕ, $E_{F,p}$, p are updated by the self-consistent coupled solution of Poisson-Continuity-Drift-Diffusion equations during each iteration. The solution is obtained for each bias step by taking the solution from the previous step as its initial guess and the loop ends

when the self-consistent convergent solution is obtained. The output dataset contains ϕ, Φ_p, $E_{F,p}$, p and J_p.

- *Case II: Coupled Baseline-Schrodinger Solver*
  (Quantization=on, Thermionic=off)
  The second scenario determines distinct Eigen Energies associated with the holes in the MQW regions by iteratively solving 1D Schrodinger equation which requires the explicit ladders specified for each valence band as well as the conduction band as given below:

$$hLadder(m_{z,v}, m_{xy,v}, d_v, \Delta E_v, HeavyHole)$$
$$hLadder(m_{z,v}, m_{xy,v}, d_v, \Delta E_v, LightHole)$$

  The v_{th} specification defines the quantization mass m_z, the mass perpendicular to the quantization direction m_{xy}, the ladder degeneracy d_v, and a band edge shift ΔE_v. The values of the effective masses of holes in the case of strained $Si/Si_{1-x}Ge_x$ alloy on relaxed Si(001) for various Ge content x are used as given in Table 8. When *Quantization=on*, p is computed by either (3.33) or (3.34) together with $E_{F,p}$ obtained from the coupled Poisson-continuity equations for each well. The estimated p is then resubstituted into the Baseline solver, the updated $E_{F,p}$ derived from next solution is substituted back into quantization model. These iterations continue until the convergence is reached. The output dataset includes number of bound states and quantized energy levels beside the outputs of the baseline solver.

- *Case III: Baseline Solver-Heterointerface boundary*
  (Quantization=off, Thermionic=on)
  Under this scenario, the quasi-Fermi levels on the both sides of heterointerface are self-consistently determined by the thermionic emission boundary condition assuming bulk energy states in MQW regions and no tunneling through the barriers. Instead of using (3.34), the thermionic emission expression (3.36) is used at the heterointerface to retreat the current transport across heterojunction between Si and $Si/Si_{1-x}Ge_x$ integrated with the Baseline solver.

- *Case IV: Fully coupled Baseline-Schrodinger-heterointerface*

(Quantization=on, Thermionic=on)

Finally, the quantization model in MQW regions alongwith the thermionic emission mechanism across the heterointerface are simultaneously integrated into the baseline solver to determine self-consistent convergent solution. This scenario taking into account the discrete energy states within $Si_{1-x}Ge_x$ MQW and the band discontinuity between Si and $Si_{1-x}Ge_x$ represents more realistic and accurate carrier transport dynamics through the device.

In general, this chapter has presented the self-contained comprehensive theoretical and numerical modeling framework for a $Si/Si_{1-x}Ge_x$ MQW structure. The physical phenomena governing the carrier transport together with the physical transport parameters related to the material and the device behavior have been explained. The simulation results obtained from the numerical model are thoroughly analyzed and compared with the experimental data in the next chapter.

4 Chapter 4

Predictive Model Simulation and Validation

This chapter includes the model simulation to investigate the effects of various physical design parameters (Ge content, well periodicity, well thickness). In particular, the effects of these physical design parameters on the carrier dynamics have been analyzed to determine Figure-of-merit specified in terms of temperature coefficient of resistance (TCR) and dc resistance (R). Moreover, the effect of various boron profiles and C-delta layers have been discussed on the overall device performance. The predictive behavioral modeling enables to optimize the design parameters to gear up for both high TCR and low noise. The dc characteristics obtained from the model are compared and validated with the experimental data obtained from the fabricated test devices at IHP microelectronics.

4.1 Device Fabrication

Fabrication of MQW device are carried out on a 8-inch Si wafer at IHP clean room facility [103]. The fabrication involves reduced pressure chemical vapor deposition (RPCVD) for the growth of Si/$Si_{1-x}Ge_x$ MQW. The fabrication process starts with cleaning the wafer. After loading to the CVD reactor the wafer is baked at 1000 ℃ to remove the native oxide. After temperature stabilization of the desired deposition temperature, first p-doped Si (bottom electrode) is deposited to obtain the bottom contact, followed by the deposition of thick Si buffer to refrain autodoping from the underneath heavily doped epitaxial layer. Thereafter, $Si_{1-x}Ge_x$ layers under the critical thickness constraint and the intrinsic Si barrier layers at 500 ℃ to 575 ℃ are deposited to form the MQW stack. Subsequently, the thick intrinsic Si buffer layer followed by the heavily p-doped layer as the top electrode are deposited. Additionally, the C-delta layers have been incorporated in the test devices to reduce the Ge diffusion, particularly in the case of higher Ge content [104].

Photo-lithography technique is used for patterning, followed by reactive ion etching (RIE) process to obtain desired active device area. The device with three different active areas (17 µm×17 µm, 25 µm×25 µm, 12 µm×12 µm) have been fabricated.

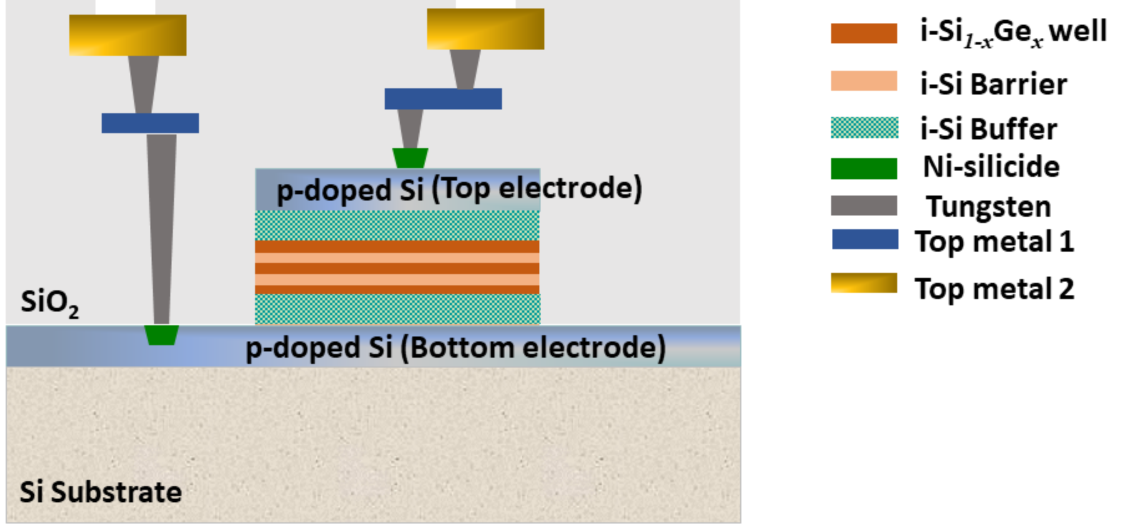

Figure 4.1: The schematic representation of fabricated device illustrating Ni silicide and double metal process for the contact pads.

Table 9: Device structure Specifications

Ge content (x)	0.3, 0.4, 0.5
Well thickness (nm)	10
i-Si barrier thickness (nm)	50
i-Si buffer thickness (nm)	250
p-doped Si thickness (nm)	500
p-doping (cm^{-3})	1×10^{19}
No. of well stacks	single, double, triple
Active area (μm^2)	25×25, 17×17, 12×12

Finally, the standard metal deposition is carried out to form the electrical contacts required for the dc probing as shown in Figure 4.1. Additionally, the nickel silicidation is also incorporated to reduce the interconnect resistance between the electrodes and the metal pads. The geometrical layer specifications are given in Table 9. The influence of C-delta layers at the interface between Si and Ge is investigated in detail in [104] and briefly discussed here.

High quality and steep Si/$Si_{1-x}Ge_x$/Si profile in the device specifically with 50 % Ge content, is obtained by introducing C-delta layers at the interfaces during the fabrication of MQW stack. Addition of C-delta layers reduces the surface roughness of $Si_{1-x}Ge_x$ and suppress the Ge diffusion, which essentially results in high crystallinity. The interdiffusion and migration at the Si/$Si_{1-x}Ge_x$ interface causes

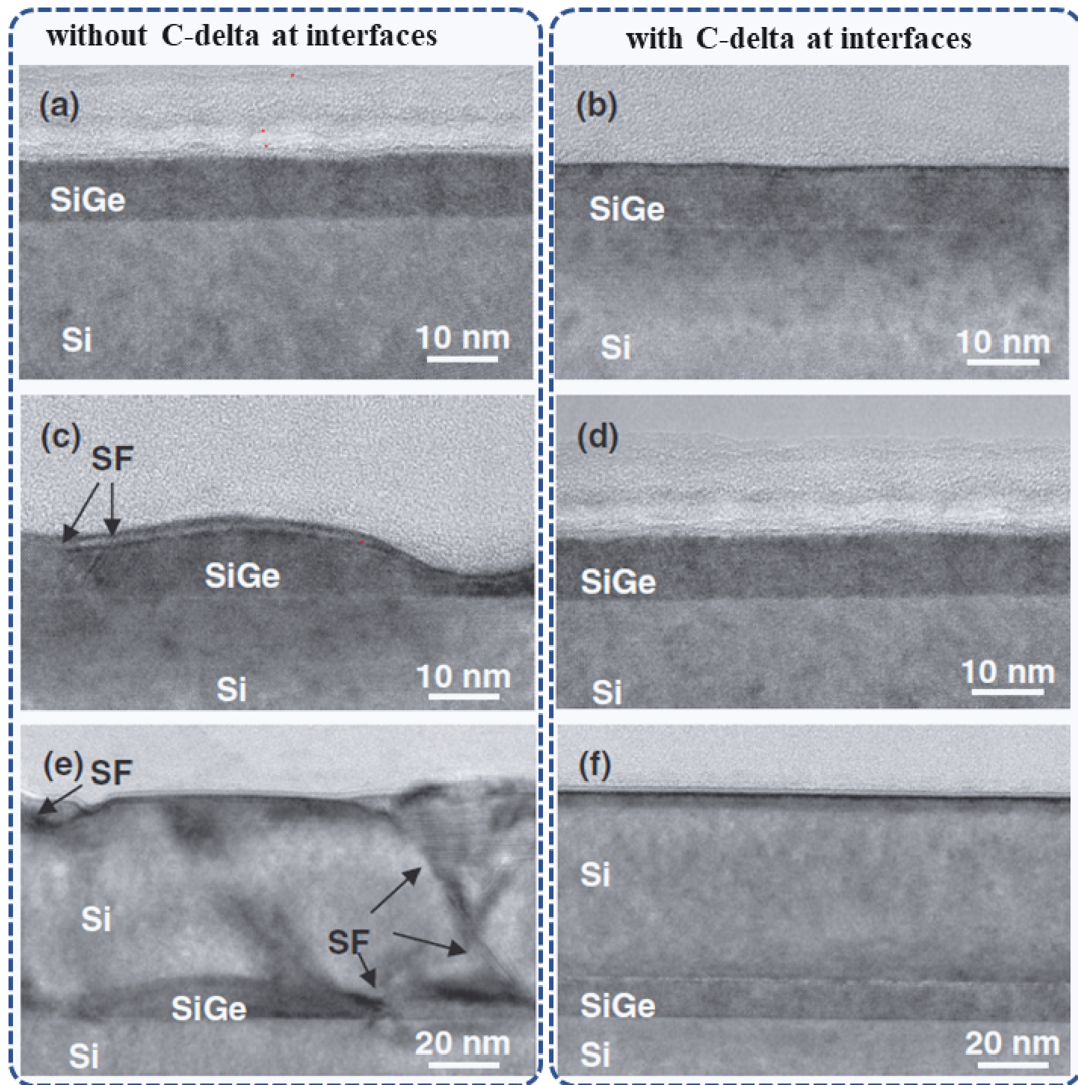

Figure 4.2: Cross sectional TEM images of $Si/Si_{0.5}Ge_{0.5}$ stack (a,b) show sample without post annealing. (c,d) show samples after post annealing at 575℃. (e,f) show Si cap growth at 575℃ [104].

smearing in the Ge profile. Figure 4.2 (a,b) shows smooth SiGe surfaces are observed for both samples after growth. Neither the stacking faults (SF) nor the misfit dislocations are observed which indicates the high quality crystal. During post annealing process, the samples without C-delta layers at the interface suffers severe surface roughness caused by surface migration of Si and Ge atoms, refer Figure 4.2-c. In contrary, no surface roughness is observed in the case of samples including C-delta layers at the interfaces, refer Figure 4.2-d. Likewise, deposition of Si cap on the sample without C-delta layer yields a defective Si with rough surface (see Figure 4.2-e), whereas smooth surfaces are obtained for the sample with C-delta layers at the interface shown in Figure 4.2-f.

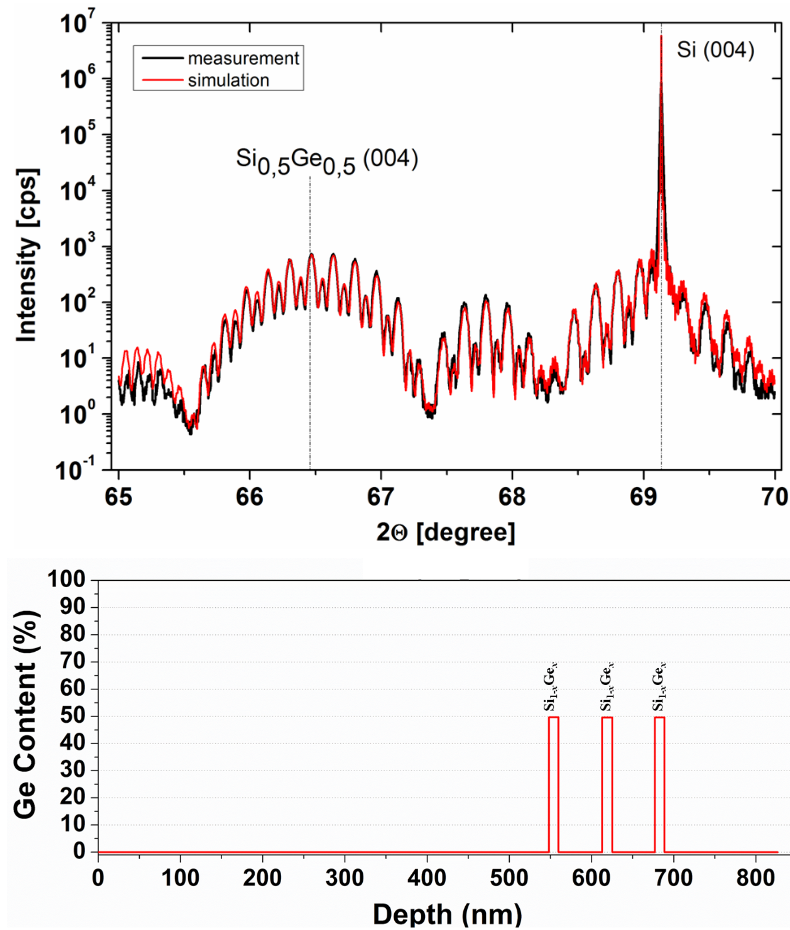

Figure 4.3: a) HR-XRD (004) measured (black line) and simulated (red line) rocking curve of (004) plane of the $Si/Si_{0.5}Ge_{0.5}$ MQW structure b) Simulated Ge depth profile for the $Si/Si_{0.5}Ge_{0.5}$ stack comprising three quantum wells [103].

4.2 Device Characterization

4.2.1 HR-XRD Measurement

In order to analyze the crystal structure of the epitaxially grown $Si/Si_{1-x}Ge_x$ MQW layers, high resolution x-ray diffraction (HR-XRD) measurements have been performed [103]. The profile of the structure are investigated through fitting the XRD rocking curve measurement to analyze layer thicknesses, crystal perfection, and Ge content in the $Si_{1-x}Ge_x$ MQW. Figure 4.3-a shows the XRD measurement performed on (004) planes of the $Si/Si_{0.5}Ge_{0.5}$ MQW structure. The diffraction pattern are in the close agreement in terms of peak position and peak intensity. The sharp oscillations of satellite peaks has been observed, which indicates the pseudomorphic growth of the stacked $Si/Si_{0.5}Ge_{0.5}$ layers exhibit high crystal quality whereas no relaxation is observed in the strained layers. The regular periodicity of

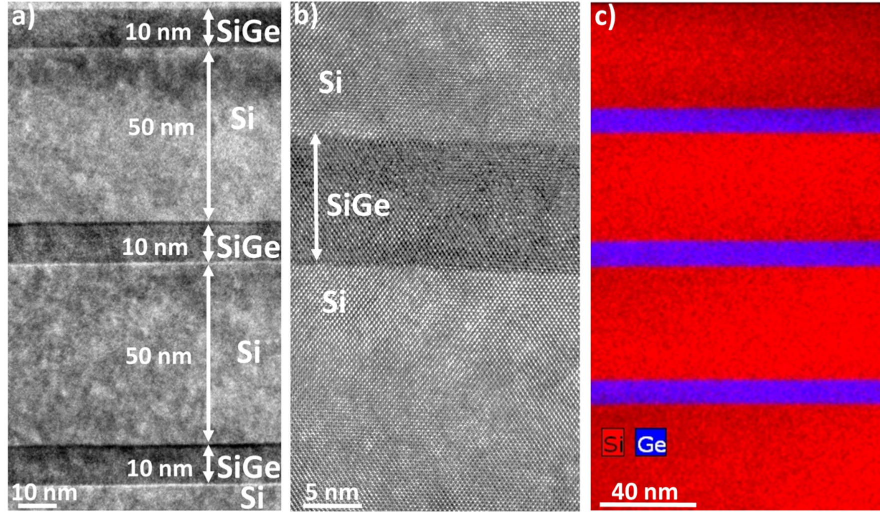

Figure 4.4: Cross-sectional TEM image: (a) three stack $Si/Si_{0.5}Ge_{0.5}$ MQW showing the uniform layer thickness, (b) the pseudomorphic growth of the fully-strained $Si/Si_{0.5}Ge_{0.5}$ with the smooth and even interface surfaces, (c) EDXS image showing the compositional analysis of $Si/Si_{0.5}Ge_{0.5}$ MQW [103].

the rocking curve illustrates the uniform thickness of each layer in the $Si/Si_{0.5}Ge_{0.5}$ stack and Si spacer layers as presented in Figure 4.3-b, showing the simulated Ge profile in the stacked structure.

4.2.2 TEM and EDXS Analysis

Transmission electron microscope (TEM) is used for the qualitative analysis of the $Si/Si_{1-x}Ge_x$ stacks and interface morphology. Figure 4.4-a shows the three $Si_{0.5}Ge_{0.5}$ 10 nm thick layers separated by 50 nm thick Si barrier layers. The zoomed TEM image in Figure 4.4-b illustrates the smooth and even interface surface between Si and $Si_{0.5}Ge_{0.5}$ layers which affirms the fully-strained and high crystallinity of the $Si_{0.5}Ge_{0.5}$, with no stacking faults and dislocations at the interface. The quantitative layer analysis of $Si/Si_{0.5}Ge_{0.5}$ is carried out using Energy-dispersive X-ray spectroscopy (EDXS). EDXS image in Figure 4.4-c conforms no intermixing and migration of Ge at the interface.

4.2.3 SIMS Analysis

To analyze the final boron profile in the test strcuture, time of flight secondary ion mass spectrometry (TOF-SIMS) measurements are carried out. A 2 keV O_2+ sputtering beam with a raster size of 300 µm × 300 µm has been used in combination

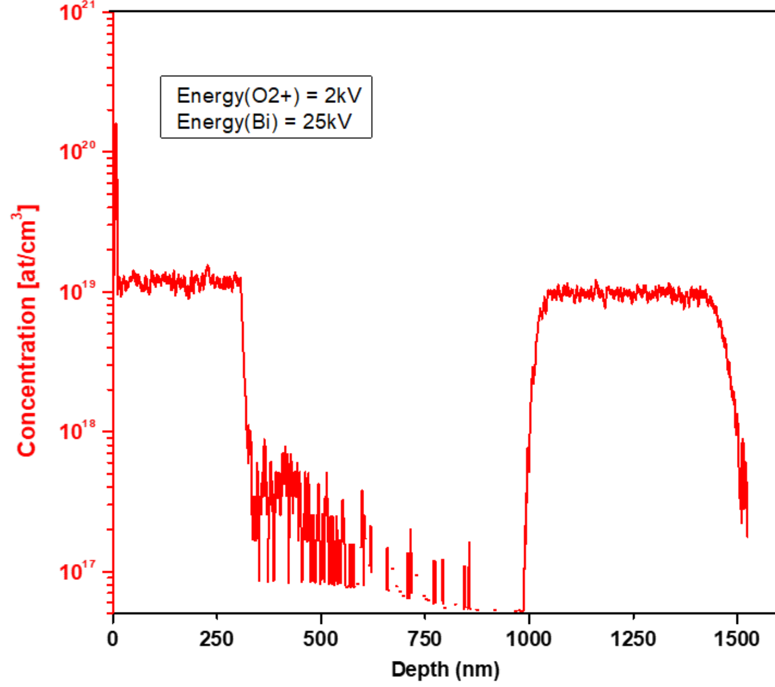

Figure 4.5: Measured SIMS profile of the test structure with triple $Si_{0.5}Ge_{0.5}$ shows the boron doping concentration in the various device regions.

with a bunched 25 keV Bi^+ primary ion beam with a raster size of 100 µm × 100 µm for the analysis. Figure 4.5 shows the doping profile in the Si/$Si_{0.5}Ge_{0.5}$ MQW structure, indicating heavily doped $1{\times}10^{19}$cm^{-3} in the top and bottom regions for the ohmic contacts. Moreover, the doping profile reveals the considerable asymmetric doping levels in the intrinsic top and bottom buffer regions and moderate doping in the Si/$Si_{0.5}Ge_{0.5}$ MQW because of autodoping/background doping mechanism as previously discussed in section 3.2.2. Consequently, the autodoping phenomena perturbs the electrical characteristics of the device particularly the linearity and symmetry over the bias range.

4.2.4 DC Transfer Characteristics Measurement

The test field shown in Figure 4.6 contains test devices with areas of 25×25 µm^2, 17×17 µm^2, 12×12 µm^2, comprising triple Si/$Si_{1-x}Ge_x$ stacks. The electrical transfer characteristics (I-V) of the fabricated test devices are measured with respect to various temperatures. The measurements were taken by heating up the device substrate placed on a temperature-controlled chuck over a temperature range of 278 K - 323 K with temperature step of 5 K. The measurement setup shown in Figure 4.7

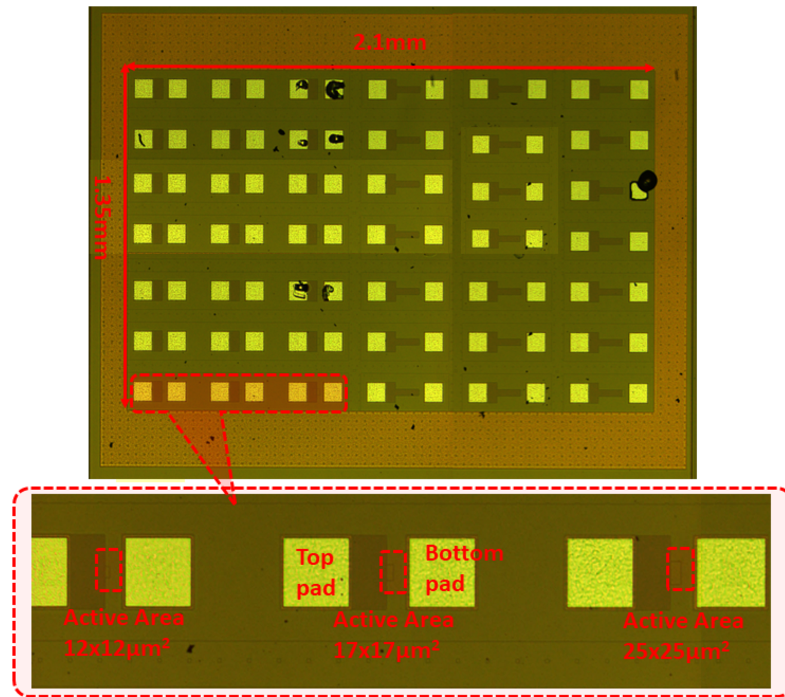

Figure 4.6: The test field with various test structures used for dc probing to extract I-V characteristics.

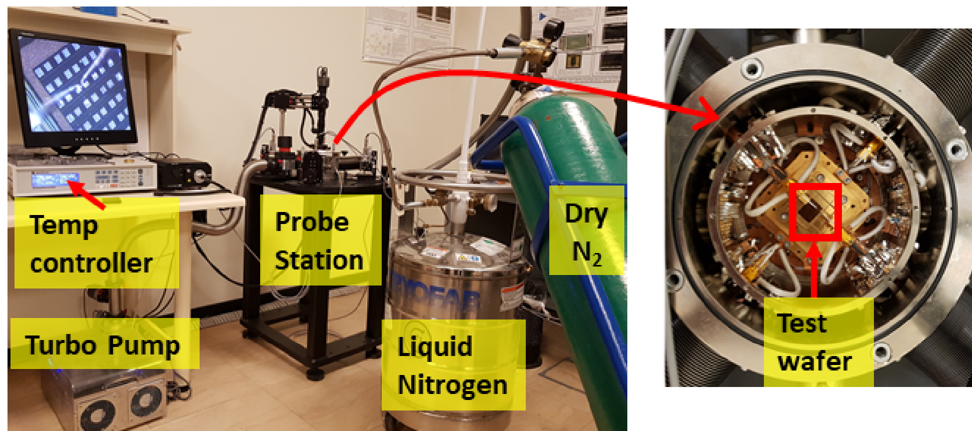

Figure 4.7: The on-wafer dc characteristics measurement setup.

contains liquid nitrogen dewar with dry nitrogen cylinder for the precise temperature step control. The temperature of the chuck is monitored closely through the temperature controller. For each Ge content, data was extracted from devices on 9 different locations over the two 8 - inch test wafers. The I-V measurement showed the consistency and well-uniformity in the data obtained from various text structures as shown in Figure 4.8.

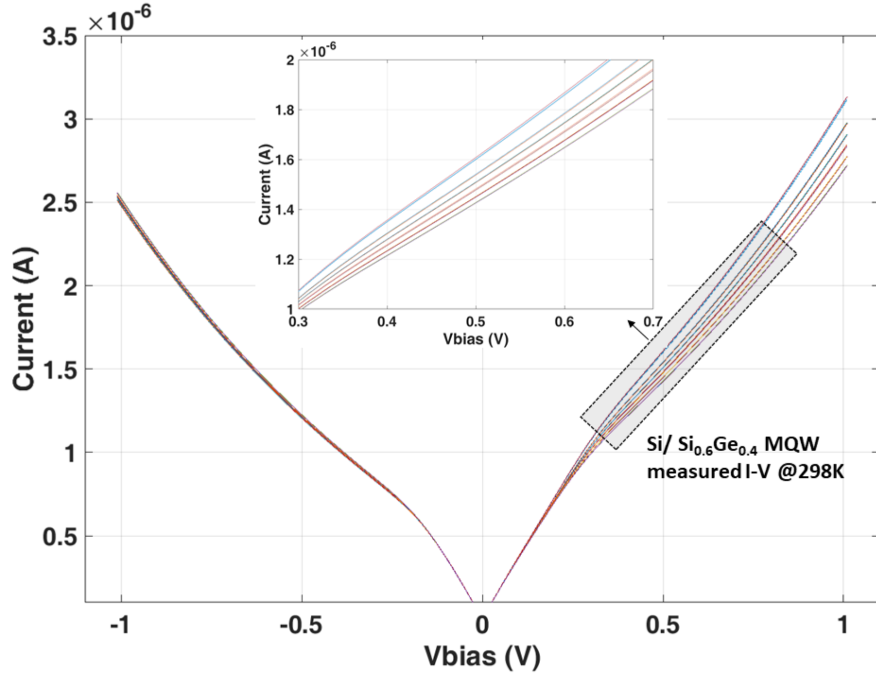

Figure 4.8: On-wafer dc measurement of eighteen test devices from two different wafers shows the measurement uniformity and the data consistency.

4.3 Predictive Simulation and Validation

Device simulation have been performed to investigate the dc characteristics (I-V) of Si/$Si_{1-x}Ge_x$ MQW detector for various Ge profiles, QW periodicity and device area to extract important Figure-of-Merits (FoM) of the detector expressed in terms of TCR and dc resistance R in the following subsections.[1]

4.3.1 Steady-State Carrier Transport

To investigate the physical mechanisms governing the hole transport through the device, the four cases were simulated individually as discussed in previous chapter. *Case I* (*Quantization=off, Thermionic=off*) comprises the baseline solver without considering quantum confinement and the heterointerface discontinuity assumes $E_{F,p}$ to be continuous across the interface, tends to overestimate the current density as shown in Fig. 4.9. *Case II* (*Quantization=on, Thermionic=off*), discretizes the energy states across heterointerface and performs hole density correction within the MQW regions leading to comparatively less current density as compared to *Case I*. Next, *Case III* (*Quantization=off, Thermionic= on*) improves model prediction

[1]this work is a part of a peer-reviewed journal publication [105]

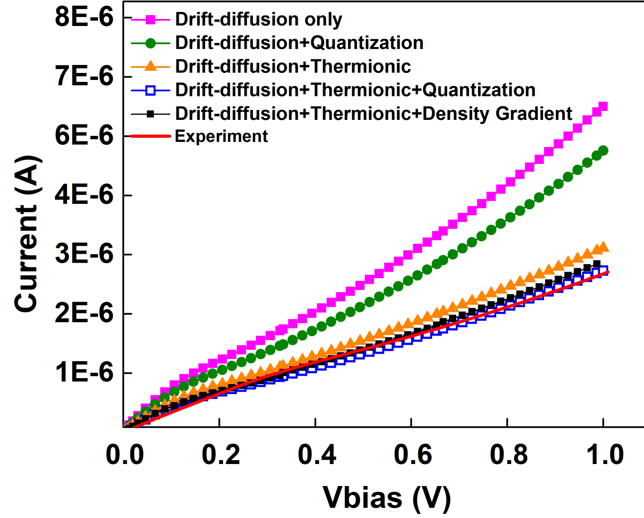

Figure 4.9: The dominant physical phenomena effecting carrier's dynamics and transport modeling at T=298 K in the $Si_{0.6}Ge_{0.4}$ MQW device leading to progressive prediction accuracy.

significantly as it discretizes (3.21 and 3.22) around the heterointerface for each mesh. Additionally, it employs thermionic emission heterointerface condition (3.36) of holes to determine the current density across the heterointerface. The net current density in this case reduces considerably due to band discontinuity which was ignored previously in *Case I* and *Case II*.

Finally, *Case IV* (both *Quantization = on, Thermionic= on*), treats simultaneously the heterointerface discontinuity and the hole density correction within the MQW for discrete energy levels and therefore, improves the model prediction farther as illustrated in Fig. 4.9. Moreover, the hole density determined either by local quantum well model (3) or density gradient quantization model (4) within the MQW are quite close as shown by their respective I-V plot in Fig. 4.9. The I-V characteristic trends are overall optimized by simultaneous fine tunning of ΔE_V and optimization of the candidate profiles via device simulation at room temperature (298 K).

4.3.2 Modeling Ge Content (x) in MQW

Increase in Ge content in $Si_{1-x}Ge_x$ directly influences the material bandgap by the amount of increase in valence band offset ΔE_V, whereas no appreciable change in the conduction band offset ΔE_C is observed, as shown in Figure 4.10. Thus, the net current density is estimated by using mole-fraction dependent bandgap $E_g(x)$ as a

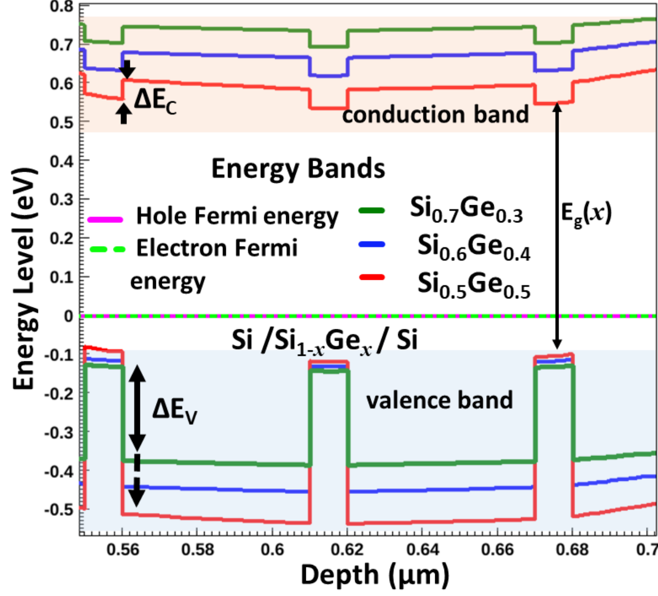

Figure 4.10: Energy band diagram indicating the increase in ΔE_V for higher x in $Si_{1-x}Ge_x$. The extracted barrier heights are $\Delta E_V \sim 0.25\,\text{eV}$, $0.35\,\text{eV}$, $0.45\,\text{eV}$ and $\Delta E_C \sim 41\,\text{meV}$, $49\,\text{meV}$, $51\,\text{meV}$ for $x = 0.3$, 0.4 and 0.5 respectively.

fitting parameter to map the transfer characteristics of the model to the experimental data. To model the "Ge effect", the estimated effective barrier height specified in terms of ΔE_V is interpolated between Si and Ge depending on x calculated by [70]. Increase in ΔE_V causes exponential increase in the resistance as shown in equation (2.3). Consequently, the carriers require large E_a to hop over the larger barrier, thus the net current through the device decreases in the case of higher x in the $Si_{1-x}Ge_x$ MQW.

Impact of Process Parameters on Electrical Characteristics:

The predictive modeling of the device requires a carefully parametrized the Ge and boron doping profiles. A thermodynamically stable box-like Ge profiles are included for simulation to emulate the abrupt Ge profiles and heterojucntions to cater the effect of carbon content in the presence of the C-delta layers. However, parametrization of the doping profiles requires multiple iterations to determine the best candidate profile accounting unintentional doping levels in the various intrinsic regions of the device for each Ge content. Figure 4.11 shows the flow diagram of the basic steps adopted to model Ge content in $Si/Si_{1-x}Ge_x$ MQW and optimization methodology employed for developing the best fit profiles.

i) Boron Doping Level

It is equally important to consider the p-doping levels in the intrinsic regions of

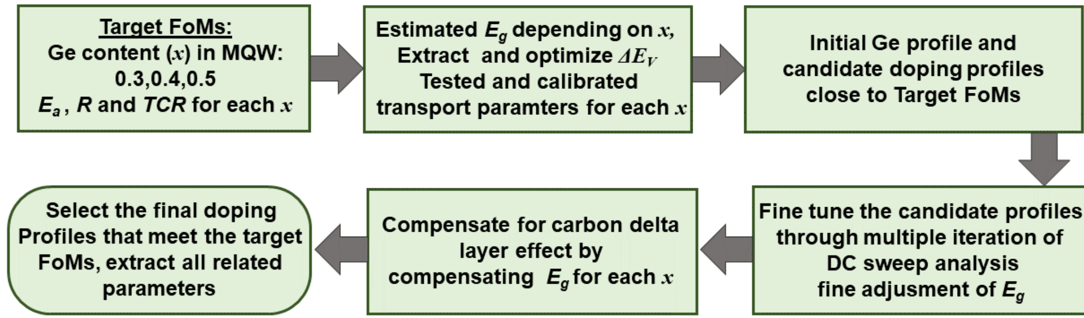

Figure 4.11: Model optimization methodology for given Ge content and the candidate doping profiles

the device due to unintentional background doping to improve the predictive behavior of the device model. Optimization and fine tuning of the candidate profiles are performed iteratively to finalize the profile that provides best fit of the model prediction to the measured I-V for any x in the $Si/Si_{1-x}Ge_x$ MQW. To model the background doping, the threshold p-doping levels along with the decay lengths (refer to Figure 4.12), are specified in the intrinsic regions to obtain a smooth profile gradient throughout the structure. Initially, the light doping of $1{\times}10^{14}\,cm^{-3}$ were assumed in both i-Si buffers and i-MQW. Then, the final profiles were optimized iteratively to predict comparable I-V response for each Ge content. I-V characteristics fitting is obtained by tuning ΔE_V together with the optimum candidate profile for the model fitting. The exhaustive iterative simulations based on various candidate profiles to fit the model, reveals that the overall electrical behavior of the device heavily relies on the background doping level. Moreover, the background doping levels becomes excessively high as the Ge content increases in MQW. Moreover, the measurement showed somewhat asymmetric I-V characteristics of $Si_{0.5}Ge_{0.5}$ MQW.

The asymmetry in I-V characteristics can also be attributed to either the Ge profile or the doping profile [40]. Considering the asymmetric background doping among the top and bottom i-Si buffers as one of the factors, the model reproduces the asymmetry as observed in the measurement. Various candidate profiles used for simulating $Si/Si_{0.5}Ge_{0.5}$ MQW are shown in Figure 4.12. Profile A is an abrupt transition profile and results in the symmetric I-V characteristics, whereas, Profile D with an asymmetric elevated doping level in the top Si buffer (Figure4.12) reproduces the I-V characteristics closely matched to the measurement as shown

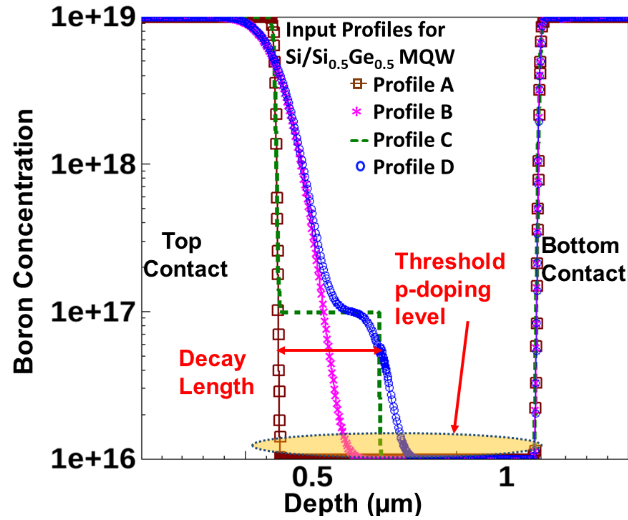

Figure 4.12: Various boron profiles incorporated in the $Si_{0.5}Ge_{0.5}$ MQW model. Profiles A and C show the abrupt transition whereas B and D are defined by specifying the decay lengths of 70 nm in the top Si buffer.

in Figure 4.13. Nevertheless, the best fit profile D obtained iteratively is in good agreement to the doping profile obtained by SIMS analysis (Figure 4.5) of the test structure. Therefore, it may be suspected that the longer processing time required by the RPCVD growth for the devices containing higher Ge concentration may cause the elevated background doping. The best fit profiles shown in Figure 4.14 were optimized iteratively to predict comparable I-V response for each Ge content. Based on these profiles and estimated ΔE_V from Figure 4.10, the reasonably matched I-V curves of $Si/Si_{1-x}Ge_x$ MQW for various x are obtained and presented in Figure 4.15

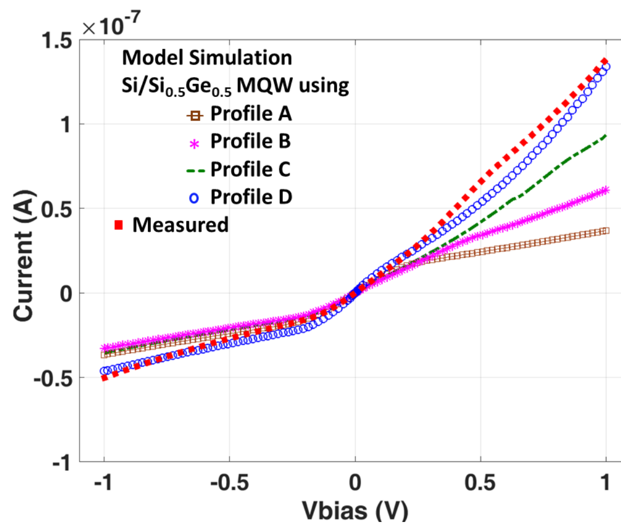

Figure 4.13: Employing profile D, model reproduces the asymmetry in I-V characteristics of $Si_{0.5}Ge_{0.5}$ which is quite in-line with the measured I-V.

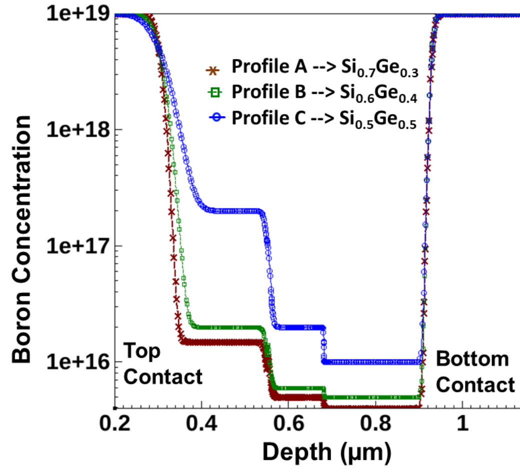

Figure 4.14: The optimized candidate profiles used for fitting the model and measured I-V for x= 0.3, 0.4 and 0.5.

at 298 K with an active device area of 17 µm × 17 µm.

Once the candidate profile are finalized, the device simulation is extended to the entire temperature range of 278 K - 323 K over the bias range ± 1 V. Figure 4.16 shows that the model prediction of I-V behavior is very well consistent and in agreement with the measured data for the various Ge content. The I-V characteristics of $Si_{0.7}Ge_{0.3}$ MQW are very well matched as compared to $Si_{0.6}Ge_{0.4}$ and $Si_{0.5}Ge_{0.5}$ MQW in, as the transport parameters are well calibrated for 30 % Ge concentration than 40 % and 50 % Ge concentration.

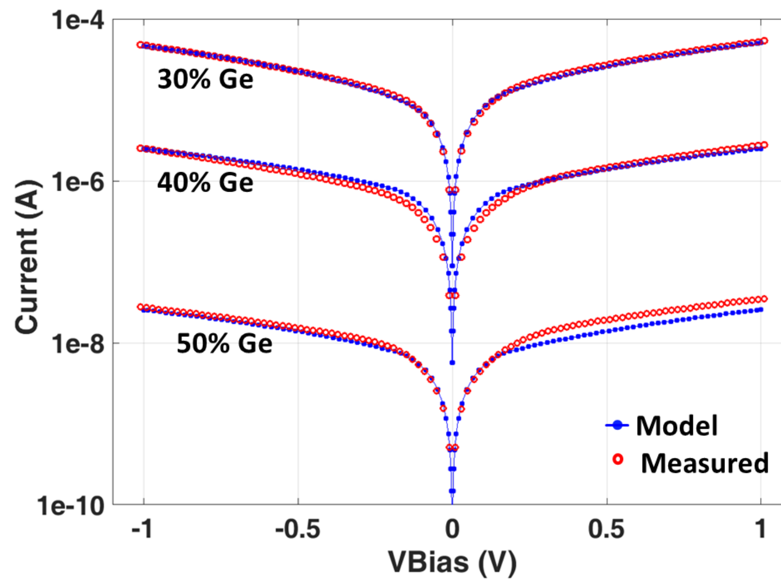

Figure 4.15: The transfer characteristics of the model validated with the experiment data for x = 0.3, 0.4, 0.5 in 17 µm × 17µm Si/$Si_{1-x}Ge_x$ MQW at 298 K using the best optimum profiles (Figure 4.14) and estimated ΔE_V (Figure 4.10).

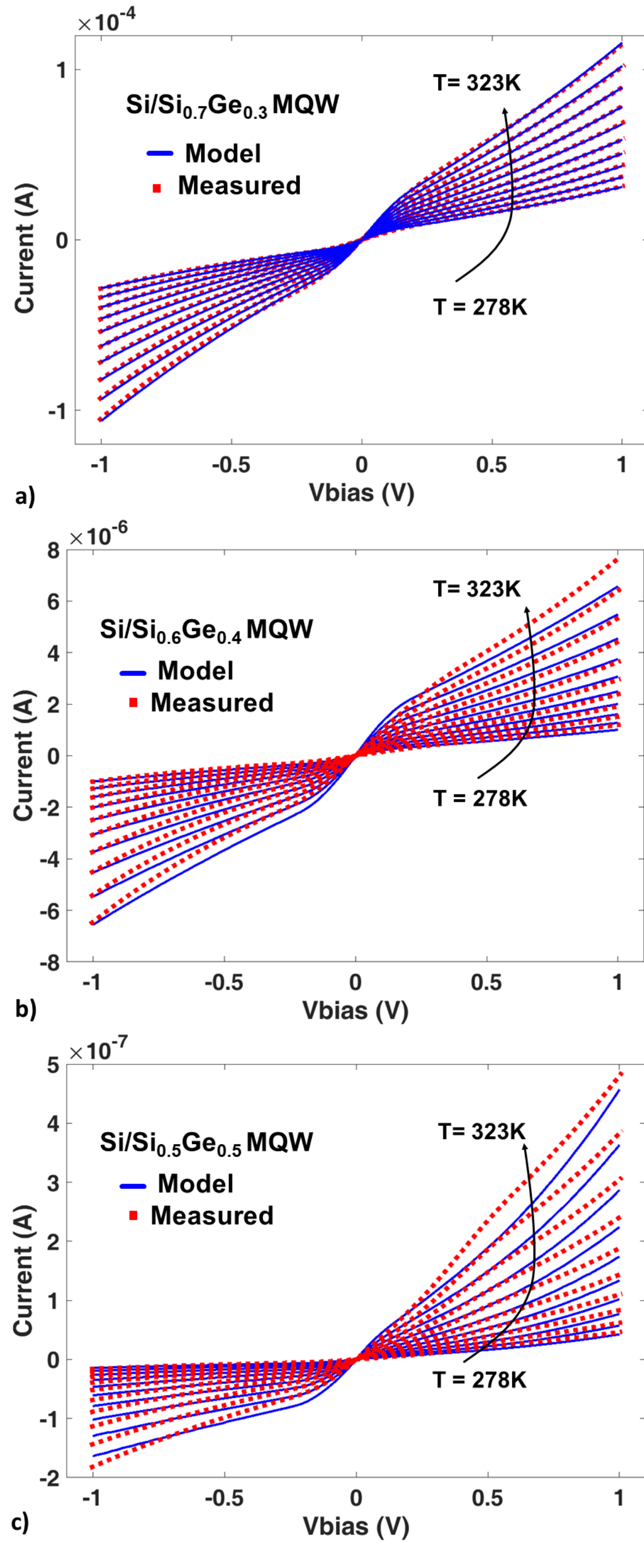

Figure 4.16: I-V fitting of the model and measured data extended over the entire temperature range of 278 K-323 K:
a) $Si_{0.7}Ge_{0.3}$ MQW with $\Delta E_V \approx 252\,\text{meV}$ and the doping profile A.
b) $Si_{0.6}Ge_{0.4}$ MQW with $\Delta E_V \approx 357\,\text{meV}$ and the doping profile B.
c) $Si_{0.5}Ge_{0.5}$ MQW with $\Delta E_V \approx 459\,\text{meV}$ and the doping profile C.

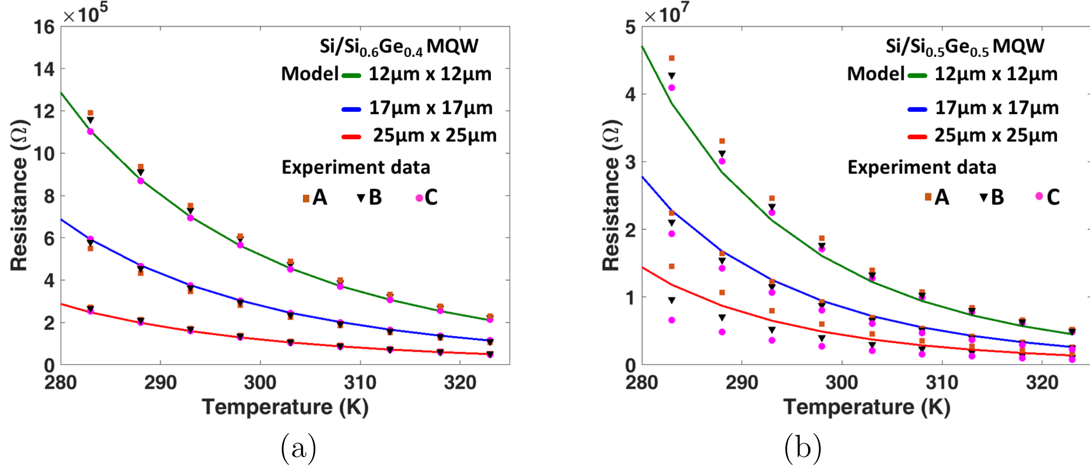

Figure 4.17: Variation of R over the temperature range for the nominal bias of 0.3 V, predicted by the model and validated with the experimental data in the $Si_{1-x}Ge_x$ MQW, a) for $x = 0.4$ b) for $x = 0.5$ for the various device active areas. Extracted E_a and TCR at 298 K for 0.3 V.

When the temperature of the device is increased, the more thermally excited carriers are available to hop over the Si barriers and hence the current increases. R plotted against the temperature range at nominal bias of 0.3 V is shown in Figure 4.17a for 40 % and Figure 4.17-b for 50 % Ge content, respectively in the MQW. The devices with the higher Ge content exhibit the larger resistance manifested by ΔE_V enlargement and thus requires more E_a to energize thermal emission of the carriers. Moreover, the effect of active device area on R is also investigated by comparing the devices of the active areas 25 µm × 25 µm, 17 µm × 17 µm, 12 µm × 12 µm. Resistance $R(T)$ as a function of E_a and T as previously mentioned in chapter 2 and restated here for convenience:

$$R(T) = R_0 \exp \frac{E_a}{k_B T} \tag{4.1}$$

where E_a is the activation energy and defined as the difference of $E_{F,p}$ and the valence band edge of Si as expressed in (Eq.3.2).

Equation (4.1) shows the exponential dependence of R on the temperature. TCR is related to activation energy and temperature as defined previously in (2.5), restated here for convenience:

$$TCR = \frac{1}{R}\frac{\partial R(T)}{\partial T} = -\frac{E_a}{k_B T^2} \tag{4.2}$$

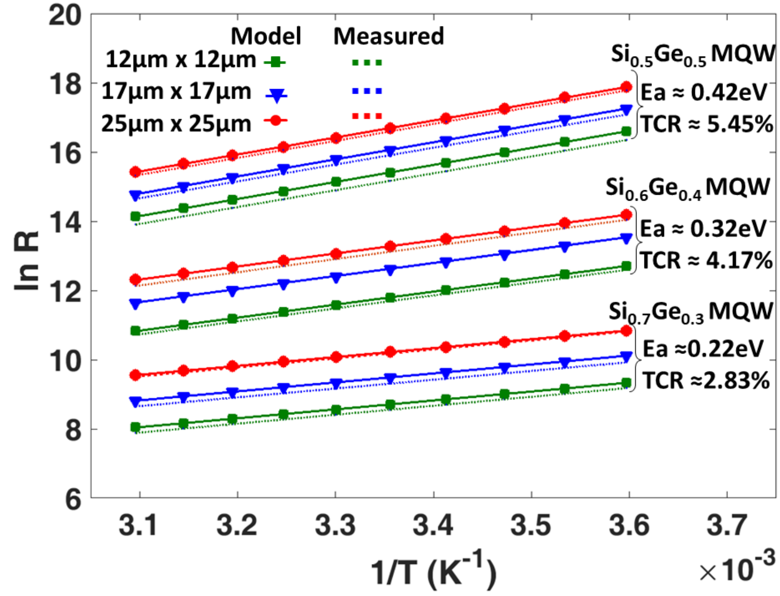

Figure 4.18: Extracted E_a for various Ge content and active areas at fixed bias of 0.3 V. The extracted values of E_a are in-line with the estimated band offset ΔE_V.

The linear fitting function has been used to extract E_a from the simulation and the experiment data by determining the slope (E_a/k_B) of Arrhenius plot in Figure 4.18. E_a and TCR depend primarily on the effective barrier height acquired by the amount of Ge in the MQW and thus remains same for a fixed x regardless of the device active area. Despite of the fact that the TCR of a semiconductor is negative according to (4.2), its temperature effect is more relevant in terms of an absolute

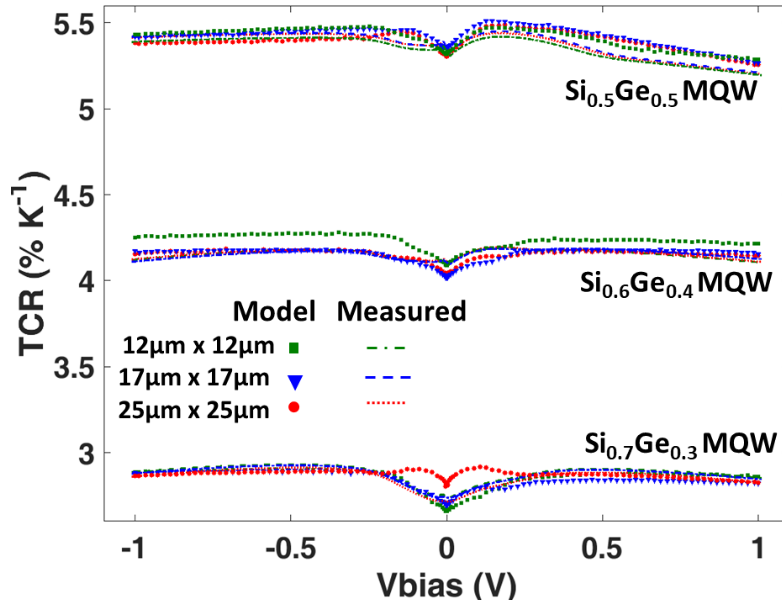

Figure 4.19: TCR increases with the Ge content x in MQW but remains same regardless of the active area for the given x in the $Si/Si_{1-x}Ge_x$ MQW.

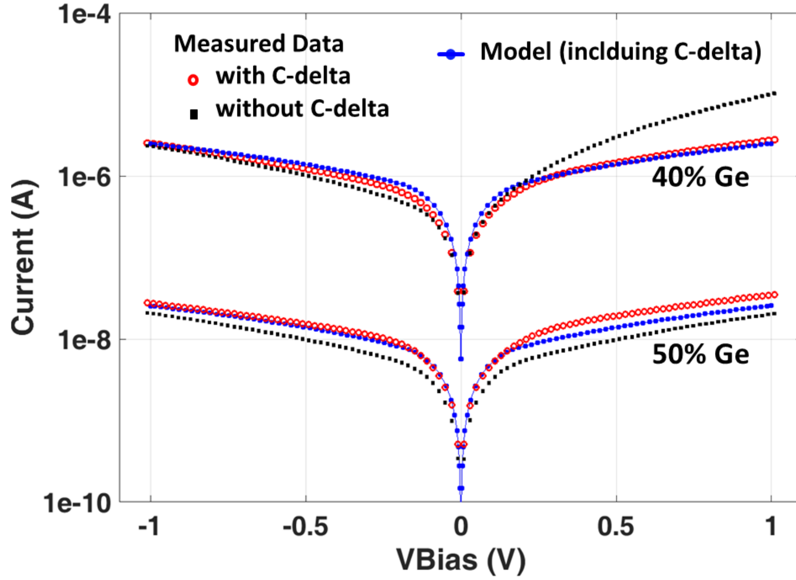

Figure 4.20: Measurement of the electrical characteristics of the device with and without C-delta layers in $Si/Si_{0.6}Ge_{0.4}$ and $Si/Si_{0.5}Ge_{0.5}$ MQW. The presence of C-delta layers shows no significant difference in the measured electrical characteristics.

value as presented in Figure 4.19 for convenience. The anticipated TCR behavior for various amount of Ge obtained from the model is well in agreement with the measurement as shown in Figure 4.19. TCR increases linearily from 2.8 $\%K^{-1}$ to 5.4 $\%K^{-1}$ as the Ge content in MQW increases from 30 % to 50 %. Furthermore, TCR remains substantially constant over the bias range of ± 1 V, nevertheless, it suffers slight roll-off in the case of $Si_{0.5}Ge_{0.5}$ MQW for the bias >0.5 V. The model also reproduces this roll-off in the TCR attributed to the considerable resistance nonlinearity caused by the nonuniform background doping in the top Si buffer.

ii) Influence of Carbon Content [2]

In order to analyze the effect of the C-delta layers at the Si/SiGe interfaces in the device with higher x, the fabrication of the test structures was also carried out without including the C-delta layers at the interfaces. Addition of C-delta layers at the interface forming ternary alloy causes somewhat slightly lower bandgap narrowing than the binary alloy SiGe (without any C-delta layers). The effect of carbon content on the bandgap offset is considered insignificant as compare to the constituent Ge content. Through the measurement of the transfer characteristics of the both fabricated test structures with and without the C-delta layers, it is deduced that the presence of carbon does not effect the electrical characteristics significantly.

[2] this work is a part of a peer-reviewed journal publication [106]

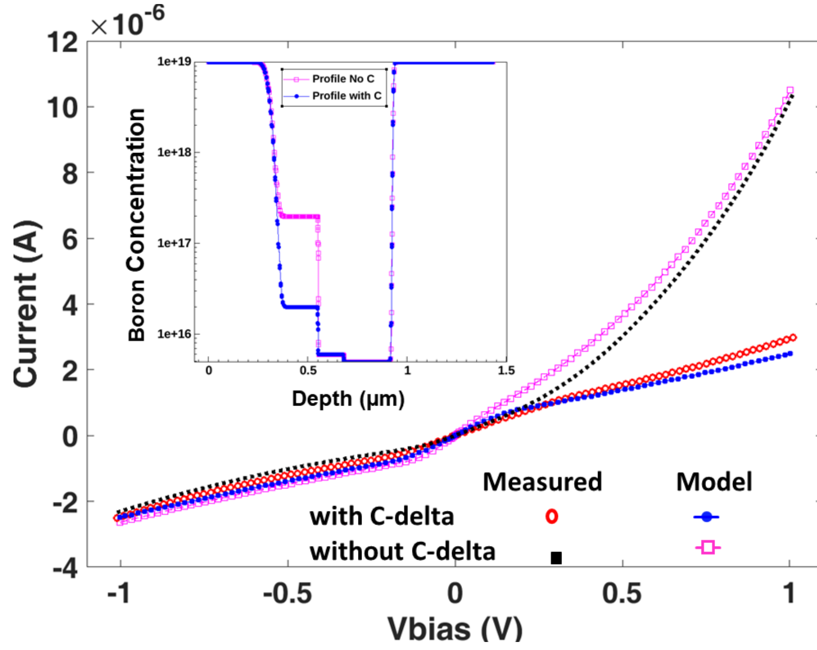

Figure 4.21: The model reproduces the asymmetric deviation in I-V characteristics of Si/$Si_{0.6}Ge_{0.4}$ MQW (without C-delta layers) matched to the measured data using the non-uniform doping profile given in the inset plot.

The I-V characteristics of model can be reproduced and fitted to the measured I-V characteristics of the devices without any C-delta layer by modifying ΔE_V such that the bandgap narrowing is more in $Si_{1-x}Ge_x$ for a given Ge content. In consequence to more bandgap narrowing (larger bandoffset), the net current through the device (without C-delta) decreases as the carrier density across the barrier is reduced as shown in Figure 4.20. The plot in Figure 4.20 for $Si_{0.5}Ge_{0.5}$ MQW without C-delta layers shows the measured current density is slightly less as compared to the device with C-delta. The model can be mapped to the characteristics of devices without C-delta layers by increasing the ΔE_V. However, in the case of $Si_{0.6}Ge_{0.4}$ MQW without C-delta, the I-V response is nearly same for the negative bias but more asymmetric for the positive bias. As already discussed in the preceding section, the asymmetry in the I-V characteristics is attributed to the non-uniform boron doping in the top buffer. In the case of $Si_{0.6}Ge_{0.4}$ MQW without C-delta, fitting of the model to the measurement is obtained by using the profile *Profile No C* (refer to the inset in Figure 4.21) together with the recalibration of ΔE_V up to $6 \sim 8\,\text{meV}$. TCR remains substantially constant over the bias range of $\pm 1\,\text{V}$, nevertheless, it suffers slight roll-off in case of $Si_{0.6}Ge_{0.4}$ MQW without C-delta for bias >0.5 V, as shown in Figure 4.22. The model also reproduces the roll-off trend in the TCR owing to

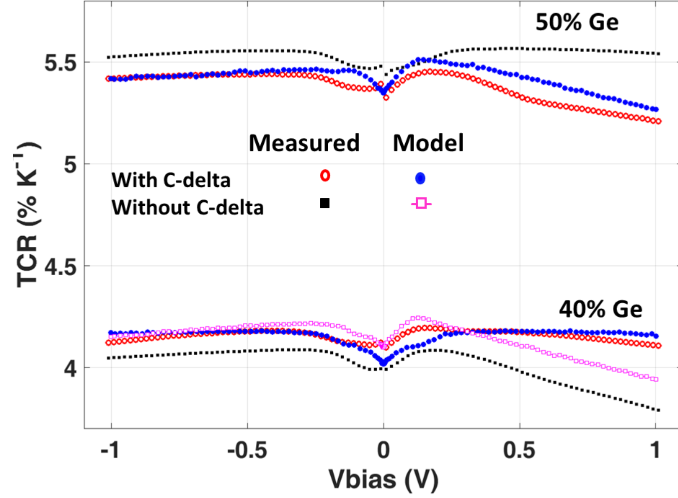

Figure 4.22: The carbon content does not cause explicit change in TCR. The roll-off in TCR over the bias range is attributed to the nonlinearity in R in consequence to the non-uniform doping.

the considerable resistance nonlinearity and asymmetry caused by the non-uniform background doping.

iii) Self-Heating Effect

Typically, R in the semiconductor device has inherent non-linearity as illustrated in Figure 4.23 with respect to the bias at temperature T = 298 K. A slope of the differential resistance ∂R decreases due to Joule self-heating effect. When the bias across the device exceeds 0.5 V, the current flowing through the device causes the device to heat up which in return decreases the absolute R because of negative thermal feedback. Consequently, this negative thermal feedback restricts the region of operation of the device due to the desired linearity constraint. The self-heating effect

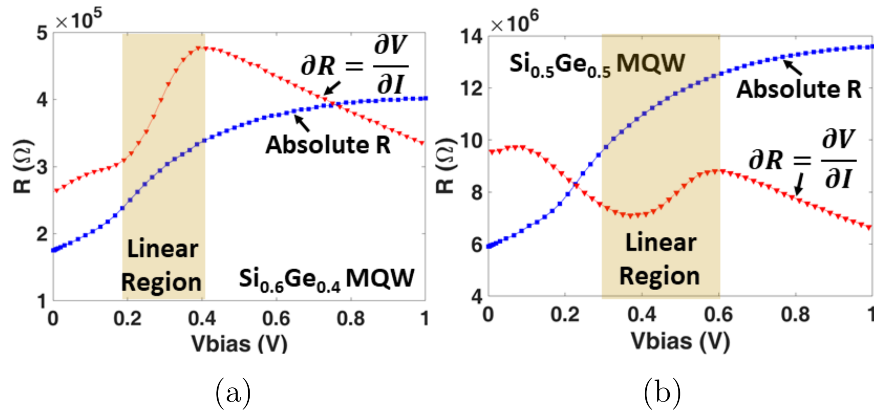

Figure 4.23: Self-bias heating effect illustrated by ∂R in (a) $Si_{0.6}Ge_{0.4}$ MQW and (b) $Si_{0.5}Ge_{0.5}$ MQW. The larger R in $Si_{0.5}Ge_{0.5}$ MQW allows extended linear region of operation as compared to $Si_{0.6}Ge_{0.4}$ MQW.

exacerbates further in the case of device with lower resistance. $Si_{0.6}Ge_{0.4}$ MQW device suffers from the self-heating even at the lower bias value as compare to $Si_{0.5}Ge_{0.5}$ MQW. Thus, it can be concluded that to counteract the self-heating effect, the device with a larger resistance is preferred.

4.3.3 Quantum well (QW) Periodicity

To investigate the effect of well periodicity, the test devices comprising single and double stacked $Si_{0.5}Ge_{0.5}$ MQW layers (refer Figure 4.24), were also fabricated and characterized. Since the current transport through the device is perpendicular to the quantization direction, the net current through the device increases for a fixed temperature under same bias as shown in Figure 4.25-a as the vertical path resistance decreases.

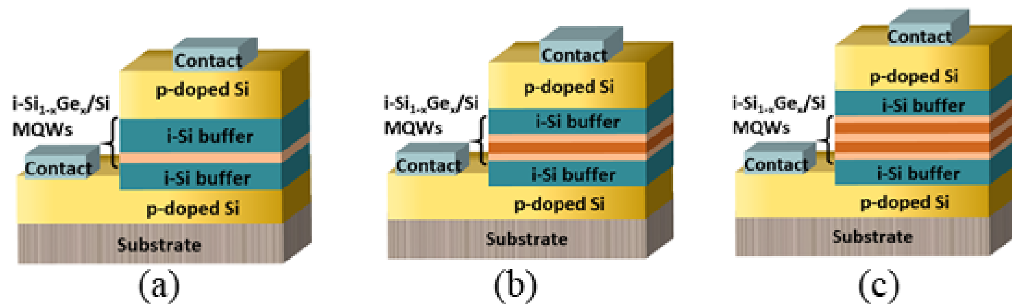

Figure 4.24: Schematic representation of a) Single quantum well stack b) Double quantum well stack c) Triple quantum well stack.

The experimental data analysis of single and double stacked test devices also revealed that I-V characteristics suffer from more asymmetry and nonlinearity as compared to three stack device owing to the substantial nonuniform background doping. The model predicts I-V reasonably matched to the experimental data with the prior estimated barrier height in the case of 50 % Ge content, whereas, the best fit doping profile is determined by re-iterating the candidate profile. The extracted E_a is 0.41 eV which is same as in the triple stacked $Si_{0.5}Ge_{0.5}$ MQW, owing to the same barrier height for all single, double or triple stacked MQW with fixed 50 % Ge content. Thus, the TCR is more or less same around the zero-bias region for all single, double and triple stacks. Nevertheless, TCR suffers considerable asymmetric roll-off in case of the single well device, attributed to nonuniform background doping leading to significant nonlinear resistance variation over the bias range shown in

Fig. 4.25-b. The model affirms this asymmetric roll-off manifested with the aid of nonuniform doping in the Si buffers.

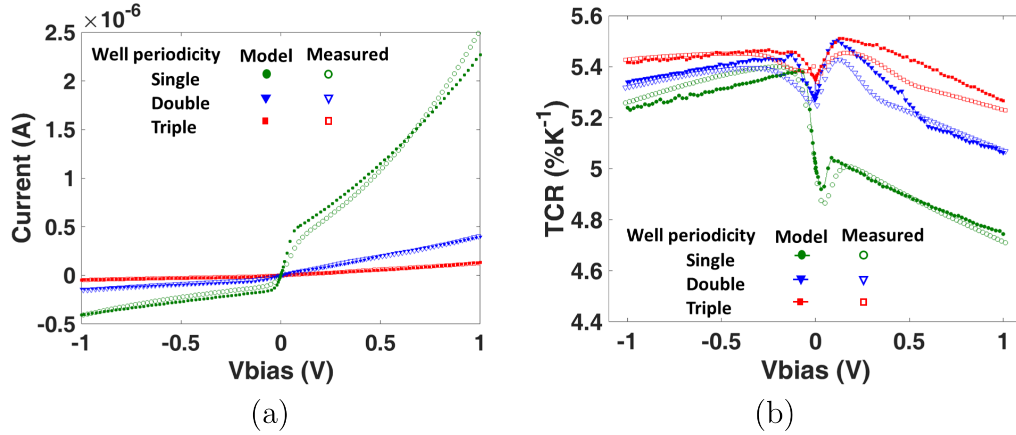

Figure 4.25: a) I-V response for different number of well stacks containing 50 % Ge content at T=298 K. b) The model predicts the TCR roll-off which is in good agreement with the measurement attributed to the asymmetric nonuniform background doping.

4.3.4 Background Doping

Once the I-V characteristics of the model were optimized and validated for each Ge content, the predictive capability of the model is employed to investigate the effect of various design constraints to optimize the desired performance metrics from the detector perspective. The unintentional doping of boron impurity in various regions of the device is one of the main design constraints causing nonlinearity in R and TCR degradation over the bias range as discussed previously. To illustrate the effect of background doping on the overall performance, the doping in the i-

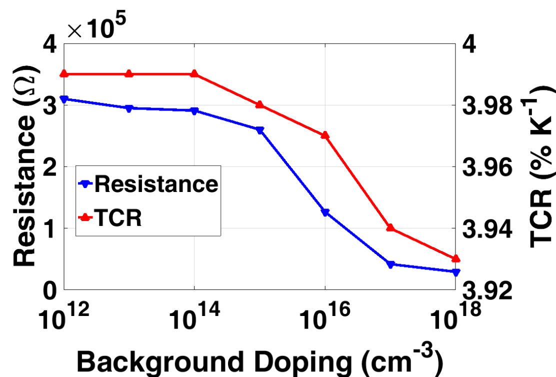

Figure 4.26: TCR drops in the device with the $Si_{0.6}Ge_{0.4}$ MQW at a fixed bias of 0.3 V due to the elevated background doping level.

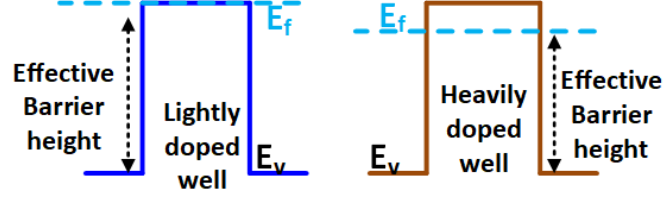

Figure 4.27: Quasi-fermi level shifts as a result of boron doping in MQW.

Si buffers was varied in the range $1\times10^{12}\,\text{cm}^{-3}$ to $1\times10^{18}\,\text{cm}^{-3}$ in the simulation. Both R and TCR remain unaffected until $1\times10^{15}\,\text{cm}^{-3}$ but decreases as the doping exceeds $1\times10^{15}\,\text{cm}^{-3}$, as shown in Figure 4.26. The rate of TCR drop aggravates on higher bias values due to enhanced nonlinearity in R caused by the elevated non uniform doping and therefore, limits the region of operation. The background doping effect can be mitigated by either increasing thickness of the i-Si buffers or by increasing the periodicity of i-MQW which comes at the cost of larger R.

4.3.5 Boron Doping in MQW

Figure 4.19 shows that the higher TCR can be obtained by increasing Ge content in the MQW but at the expense of the larger R (Figure 4.17) owing to the larger ΔE_V. A large resistance signifies a higher Johnson noise linearly dependent on R. Therefore, from a detector perspective to enhance the thermal sensitivity, it is equally important to reduce R by selectively doping the $Si/Si_{1-x}Ge_x$ MQW.

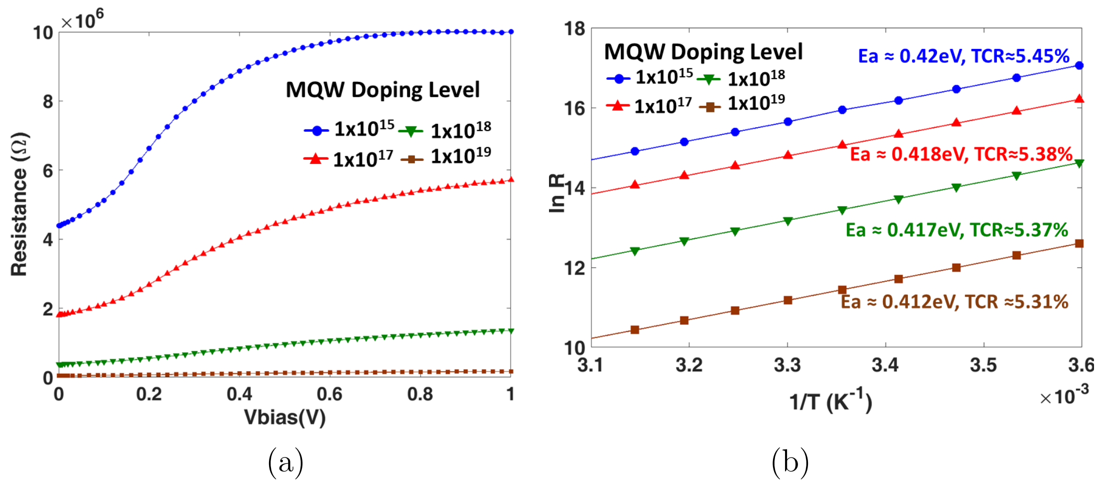

Figure 4.28: a) Boron doping in the $Si_{0.5}Ge_{0.5}$ MQW causes R to reduce from $8\,\text{M}\Omega$ to $93\,\text{K}\Omega$ for Vbias= $0.3\,\text{V}$ at T=298 K b) TCR drops induced as a consequence of the heavily doped MQW $\approx 1\times10^{19}\,\text{cm}^{-3}$.

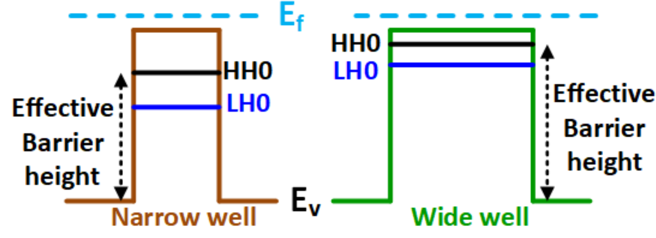

Figure 4.29: In a wider well HH0 occupies the lowest ground state energy as compared to a narrow well, where the HH0 shifts to the higher energy level.

Nevertheless, doping in the MQW must be optimized carefully without deteriorating TCR. Doping MQW shifts the $E_{F,p}$ closer to the top of the valence band as indicated in Figure 4.27. Thus the hole concentration increases in the MQW and the resistance reduces corresponding to the doping level as shown in Figure 4.28-a. $E_{F,p}$ moves farther into the valence band with heavy doping $\approx 1{\times}10^{19}\,\text{cm}^{-3}$ which ultimately reduces the effective barrier height, subsequently the TCR drops as shown in Fig. 4.28-b.

4.3.6 Quantum Well Thickness

The well thickness is another design parameter which can be optimized beside Ge content for further TCR enhancement. Though in the case of a strained $\text{Si}_{1-x}\text{Ge}_x$ alloy the well thickness is already constrained by the critical thickness criteria for a given x in the metastable region [66]. The ground energy state HH0 lies near

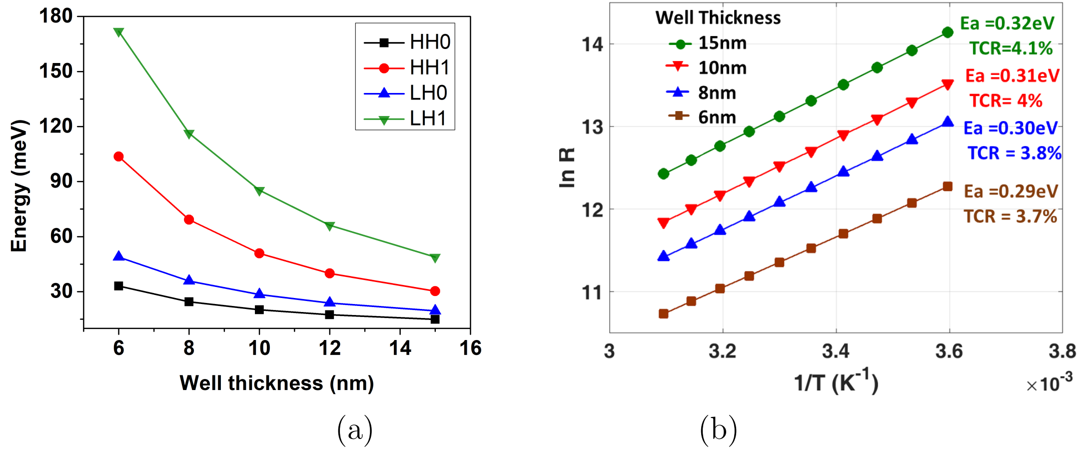

Figure 4.30: a) HH0 occupies the lowest energy as the well thickness increases, b) E_a and TCR increases due to increased effective barrier height for the fixed 40 % Ge content in the MQW for a wider well.

the top of $Si_{1-x}Ge_x$ MQW valence band occupying the minimum energy level in a thick well as indicated in Figure 4.29. Shrinking the well thickness shifts the HH0 away from the valence band edge towards the higher energy states which in return reduces the effective barrier height (refer to the narrow well presented in Figure 4.29). The quantitative change in the energy value of HH0 and LH0 corresponding to well thickness are plotted in Figure 4.30-a. Consequently, decrease in effective E_a causes TCR degradation as shown in Figure 4.30-b. However, exceeding the well width more than 12 nm - 15 nm shows no appreciable increase in TCR.

4.4 Noise Measurement

As discussed in the chapter 2, the electrical noise in a resistive device mainly comprises of two components: Flicker noise ($1/f$) and Johnson noise. $1/f$ noise is mainly material related noise depending on the value of Hooge's parameter and the carrier concentration. $1/f$ noise is termed as "pink noise", having peak power spectral density (PSD) at lower frequencies. On the other hand, the Johnson noise is a function of device resistance and the bandwidth of the measurement. Johnson noise described as "white noise"and having PSD across the entire spectrum. Both $1/f$ and Johnson noise contribute to the net PSD measured in V^2Hz^{-1}. $1/f$ noise component ($V_{1/f}$) dominates on the lower frequencies, while the Johnson noise component (V_J) dominates at higher frequencies. The measurement system includes a low noise voltage amplifier, an input low pass filter and a dynamic signal analyzer as represented in Figure 4.31. The detector has been characterized by measuring PSD in the frequency range of 1 Hz - 100 kHz for the test devices containing various amounts of Ge content in the $Si/Si_{1-x}Ge_x$ with various active areas at multiple bias points (0.1 V, 0.5 V, 1 V).

4.4.1 Effect of Ge Content

The measured noise PSD of $Si/Si_{1-x}Ge_x$ MQW is plotted for various Ge contents $x = 0.3$, 0.4, 0.5 in Figure 4.32 at nominal bias of 0.5 V. It is clearly observed that below 50 Hz the characteristics $1/f$ noise dominates, while at higher frequencies the Johnson (thermal) noise dominates the overall device noise. Moreover, the overall noise floor in the detector increases as the Ge content increases from 30 % up to

50 % in $Si/Si_{1-x}Ge_x$ MQW. The higher Johnson noise is manifested by the larger resistance attributed to the presence of a larger barrier due to the higher Ge content in the undoped SiGe wells the detector. $1/f$ noise also increases order of magnitude as Ge content is increased from 30 % to 50 %.

4.4.2 Effect of Bias Voltage

It is also apparent from the measured PSD plots that the Johnson noise decreases as the bias applied across the detector is increased, whereas, $1/f$ noise increases proportionally with the increase in the bias voltage as expressed in equation (2.36). The effect of bias voltage on the overall detector noise for various amount of Ge content is shown in Figure 4.33. This fact brings forth the trade-off between self-heating and noise. Typically, a small bias voltage (0.3 V) is preferred to be applied across the detector to overcome the non-linearity and dynamic range artifacts manifested by self-heating while a higher bias voltage is required to reduce the Johnson noise in the operational bandwidth.

4.4.3 Effect of Active Area

Figure 4.34 presents the effect of active device area on the noise performance for a fixed Ge content. As it can be seen that decreasing the active area increases the Johnson noise for Ge content of 40 % at a fixed bias of 0.5 V but $1/f$ noise remains same for all three areas. As $1/f$ noise component varies in proportion to the Ge content, thus, for the fixed Ge content it remained unaltered regardless of the active device area. On the other hand, the resistance is inversely proportional to the area, therefore, reducing the active area further increases the resistance and subsequently

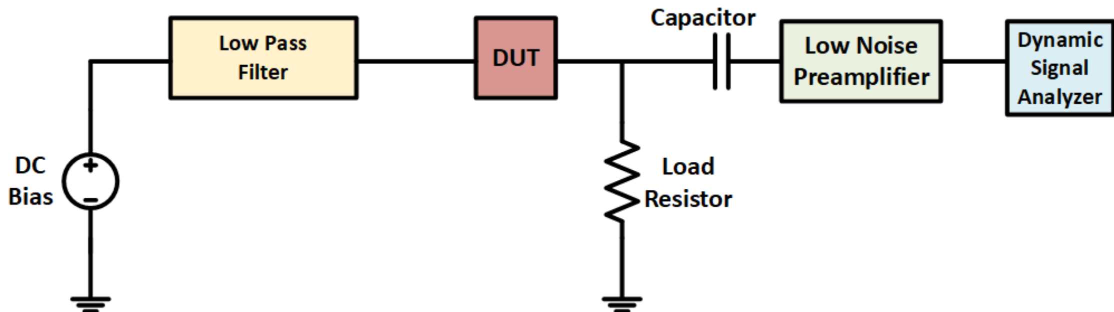

Figure 4.31: Schematic representation of the noise measurement setup.

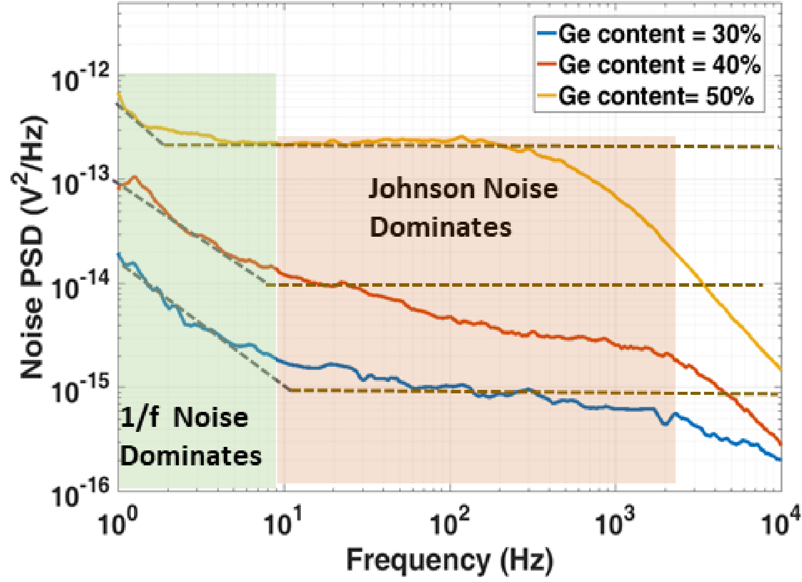

Figure 4.32: Measured noise PSD for various Ge content at nominal bias of 0.5 V.

resulting the higher Johnson-Nyquist noise. Moreover, it is also apparent that area reduction shifts the corner frequency to lower value, as the Johnson noise starts dominating over $1/f$ even below 10 Hz.

4.5 Performance Comparison

To this end we can conclude that it is equally important to consider the noise of the device beside TCR. To enhance the overall thermal sensitivity and to achieve larger SNR, not only to have larger TCR but the low noise is equally important. Increasing the Ge content from 30 % to 50 % increases the TCR from 2.9 %K^{-1} to 5.4 %K^{-1} in Si/SiGe MQW detector when compared to the other semiconductor based detector given in Table 10. The increase in TCR employing higher Ge content in MQW comes at the cost of higher noise induced mainly due to larger R. Table 11 summarizes the performance of Si/Si$_{1-x}$Ge$_x$ MQW detector obtained in this work in terms their of TCR, R and PSD. Henceforth, it is inevitable to optimize and reduce R by the selectively and carefully optimized p-doping in Si$_{0.5}$Ge$_{0.5}$ such that R can be reduced, without compromising TCR. Likewise, the device noise can be reduced and the overall FoM can be improved.

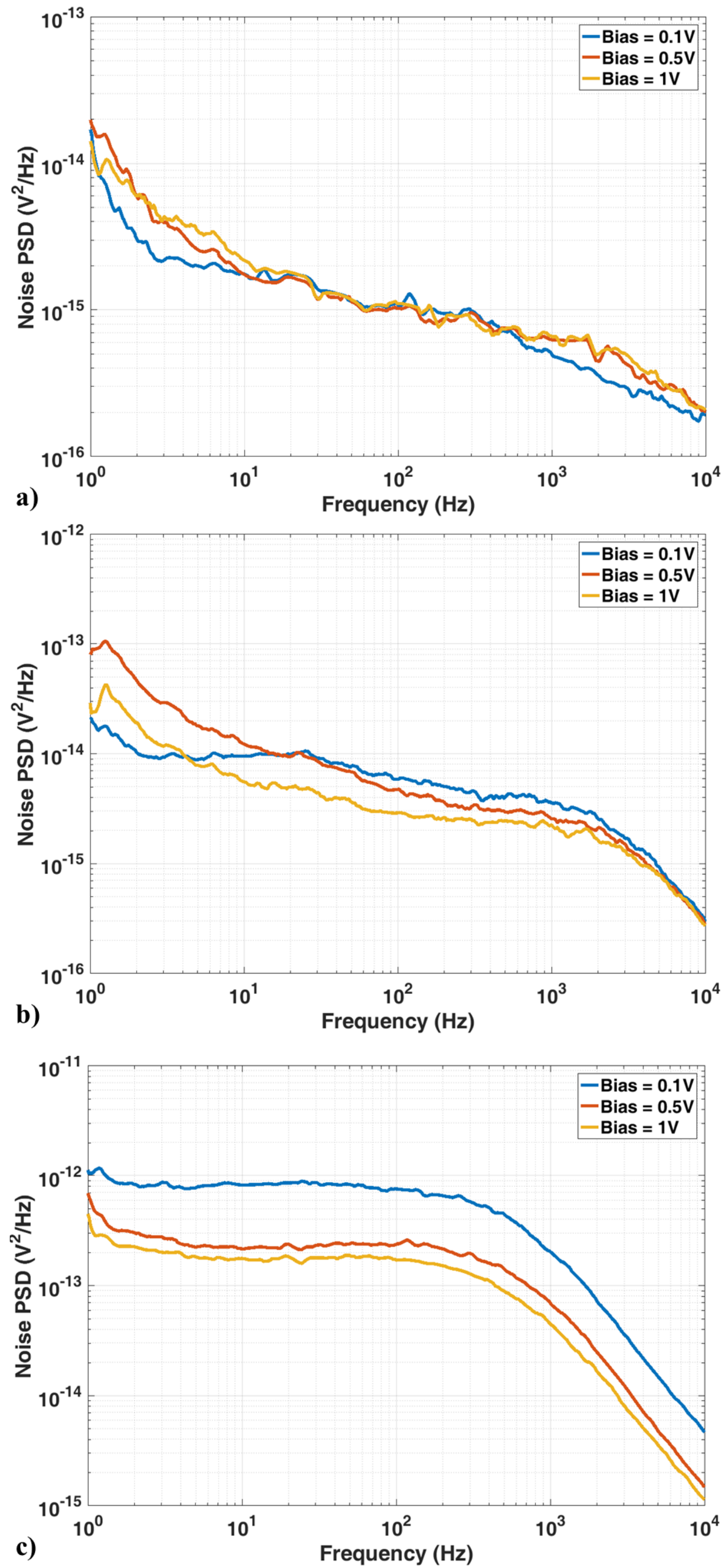

Figure 4.33: Measured noise PSD at various bias points:
a) $Si_{0.7}Ge_{0.3}$ MQW where characteristic $1/f$ is seen below 50 Hz.
b) $Si_{0.6}Ge_{0.4}$ MQW where characteristic $1/f$ is seen below 30 Hz.
c) $Si_{0.5}Ge_{0.5}$ MQW where characteristic $1/f$ is seen below few Hz.

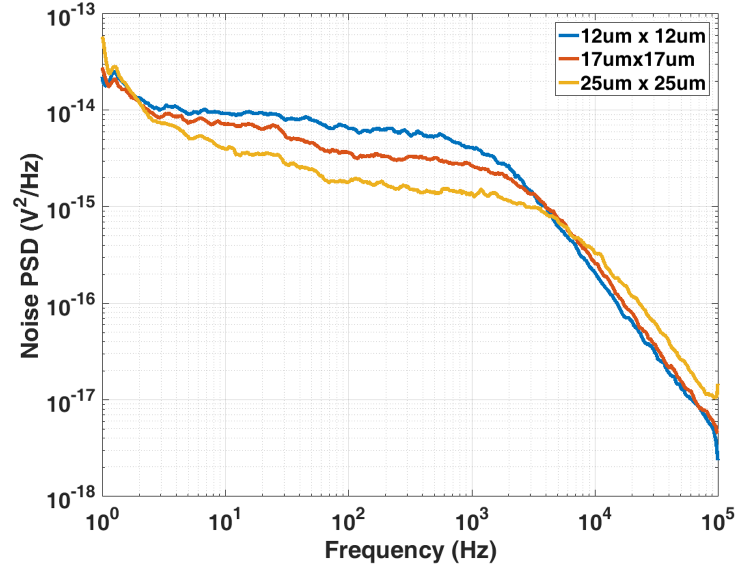

Figure 4.34: The measured noise PSD of $Si_{0.6}Ge_{0.4}$ MQW at fixed bias of 0.5 V.

Table 10: Comparative analysis with the other semiconductor based detectors.

Material	TCR %K $^{-1}$	PSD V^2/Hz^*	Pixel Area µm^2	Reference
VO_x	2	1.2×10^{-13}	100 × 100	[32]
a-Si:H	3.3	1×10^{-14}	17 × 17	[33]
Si/SiGe QW	3	1×10^{-14}	25 × 25	[58]
Ge/SiGe MQW p-i-n	5.8	1×10^{-10}	-	[107]
pm-SiGe:H	6.6	5.2×10^{-12}	50 × 50	[30]

*in the frequency range of 1-100 Hz

Table 11: Performance summary of the $Si/Si_{1-x}Ge_x$ MQW in this work for different Ge contents and active areas.

Detector Area µm^2	Ge content x	R Ω	TCR %K^{-1}	PSD V^2/Hz^*
12 × 12	30 %	2×10^{4}	2.9	1.2×10^{-15}
	40 %	6×10^{5}	4.2	6.8×10^{-15}
	50 %	16×10^{6}	5.5	9×10^{-13}
17 × 17	30 %	1×10^{4}	2.9	1.07×10^{-15}
	40 %	3×10^{5}	4.2	3.8×10^{-15}
	50 %	8×10^{6}	5.5	2.8×10^{-13}
25 × 25	30 %	6×10^{3}	2.9	2.7×10^{-16}
	40 %	1×10^{5}	4.2	2.2×10^{-15}
	50 %	4×10^{6}	5.5	8.7×10^{-14}

*in the frequency range of 1-100 Hz

5 Chapter 5

Conclusions and Future Directions

This research aimed to model and characterize the high performance and cost-effective monocrystal SiGe multi-quantum wells (MQW) based microbolometer for the uncooled thermal image sensing. For commercial and consumer applications thermal imaging is stymied by cost, size, and weight of imagers. Thus, reduction of manufacturing cost and smaller size pixels, ease of integration are the key parameters to establish newer technologies. The tremendous efforts to perpetual research for new materials and innovative devices has steered up to meet the industry standard of IR cameras concerning both higher sensitivity and lower noise. a-Si technology was born out of a desire for a small, lightweight, low-cost IR imager. Some of the recent work based on polycrystalline SiGe, SiGe multi-quantum-well structure gathered considerable attention due to their high TCR values. The higher Ge content is proposed to increase the thermal sensitivity of the SiGe MQW. An epitaxially grown $Si/Si_{1-x}Ge_x$ MQW detector has been distinguished as a potential candidate to improve the TCR owing to its monocrystalline properties and the inherent fringe benefit of ease of the bandgap tailoring by increasing the Ge content up to 50 %.

The higher Ge content in $Si/Si_{1-x}Ge_x$ MQW aids to enhance the thermal sensitivity of the detector by improving the TCR up to $5.4\,\%K^{-1}$. Nevertheless, higher TCR signifies the higher thermal sensitivity which comes at the cost of the higher noise. In recent years, higher Ge content in such MQW structures are shown to increase TCR values, but all efforts so far were limited to below 35 % Ge. Incorporating higher Ge content in MQW comes with two fundamental problems: Firstly, due to the lattice mismatch between Si and SiGe, the interface creates stress and dislocations. Thus, the strain relaxation set the upper limit on the amount of the band offset that can be achieved by adding Ge, limiting the Ge content and the thickness of the SiGe layer that can be used. Secondly, beyond the critical thickness, the dislocations in the partially relaxed SiGe give rise to the generation-recombination noise causing dysfunctionality affecting electrical characteristics of the device and deteriorates the performance of the detector due to higher noise. The development of the peculiar process to grow strained SiGe layers with higher Ge content, mean-

while maintaining the alloy stability to avoid the formation of misfit dislocations which are detrimental to detector performance.

The fabrication process development is challenging and costly, therefore, the predictive technology computer-aided design (TCAD) tool is used to obtain a priori estimate of the detector characteristics. These estimates are used to investigate the device design challenges and optimization issues. The primary requirement for such modeling methodology is to reproduce the actual characteristics of a structure under consideration. They must be predictive models, not overly idealized.

Earlier work based on theoretical analysis [39] and a numerical model [40] for such structure with 30 % Ge has been reported using either the drift-diffusion or the quantum mechanical solution where the current transport across the heterointerface is not considered explicitly. Without considering heterointerface boundary condition, a numerical device solver does not solve current continuity equations across the interface but assumes continuous quasi-fermi levels across the interface which overestimates current through the device.

This work focuses on the model and design of $Si/Si_{1-x}Ge_x$ MQW detector incorporating optimum Ge content to increase TCR without deteriorating detector noise performance. A comprehensive integrated modeling framework and methodology developed for predictive optimization of $Si/Si_{1-x}Ge_x$ multi-quantum well device as a potential candidate for the thermal detector. Coupled Poisson-Schrodinger equation in conjunction with the thermionic emission theory and the drift-diffusion transport is implemented to model the carrier transport dynamics. The region-wise device segregation within the integrated modeling framework shows the physical phenomena governing the carrier's transport dynamics.

The fitting of the model to the measurement is obtained by adjusting the effective barrier height and the careful optimization of the candidate doping profiles. The predictive modeling of the device requires the use of carefully parametrized the Ge and doping profiles. A thermodynamically stable box-like Ge profiles were included for the simulation to emulate the abrupt profiles. However, parametrization of the doping profiles requires multiple iterations to determine the best candidate profile accounting unintentional doping levels in the various intrinsic regions of the device for each Ge content. The predicted I-V behavior of the device validated with

measured I-V characteristics supports the modeling prediction accuracy. The experimental data and the model agree over a wide range of Ge content with adequate prediction accuracy. The model also validates the enhancement trend in TCR attributed to the Ge increase in the Si/$Si_{1-x}Ge_x$ MQW, which is particularly desired for a thermally sensitive detector.

The model is employed to investigate the design trade-offs (Ge content, well periodicity, well thickness) to achieve FoM for a thermally sensitive detector in terms TCR, R and the noise. The model predicts that TCR can be enhanced by increasing the Ge content in MQW but at the expense of larger R, though the larger R favors to counteract the self-bias heating. TCR exhibits fairly symmetric behavior over the bias for a three stacked device and remains uniform regardless of the active area for a fixed Ge content. The model also demonstrates that the non-uniform background doping steers nonlinearity and asymmetry in I-V characteristics as Ge content increases and exacerbates further in the case of single and double well devices comprising higher Ge content, which ultimately leads to nonlinear variation in R and deteriorate TCR. Furthermore, it is illustrated via modeling that R can be reduced to an acceptable value from a thermal detector perspective via optimized selective doping of the MQW such that TCR remains unaffected. Moreover, it is also demonstrated that the wider well assists to enhance TCR beside the higher Ge content.

The characterization (EDXS, XRD, and SIMS) analysis of the test devices has also included analyzing the crystal growth and alloy properties. Noise is equally an important parameter which must be considered beside TCR for improving overall performance metric for a thermal detector. The noise power spectral density of various test devices have been measured. It has been noted through measurement the noise PSD increases as the Ge content in Si/$Si_{1-x}Ge_x$ MQW increases. Henceforth, the Ge content in the detector needs to be optimized based on the desired thermal sensitivity versus noise trade-off.

Future possible directions include the fabrication process modeling in the TCAD to extract the accurate doping profiles in the device to eliminate the measurement errors and the iterative simulation process. Moreover, the thermal modeling of the device is critical to investigate the impact of the self-bias heating phenomena on

the device reliability and stability. In this regard, employing the hydrodynamic model instead of drift-diffusion model for the carrier transport may produce more realistic device behavior. Also, including the absorber and the reflector layers to the MQW stacks is essential to simulate the detector response under optical input. The simulated optical response of the detector can be verified by the measurement of DC responsivity. Additionally, the thermal AC parameters of the final suspended structure to extract the thermal time constant and thermal conductance is very important to realize a microbolometer.

References

[1] https://www.infratec.eu/thermography/industries-applications/building-thermography/. [Accessed:15-July-2018].

[2] L. J. Jiang, E. Y. K. Ng, A. C. B. Yeo, S. Wu, F. Pan, W. Y. Yau, J. H. Chen, and Y. Yang, "A perspective on medical infrared imaging," *Journal of Medical Engineering & Technology*, vol. 29, no. 6, pp. 257–267, jan 2005.

[3] https://www.ximea.com/en/industrial-camera-guide. [Accessed:15-July-2018].

[4] http://www.flir.co.uk/cs/display/?id=42107. [Accessed:22-Jun-2018].

[5] P. Tribolet and G. Destefanis, "Third generation and multicolor IRFPA developments: a unique approach based on DEFIR (invited paper)," in *Infrared Technology and Applications XXXI*, B. F. Andresen and G. F. Fulop, Eds. SPIE, may 2005.

[6] C.-C. Hsieh, C.-Y. Wu, F.-W. Jih, and T.-P. Sun, "Focal-plane-arrays and CMOS readout techniques of infrared imaging systems," *IEEE Transactions on Circuits and Systems for Video Technology*, vol. 7, no. 4, pp. 594–605, 1997.

[7] K.-P. M. Michael Vollmer, *Infrared Thermal Imaging: Fundamentals, Research and Applications.* WILEY-VCH Verlag GmbH & Co., 2010.

[8] [Accessed:19-July-2018]. [Online]. Available: http://www.globalsources.com/si/AS/FLIR-Systems/6008830560341/pdtl/Thermal-Imaging-Camera/1053358970.htm

[9] www.scd.co.il. [Accessed:18-July-2018].

[10] http://www.flir.com/uploadedfiles/eurasia/coresandcomponents/technical notes/uncooled%20detectors%20 BST.pdf. [Accessed:02-Jun-2017].

[11] [Accessed:18-July-2018]. [Online]. Available: https://www.slideshare.net/Yole_Developpement/yole-uncooled-thermalimaging2014sample

[12] [Accessed:19-July-2018]. [Online]. Available: http://www.raptorphotonics.com/wp-content/uploads/2015/10/Ninox-White-Paper-Final.pdf

[13] Y. E. Kesim, E. Battal, M. Y. Tanrikulu, and A. K. Okyay, "An all-ZnO microbolometer for infrared imaging," *Infrared Physics & Technology*, vol. 67, pp. 245–249, nov 2014.

[14] www.raytheon.com/businesses/ ncs/rvs/index.html. [Accessed:18-July-2018].

[15] http://teledynesi.com/imaging/. [Accessed:18-July-2018].

[16] www.sofradir.com/. [Accessed:18-July-2018].

[17] www.selexsas.com/selexgalileo/ en//index.sdo. [Accessed:18-July-2018].

[18] www.aimir.com. [Accessed:18-July-2018].

[19] www.drsinfrared.com. [Accessed:18-July-2018].

[20] A. Rogalski, "History of infrared detectors," *Opto-Electronics Review*, vol. 20, no. 3, jan 2012.

[21] G. D. Skidmore, C. J. Han, and C. Li, "Uncooled microbolometers at DRS and elsewhere through 2013," in *Image Sensing Technologies: Materials, Devices, Systems, and Applications*, N. K. Dhar and A. K. Dutta, Eds. SPIE, may 2014.

[22] E. Mounier, "Uncooled infrared imagers market and technology trends," Yole Development, Tech. Rep., 2017.

[23] E. M. Wormser, "Properties of thermistor infrared detectors," *Journal of the Optical Society of America*, vol. 43, no. 1, p. 15, jan 1953.

[24] R. W. Astheimer, "Thermistor infrared detectors," in *27th Annual Techincal Symposium.*

[25] L. Biberman and R. Sendall, *Introduction: A brief history of imaging devices for night vision*, 2001.

[26] A. Rogalski, "Infrared detectors for the future," *Acta Physica Polonica A*, vol. 116, no. 3, pp. 389–406, sep 2009.

[27] A. Rogalski, P. Martyniuk, and M. Kopytko, "Challenges of small-pixel infrared detectors: a review," *Reports on Progress in Physics*, vol. 79, no. 4, p. 046501, mar 2016.

[28] D. F. Murphy, M. Ray, A. Kennedy, J. Wyles, C. Hewitt, R. Wyles, E. Gordon, T. Sessler, S. Baur, D. V. Lue, S. Anderson, R. Chin, H. Gonzalez, C. L. Pere, and S. Ton, "High sensitivity 640 x 512 20μm pitch microbolometer FPAs," in *Infrared Technology and Applications XXXII*, B. F. Andresen, G. F. Fulop, and P. R. Norton, Eds. SPIE, may 2006.

[29] J. Tissot, P. Robert, A. Durand, S. Durand, E. Durand, and A. Crastes, "Status of uncooled infrared detector technology at ULIS, france," *Defence Science Journal*, vol. 63, no. 6, pp. 545–549, dec 2013.

[30] M. Moreno, R. Jimenez, A. Torres, and R. Ambrosio, "Microbolometers based on amorphous silicon–germanium films with embedded nanocrystals," *IEEE Transactions on Electron Devices*, vol. 62, no. 7, pp. 2120–2127, jul 2015.

[31] P. W. Kruse, *Uncooled Thermal Imaging Arrays, Systems, and Applications.* SPIE press book, July 2001.

[32] C. Chen, X. Yi, X. Zhao, and B. Xiong, "Characterizations of VO_2-based uncooled microbolometer linear array," *Sensors and Actuators A: Physical*, vol. 90, no. 3, pp. 212–214, may 2001.

[33] T. Schimert, J. Brady, T. Fagan, M. Taylor, W. McCardel, R. Gooch, S. Ajmera, C. Hanson, and A. J. Syllaios, "Amorphous silicon based large format uncooled FPA microbolometer technology," in *Infrared Technology and*

Applications XXXIV, B. F. Andresen, G. F. Fulop, and P. R. Norton, Eds. SPIE, apr 2008.

[34] J.-J. Yon, E. Mottin, and J.-L. Tissot, "Latest amorphous silicon microbolometer developments at LETI-LIR," in *Infrared Technology and Applications XXXIV*, B. F. Andresen, G. F. Fulop, and P. R. Norton, Eds. SPIE, apr 2008.

[35] J. Tissot, C. Trouilleau, B. Fieque, A. Crastes, and O. Legras, "Uncooled microbolometer detector: recent developments at ULIS," *Opto-Electronics Review*, vol. 14, no. 1, jan 2006.

[36] F. Forsberg, A. Lapadatu, G. Kittilsland, S. Martinsen, N. Roxhed, A. C. Fischer, G. Stemme, B. Samel, P. Ericsson, N. Hoivik, T. Bakke, M. Bring, T. Kvisteroy, A. Ror, and F. Niklaus, "CMOS-integrated Si/SiGe quantum-well infrared microbolometer focal plane arrays manufactured with very large-scale heterogeneous 3-D integration," *IEEE Journal of Selected Topics in Quantum Electronics*, vol. 21, no. 4, pp. 30–40, jul 2015.

[37] B. Jiang, T. Dong, Y. Su, Y. He, and K. Wang, "Epitaxial growth and characterization of self-doping $Si_{1-x}Ge_x$ multi-quantum well materials," *Journal of Microelectromechanical Systems*, vol. 23, no. 1, pp. 213–219, feb 2014.

[38] H. H. Radamson, M. Kolahdouz, S. Shayestehaminzadeh, A. A. Farniya, and S. Wissmar, "Carbon-doped single-crystalline SiGe/Si thermistor with high temperature coefficient of resistance and low noise level," *Applied Physics Letters*, vol. 97, no. 22, p. 223507, nov 2010.

[39] S. Wissmar, L. Höglund, J. Andersson, C. Vieider, S. Savage, and P. Ericsson, "High signal-to-noise ratio quantum well bolometer materials," in *Optical Materials in Defence Systems Technology III*, J. G. Grote, F. Kajzar, and M. Lindgren, Eds. SPIE, sep 2006.

[40] B. G. Malm, M. Kolahdouz, F. Forsberg, and F. Niklaus, "Characterization and predictive modeling of epitaxial silicon-germanium thermistor layers," in *Proc. of SISPAD*, 2012.

[41] K. Horio and H. Yanai, "Numerical modeling of heterojunctions including the thermionic emission mechanism at the heterojunction interface," *IEEE Transactions on Electron Devices*, vol. 37, no. 4, pp. 1093–1098, apr 1990.

[42] A. Rogalski, "Infrared detectors: status and trends," *Progress in Quantum Electronics*, vol. 27, no. 2-3, pp. 59–210, jan 2003.

[43] T. Kanno, M. Saga, S. Matsumoto, M. Uchida, N. Tsukamoto, A. Tanaka, S. Itoh, A. Nakazato, T. Endoh, S. Tohyama, Y. Yamamoto, S. Murashima, N. Fujimoto, and N. Teranishi, "Uncooled infrared focal plane array having 128 x 128 thermopile detector elements," in *Infrared Technology XX*, B. F. Andresen, Ed. SPIE, oct 1994.

[44] M. C. Foote and E. W. Jones, "High-performance micromachined thermopile linear arrays," in *Infrared Detectors and Focal Plane Arrays V*, E. L. Dereniak and R. E. Sampson, Eds. SPIE, jul 1998.

[45] S. Becker, P. Imperinetti, J.-J. Yon, J.-L. Ouvrier-Buffet, V. Goudon, A. Hamelin, C. Vialle, and A. Arnaud, "Latest pixel size reduction of uncooled IR-FPA at CEA, LETI," in *Electro-Optical and Infrared Systems: Technology and Applications IX*, D. A. Huckridge and R. R. Ebert, Eds. SPIE, oct 2012.

[46] R. Blackwell, D. Lacroix, T. Bach, J. Ishii, S. Hyland, J. Geneczko, S. Chan, B. Sujlana, and M. Joswick, "Uncooled VOx thermal imaging systems at BAE systems," in *Infrared Technology and Applications XXXIV*, B. F. Andresen, G. F. Fulop, and P. R. Norton, Eds. SPIE, apr 2008.

[47] *Seeing photons: progress and limits of visible and infrared sensor arrays.* Committee on Developments in Detector Technologies; National Research Council,, 2010, [Accessed:19-July-2018]. [Online]. Available: http://www.nap.edu/catalog/12896.html

[48] P. W. Kruse and D. D. Skaturd, *Uncooled Infrared Imaging Arrays and Systems.* Academic Press, 1997.

[49] R. S. Saxena, A. Panwar, S. S. Lamba, and R. Bhan, "A sub-circuit model of a microbolometer IR detector and its experimental validation," *Sensors and Actuators A: Physical*, vol. 171, no. 2, pp. 138–145, nov 2011.

[50] M. Liger, "Uncooled carbon microbolometer imager," 2006.

[51] J. M. Lloyd, *Thermal Imaging Systems.* Springer US, 1975.

[52] S. Abbasi, A. Shafique, O. Ceylan, C. B. Kaynak, M. Kaynak, and Y. Gurbuz, "A test platform for the noise characterization of SiGe microbolometer ROICs," *IEEE Sensors Journal*, vol. 18, no. 15, pp. 6217–6223, aug 2018.

[53] M. Moreno, A. Torres, R. Ambrosio, and A. Kosarev, *Un-Cooled Microbolometers with Amorphous Germanium-Silicon a-GexSiy:HThermo-Sensing Films.* nTech, 2012.

[54] J. B. Johnson, "Thermal agitation of electricity in conductors," *Physical Review*, vol. 32, no. 1, pp. 97–109, jul 1928.

[55] H. Nyquist, "Thermal agitation of electric charge in conductors," *Physical Review*, vol. 32, no. 1, pp. 110–113, jul 1928.

[56] F. Hooge, "1/f noise sources," *IEEE Transactions on Electron Devices*, vol. 41, no. 11, pp. 1926–1935, 1994.

[57] F. Hooge and L. Vandamme, "Lattice scattering causes 1/f noise," *Physics Letters A*, vol. 66, no. 4, pp. 315–316, may 1978.

[58] P. Ericsson, L. Höglund, B. Samel, S. Savage, S. Wissmar, O. Öberg, J.-E. Källhammer, and D. Eriksson, "Design and evaluation of a quantum-well-based resistive far-infrared bolometer," in *Electro-Optical and Infrared Systems: Technology and Applications VII*, D. A. Huckridge and R. R. Ebert, Eds. SPIE, oct 2010.

[59] N. Roxhed, F. Niklaus, A. C. Fischer, F. Forsberg, L. Höglund, P. Ericsson, B. Samel, S. Wissmar, A. Elfving, T. I. Simonsen, K. Wang, and N. Hoivik, "Low-cost uncooled microbolometers for thermal imaging," in *Optical Sensing and Detection*, F. Berghmans, A. G. Mignani, and C. A. van Hoof, Eds. SPIE, apr 2010.

[60] F. Herman, "The electronic energy band structure of silicon and germanium," *Proceedings of the IRE*, vol. 43, no. 12, pp. 1703–1732, 1955.

[61] R. Moskalyk, "Review of germanium processing worldwide," *Minerals Engineering*, vol. 17, no. 3, pp. 393–402, mar 2004.

[62] K. Washio, "SiGe HBT and BiCMOS technologies for optical transmission and wireless communication systems," *IEEE Transactions on Electron Devices*, vol. 50, no. 3, pp. 656–668, mar 2003.

[63] J. D. Cressler and G. Niu, *Silicon-Germanium heterojunction bipolar transistors*. Artech House ,Boston ,London, 2003, ch. SiGe Strained-Layer Epitaxy, pp. 35–60.

[64] D. J. Paul, "Si/SiGe heterostructures: from material and physics to devices and circuits," *Semiconductor Science and Technology*, vol. 19, no. 10, pp. R75–R108, sep 2004.

[65] J. Matthews and A. Blakeslee, "Defects in epitaxial multilayers," *Journal of Crystal Growth*, vol. 27, pp. 118–125, dec 1974.

[66] R. People and J. C. Bean, "Calculation of critical layer thickness versus lattice mismatch for Ge_xSi_{1-x}/Si strained-layer heterostructures," *Applied Physics Letters*, vol. 47, no. 3, pp. 322–324, aug 1985.

[67] "Band structure of Si and Ge," [Accessed: 22-May-2018]. [Online]. Available: http://www.ioffe.ru/SVA/NSM/Semicond/SiGe/bandstr.html

[68] C. Maiti, N. Chakrabarti, and S. Ray, *Strained Silicon Heterostructures: Materials and devices (Materials, Circuits and Devices)*. The Institution of Engineering and Technology, 2001, ch. Electronic Properties of Alloy Layers, pp. 99–146.

[69] P. Harrison, *Quantum Wells, Wires and Dots: Theoretical and Computational Physics of Semiconductor,*. John Wiley & Sons, Ltd,England, 2005, ch. Semiconductors and Heterostructures, pp. 8–11.

[70] C. G. V. de Walle and R. M. Martin, "Theoretical calculations of heterojunction discontinuities in the Si/Ge system," *Physical Review B*, vol. 34, no. 8, pp. 5621–5634, oct 1986.

[71] K. Takahashi, M. Fujiu, M. Sakuraba, and J. Murota, "Si epitaxial growth on SiH_3CH_3 reacted Ge(1 0 0) and intermixing between Si and Ge during heat treatment," *Applied Surface Science*, vol. 212-213, pp. 193–196, may 2003.

[72] T. Hirano, M. Sakuraba, B. Tillack, and J. Murota, “Heavy carbon atomic-layer doping at $Si_{1-x}Ge_x$/si heterointerface,” *Thin Solid Films*, vol. 518, no. 6, pp. S222–S225, jan 2010.

[73] H. J. Osten, “Band-gap changes and band offsets for ternary $Si_{1-x-y}Ge_xC_y$ alloys on Si(001),” *Journal of Applied Physics*, vol. 84, no. 5, pp. 2716–2721, sep 1998.

[74] P. Jerier, “Boron autodoping in single-wafer epitaxy of silicon at reduced pressure,” *Journal of The Electrochemical Society*, vol. 146, no. 1, p. 331, 1999.

[75] T. Manku and A. Nathan, “Effective mass for strained p-type $Si_{1-x}Ge_x$,” *Journal of Applied Physics*, vol. 69, no. 12, pp. 8414–8416, jun 1991.

[76] J. Song, C. Yang, H. Zhang, H. Hu, C. Zhou, and B. Wang, “Longitudinal, transverse, density-of-states, and conductivity masses of electrons in (001), (101) and (111) biaxially-strained-Si and strained $Si_{1-x}Ge_x$,” *Science China Physics, Mechanics and Astronomy*, vol. 55, no. 11, pp. 2033–2037, sep 2012.

[77] S. Chun and K. Wang, “Effective mass and mobility of holes in strained Si_{1-x}/Ge_x layers on,” *IEEE Transactions on Electron Devices*, vol. 39, no. 9, pp. 2153–2164, 1992.

[78] S.M.Sze and M.K.Lee, *”Carrier transport phenomena,” in Semiconductor devices, physics and technology.* Wiley, 2013, pp.43-68.

[79] M. M. Rieger and P. Vogl, “Erratum: Electronic-band parameters in strained $Si_{1-x}Ge_x$ alloys on $Si_{1-y}Ge_y$ substrates,” *Physical Review B*, vol. 50, no. 11, pp. 8138–8138, sep 1994.

[80] J.-P. Cheng, V. P. Kesan, D. A. Grutzmacher, T. O. Sedgwick, and J. A. Ott, “Cyclotron resonance studies of two-dimensional holes in strained $Si_{1-x}Ge_x$/Si quantum wells,” *Applied Physics Letters*, vol. 62, no. 13, pp. 1522–1524, mar 1993.

[81] Y. Fu, S. C. Jain, M. Willander, and J. J. Loferski, “Valence band structures of heavily doped strained Ge_xSi_{1-x}layers,” *Journal of Applied Physics*, vol. 74, no. 1, pp. 402–407, jul 1993.

[82] *Sentaurus device User Guide*, 2017, synopsys, Inc. Mountain View, CA.

[83] H. S. Bennett and C. L. Wilson, “Statistical comparisons of data on band-gap narrowing in heavily doped silicon: Electrical and optical measurements,” *Journal of Applied Physics*, vol. 55, no. 10, pp. 3582–3587, may 1984.

[84] S. Jain and D. Roulston, “A simple expression for band gap narrowing (BGN) in heavily doped Si, Ge, GaAs and Ge_xSi_{1-x} strained layers,” *Solid-State Electronics*, vol. 34, no. 5, pp. 453–465, may 1991.

[85] J. Slotboom and H. de Graaff, “Bandgap narrowing in silicon bipolar transistors,” *IEEE Transactions on Electron Devices*, vol. 24, no. 8, pp. 1123–1125, aug 1977.

[86] J. del Alamo, S. Swirhun, and R. Swanson, "Simultaneous measurement of hole lifetime, hole mobility and bandgap narrowing in heavily doped n-type silicon," in *1985 International Electron Devices Meeting.* IRE, 1985.

[87] D. Klaassen, J. Slotboom, and H. de Graaff, "Unified apparent bandgap narrowing in n- and p-type silicon," *Solid-State Electronics*, vol. 35, no. 2, pp. 125–129, feb 1992.

[88] C. Lombardi, S. Manzini, A. Saporito, and M. Vanzi, "A physically based mobility model for numerical simulation of nonplanar devices," *IEEE Transactions on Computer-Aided Design of Integrated Circuits and Systems*, vol. 7, no. 11, pp. 1164–1171, 1988.

[89] S. Reggiani, M. Valdinoci, L. Colalongo, M. Rudan, G. Baccarani, A. Stricker, F. Illien, N. Felber, W. Fichtner, and L. Zullino, "Electron and hole mobility in silicon at large operating temperatures. i. bulk mobility," *IEEE Transactions on Electron Devices*, vol. 49, no. 3, pp. 490–499, mar 2002.

[90] G. Masetti, M. Severi, and S. Solmi, "Modeling of carrier mobility against carrier concentration in arsenic-, phosphorus-, and boron-doped silicon," *IEEE Transactions on Electron Devices*, vol. 30, no. 7, pp. 764–769, jul 1983.

[91] N. Arora, J. Hauser, and D. Roulston, "Electron and hole mobilities in silicon as a function of concentration and temperature," *IEEE Transactions on Electron Devices*, vol. 29, no. 2, pp. 292–295, feb 1982.

[92] S. C. Choo, "Theory of a forward-biased diffused-junction p-l-n rectifier—part III: Further analytical approximations," *IEEE Transactions on Electron Devices*, vol. 20, no. 4, pp. 418–426, apr 1973.

[93] N. Fletcher, "The high current limit for semiconductor junction devices," *Proceedings of the IRE*, vol. 45, no. 6, pp. 862–872, 1957.

[94] D. Klaassen, "A unified mobility model for device simulation—I. model equations and concentration dependence," *Solid-State Electronics*, vol. 35, no. 7, pp. 953–959, jul 1992.

[95] C. Canali, G. Majni, R. Minder, and G. Ottaviani, "Electron and hole drift velocity measurements in silicon and their empirical relation to electric field and temperature," *IEEE Transactions on Electron Devices*, vol. 22, no. 11, pp. 1045–1047, nov 1975.

[96] D. Caughey and R. Thomas, "Carrier mobilities in silicon empirically related to doping and field," *Proceedings of the IEEE*, vol. 55, no. 12, pp. 2192–2193, 1967.

[97] A. Schenk, "A model for the field and temperature dependence of shockley-read-hall lifetimes in silicon," *Solid-State Electronics*, vol. 35, no. 11, pp. 1585–1596, nov 1992.

[98] J. Fossum, R. Mertens, D. Lee, and J. Nijs, "Carrier recombination and lifetime in highly doped silicon," *Solid-State Electronics*, vol. 26, no. 6, pp. 569–576, jun 1983.

[99] L. Huldt, N. G. Nilsson, and K. G. Svantesson, “The temperature dependence of band-to-band auger recombination in silicon,” *Applied Physics Letters*, vol. 35, no. 10, pp. 776–777, nov 1979.

[100] M. G. Ancona and G. J. Iafrate, “Quantum correction to the equation of state of an electron gas in a semiconductor,” *Phys. Rev. B*, vol. 39, pp. 9536–9540, May 1989, doi:10.1103/PhysRevB.39.9536.

[101] D. Schroeder, *Modelling of Interface Carrier Transport for Device Simulation*. Springer Vienna, 1994.

[102] R. E. Bank and D. J. Rose, “Global approximate newton methods,” *Numerische Mathematik*, vol. 37, no. 2, pp. 279–295, jun 1981.

[103] C. B. Kaynak, Y. Yamamoto, A. Goritz, F. Korndorfer, P. Zaumseil, P. Kulse, K. Schulz, M. Wietstruck, A. Shafique, Y. Gurbuz, M. Kaynak, and M. Kaynak, “High performance thermistor based on $Si_{1-x}Ge_x$ /Si multi quantum wells,” *IEEE Electron Device Letters*, pp. 1–1, 2018.

[104] Y. Yamamoto, P. Zaumseil, M. A. Schubert, A. Hesse, J. Murota, and B. Tillack, “Abrupt SiGe and Si profile fabrication by introducing carbon delta layer,” *ECS Journal of Solid State Science and Technology*, vol. 6, no. 8, pp. P531–P534, 2017.

[105] A. Shafique, S. Abbasi, O. Ceylan, Y. Yamamoto, C. B. Kaynak, M. Kaynak, and Y. Gurbuz, “Comprehensive predictive device modeling and analysis of a $Si/Si_{1-x}Ge_x$ multiquantum-well detector,” *IEEE Transactions on Electron Devices*, pp. 1–9, 2018.

[106] A. Shafique, S. Abbasi, O. Ceylan, A. Goeritz, Y. Yamamoto, C. B. Kaynak, M. Kaynak, and Y. Gurbuz, “A behavioral model for high Ge content in $Si/Si_{1-x}Ge_x$ multi-quantum well detector,” *IEEE Sensors Journal*, pp. 1–1, 2018.

[107] F. B. Atar, A. Yesilyurt, M. C. Onbasli, O. Hanoglu, and A. K. Okyay, “Ge/SiGe quantum well p-i-n structures for uncooled infrared bolometers,” *IEEE Electron Device Letters*, vol. 32, no. 11, pp. 1567–1569, nov 2011.